NASA/TM—2010-216328

Predictions of Supersonic Jet Mixing and Shock-Associated Noise Compared With Measured Far-Field Data

Milo D. Dahl
Glenn Research Center, Cleveland, Ohio

May 2010

NASA STI Program . . . in Profile

Since its founding, NASA has been dedicated to the advancement of aeronautics and space science. The NASA Scientific and Technical Information (STI) program plays a key part in helping NASA maintain this important role.

The NASA STI Program operates under the auspices of the Agency Chief Information Officer. It collects, organizes, provides for archiving, and disseminates NASA's STI. The NASA STI program provides access to the NASA Aeronautics and Space Database and its public interface, the NASA Technical Reports Server, thus providing one of the largest collections of aeronautical and space science STI in the world. Results are published in both non-NASA channels and by NASA in the NASA STI Report Series, which includes the following report types:

- TECHNICAL PUBLICATION. Reports of completed research or a major significant phase of research that present the results of NASA programs and include extensive data or theoretical analysis. Includes compilations of significant scientific and technical data and information deemed to be of continuing reference value. NASA counterpart of peer-reviewed formal professional papers but has less stringent limitations on manuscript length and extent of graphic presentations.

- TECHNICAL MEMORANDUM. Scientific and technical findings that are preliminary or of specialized interest, e.g., quick release reports, working papers, and bibliographies that contain minimal annotation. Does not contain extensive analysis.

- CONTRACTOR REPORT. Scientific and technical findings by NASA-sponsored contractors and grantees.

- CONFERENCE PUBLICATION. Collected papers from scientific and technical conferences, symposia, seminars, or other meetings sponsored or cosponsored by NASA.

- SPECIAL PUBLICATION. Scientific, technical, or historical information from NASA programs, projects, and missions, often concerned with subjects having substantial public interest.

- TECHNICAL TRANSLATION. English-language translations of foreign scientific and technical material pertinent to NASA's mission.

Specialized services also include creating custom thesauri, building customized databases, organizing and publishing research results.

For more information about the NASA STI program, see the following:

- Access the NASA STI program home page at *http://www.sti.nasa.gov*

- E-mail your question via the Internet to *help@sti.nasa.gov*

- Fax your question to the NASA STI Help Desk at 443–757–5803

- Telephone the NASA STI Help Desk at 443–757–5802

- Write to:
  NASA Center for AeroSpace Information (CASI)
  7115 Standard Drive
  Hanover, MD 21076–1320

NASA/TM—2010-216328

Predictions of Supersonic Jet Mixing and Shock-Associated Noise Compared With Measured Far-Field Data

Milo D. Dahl
Glenn Research Center, Cleveland, Ohio

National Aeronautics and
Space Administration

Glenn Research Center
Cleveland, Ohio 44135

May 2010

This work was sponsored by the Fundamental Aeronautics Program
at the NASA Glenn Research Center.

Level of Review: This material has been technically reviewed by technical management.

Available from

NASA Center for Aerospace Information
7115 Standard Drive
Hanover, MD 21076–1320

National Technical Information Service
5301 Shawnee Road
Alexandria, VA 22312

Available electronically at http://gltrs.grc.nasa.gov

Predictions of Supersonic Jet Mixing and Shock-Associated Noise Compared with Measured Far-Field Data

Milo D. Dahl
National Aeronautics and Space Administration
Glenn Research Center
Cleveland, Ohio 44135

Abstract

Codes for predicting supersonic jet mixing and broadband shock-associated noise were assessed using a database containing noise measurements of a jet issuing from a convergent nozzle. Two types of codes were used to make predictions. Fast running codes containing empirical models were used to compute both the mixing noise component and the shock-associated noise component of the jet noise spectrum. One Reynolds-averaged, Navier-Stokes-based code was used to compute only the shock-associated noise. To enable the comparisons of the predicted component spectra with data, the measured total jet noise spectra were separated into mixing noise and shock-associated noise components. Comparisons were made for 1/3-octave spectra and some power spectral densities using data from jets operating at 24 conditions covering essentially 6 fully expanded Mach numbers with 4 total temperature ratios.

1 Introduction

Computational codes that attempt to predict jet noise vary from the near instantly computed empirical models to numerically intensive, extremely long running, direct simulations. The empirical models are limited in their ability to predict the radiated jet noise beyond the relatively small set of geometries and operating conditions with which they were developed. At the other extreme, the computationally intensive models may simulate all the proper physics for noise predictions, but running them is so costly that they currently have little practical usage. In between these two are found attempts to increase the practical ability to predict jet noise by using more sophisticated numerical tools and physical models that achieve results in an acceptable amount of time.

In general, a jet noise model must predict the radiated noise from all the sources that exist throughout the range of useful jet operating conditions. At lower speeds, the noise may be characterized as coming from the fine-scale turbulence in the flow. As the speed increases, the noise due to coherent, large-scale turbulence becomes significant starting in the directions off the downstream jet axis. Near sonic conditions and above cause pressure imbalances in the flow, creating shocks. The interaction between turbulence and shocks creates an additional source of noise that radiates over a broad range of higher frequencies and predominantly in the direction upstream of the nozzle exit. If coherent feedback occurs, then intense screeching can also be present. These are all potential sources of radiated jet noise. An approach to making jet noise predictions is to model the sources separately. Then assuming incoherent sources, the radiated noise from each source is combined in the far field to obtain the total noise. Alternatively, some or all of the jet noise sources are computed simultaneously to obtain the total radiated noise. Once a modeling tool has been developed, it must be validated by comparing predictions to experimentally measured data.

As part of a larger study to assess NASA's capability to predict aircraft noise,[1] empirical and acoustic analogy based tools were used to predict jet noise and the results were compared to measured data over a wide range of operating conditions.[2] The jet experiments used nozzle geometries including convergent, convergent-divergent, internal mixer, separate flow, and chevron configurations operating with Mach numbers from 0.3 to 2.0 and temperatures from 0.8 to 3.0 times the ambient temperatures. The predicted jet noise included both mixing noise, for all jet operating conditions, and broadband shock-associated noise, for supersonic jet operating conditions. The general conclusions were that the empirical tools could make successful overall sound pressure level predictions for a broad range of nozzle geometries and operating conditions while the acoustic analogy tools were successful for a very limited range of operating conditions using a single stream

nozzle. No attempt was made in the above study to separately assess the ability to predict the broadband shock-associated noise generated during supersonic jet conditions. This report includes separate assessments of mixing noise and broadband shock-associated noise prediction codes. Jet noise predictions from older and more recent models are compared to a set of acoustic measurements from supersonic, shock-containing jets at a variety of jet speeds and temperatures. Predictions are made for both mixing noise sources and shock-associated noise sources.

Following a brief description of the experiments and a presentation of the spectral data obtained from the experiments, a summary of the various jet noise prediction models assessed herein is given. The jet mixing noise prediction models are empirical in nature and depend on their underlying experimental database. The broadband shock-associated noise models have varying degrees of empiricism, but only a Reynolds-averaged, Navier-Stokes (RANS) based model uses flow field calculations as a part of the jet noise prediction scheme. This allows nozzle geometry and flow field conditions outside of the experimental database to be used in making jet noise predictions. The RANS-based broadband shock-associated noise model is new and only an initial assessment for single-stream, round jets is provided here to compare with previous model predictions.

2 Experimental Setup

The experimental jet noise spectral data used in this study were acquired during an extensive test program conducted using the Small Hot Jet Acoustic Rig (SHJAR) at the NASA Glenn Research Center. The SHJAR is a single-stream, hot jet rig installed within the AeroAcoustic Propulsion Laboratory, a 65-foot geodesic dome lined with acoustic absorbing material to provide anechoic conditions for noise testing at all frequencies above 200 Hz. More information on this facility may be found in Bridges & Brown[3] and other reports describe the types of data and the quality of the data collected during testing in this facility.[4–6]

Khavaran & Bridges[7] discuss details of the test results from the program to measure the noise from jets at a variety of nozzle pressure ratios and total temperatures. Tables are given that describe the different nozzles used and the variety of operating conditions tested. A subset of that data is used here consisting of noise data from supersonic jets issuing from a 2.0-inch exit diameter, circular, convergent nozzle. The nozzle, designated as smc021, is a modified version of the smc000 baseline convergent nozzle with a 5-degree conic contraction and a 0.04-inch thick lip, see Figure 1. The smc021 nozzle had a sharp edge lip with notches cut into the edge. These nozzles are shown in Figure 2. The purpose of the modifications was to minimize the screech noise observed in the smc000 nozzle spectral data.

To assess the various shock-containing jet noise prediction models, the data were collected using the smc021 nozzle operated at the 24 conditions listed in Table 1. The operating conditions are grouped according to constant total temperatures. However, the operating condition parameters were recorded at the time the acoustic data were measured, hence, the numbers in the table reflect the slight variations in conditions that occurred during the testing. The table column headings are given as follows:

Rdg – designates the experimental reading number used to label the various operating conditions.

T_t/T_∞ – the nozzle flow total temperature to ambient temperature ratio.

NPR – the nozzle pressure ratio defined as the nozzle flow total pressure divided by the ambient pressure.

M_j – the fully expanded jet Mach number computed using the equation

$$M_j = \left[\left(\frac{2}{\gamma_j - 1} \right) \left(\mathrm{NPR}^{\frac{\gamma_j - 1}{\gamma_j}} - 1 \right) \right]^{\frac{1}{2}} \tag{1}$$

V_j/c_∞ – the acoustic Mach number is the ratio of the fully expanded jet velocity to the ambient speed of sound. The fully expanded jet velocity is computed from M_j using the fully expanded speed of sound

$$c_j = \sqrt{\gamma_j \, R T_j} \tag{2}$$

and the fully expanded temperature

$$T_j = \frac{T_t}{1 + \dfrac{\gamma_j - 1}{2} M_j^2} \tag{3}$$

β – the shock noise parameter

$$\beta = \sqrt{M_j^2 - 1} \tag{4}$$

γ_j – the ratio of specific heats at the fully expanded jet conditions. It is based on assuming that the jet flow is a calorically imperfect, thermally perfect gas. It is computed by iteration using equations (180), (43), and (44) in the 'Ames Tables'[8] where NPR and T_t are fixed and known and the resulting Mach number is M_j.

T_∞ – the ambient temperature in degrees Kelvin.

p_∞ – the ambient pressure in Pascals.

c_∞ – the ambient speed of sound in meters per second computed from the equation

$$c_\infty = \sqrt{\gamma\, R\, T_\infty} \tag{5}$$

where $\gamma = 1.4$ and $R = 286.959\,\mathrm{m}^2/(\mathrm{s}^2\mathrm{K})$.

3 Description of Measured Data and Analysis

The measurements of the noise radiated from the jet were made by 24 microphones. These microphones were located on an arc 50 nozzle exit diameters from the center of the nozzle exit area and placed at 24 equally-spaced angles. The angles were from 50 to 165 degrees as measured from the upstream inlet centerline to the nozzle.

As described in Bridges et al.[2] and in Khavaran & Bridges,[7] the time histories for the microphone signals were processed using the Finite Fourier Transform with suitable averaging and scaling to obtain narrow band spectral data with amplitude levels adjusted to report results at a radius of 100 nozzle exit diameters. The atmospheric attenuation inherent in the measured data was removed resulting in lossless spectra. These spectra contained 8193 points at equally spaced intervals of about 12 Hz. The spectral amplitudes were normalized by the frequency interval to obtain a power spectral density. Follow-on processing generated 1/12-octave and 1/3-octave spectra as desired.

Jet noise prediction models are available for computing only the mixing noise component, only the broadband shock-associated noise component, or combining the two components to compute the total radiated jet noise (not including any jet screeching noise in the predictions). Given that only the total radiated jet noise was measured, Khavaran & Bridges[7,9] developed scaling laws that attempt to separate the total jet noise into its mixing noise and shock-associated noise components. The results of this spectral component separation for the Table 1 conditions are shown in Figure 3 for measurements at a 50 degree inlet angle. The plots show 1/3-octave lossless spectra as a function of the Strouhal number fD/V_j, where, in this case, f is the 1/3-octave center frequency, D is the nozzle exit diameter, and V_j is the fully expanded jet velocity.

Khavaran & Bridges[7,9] discuss that the smc021 nozzle was designed to reduce screech, but did not eliminate it. Even at reduced amplitude, the screech was noted to have induced the effect of mixing noise amplification. This additional noise could be included as part of the velocity-scaled mixing noise or included as part of the shock-associated noise. The plots show both types of component separation. The total noise is either the sum of shock-associated noise and mixing noise with amplification or the sum of shock-associated noise with amplification and mixing noise. However, the discussion on jet noise amplification given in Deneuville & Jacques[10] describes the issue as more complicated than this simple noise component separation suggests. Both the broadband noise due to mixing and due to shock association are affected by the presence of screech tones as excitation sources. The mixing noise is amplified as a result of excitation's effect on the turbulence and as this turbulence passes through the shock structure, the broadband shock-associated noise is possibly amplified. Currently, there is no certain way to determine the amount of amplification that is applied to each component. The results shown in Figure 3 suggest that when the shock-associated noise is distinctly dominant over the mixing noise at the forward angles, the amount of screech present in the current set of noise data has little affect on the shock-associated noise amplitude. Hence for a first approximation in these results, the effects of jet noise amplification will be applied only to the mixing noise component for the purposes of comparing jet mixing noise predictions with measured data in this report and no further consideration will be given to adding amplification to the shock-associated noise data.

Figures 4 and 5 show the component separation results for measurements at 90 degrees and 120 degrees, respectively. Mixing noise can be seen to dominate at the lower frequencies and becoming a larger portion of the spectrum as the directivity angle moves downstream. Conversely, the broadband shock-associated noise dominates at the higher frequencies and at the upstream angles. After brief descriptions of both mixing noise and shock-associated noise models, these spectral data from measurements will be compared to predicted spectra.

4 Description of Jet Noise Prediction Models

The assessment conducted by Bridges et al.[2] used predictions computed using one empirical model and two acoustic analogy models. Far fewer predictions were made with the latter due to the larger amount of computational resources required, especially that these models require a flow solution computed using a Reynolds-averaged, Navier-Stokes (RANS) solver. The approach here is also to use models containing various amounts of empiricism for predicting both the mixing noise component and the shock-associated noise component of the noise spectrum from supersonic jets with shocks. Then for a subset of data, predictions are compared to measured data for a recent RANS-based shock-associated noise prediction model.

4.1 Mixing Noise Models

As a jet flow issues from a nozzle, the flow mixes with and expands into the surrounding medium. From the initial shear layer to the downstream developed jet, turbulent eddies develop at various times and of various sizes, cascading their energy through the flow, emitting unsteady fluctuations that become sound outside of the jet. Mixing noise models attempt to predict this radiated noise and the empirical models attempt to predict it over the whole frequency range and at every directivity angle from the jet axis. The two models used here are both part of NASA's Aircraft Noise Prediction Program (ANOPP).[11] The ANOPP code assembles noise source prediction modules for engine and airframe components and links them to an acoustic propagation code to obtain far field noise levels and sound spectra. While complete aircraft system level noise predictions may be computed using ANOPP, the individual modules within ANOPP may be used to make component level noise predictions. For the jet mixing noise predictions, the modules named SGLJET and ST2JET are used.

4.1.1 ANOPP Module SGLJET

The SGLJET module predicts the radiated jet mixing noise for single stream, shock-free, jet flows issuing from circular, convergent nozzles. It uses the methodology found in the SAE ARP 876 document which depends on tabulated data obtained from experiments.[12]

The equation for the far-field, mean-square acoustic pressure contains constants obtained from fitting experimental data and functions that either represent correlated equations or interpolations of tabulated values. The general form for the equation is given as

$$\langle p^2 \rangle \propto \frac{1}{r^2}\,\Pi(\rho_j^{\omega}, V_j)\,\mathrm{D}(\theta, V_j)\,\mathrm{F}(S_c, \theta, V_j, T_j)\,\mathrm{f}(V_j, \theta, M_{\infty}) \tag{6}$$

The overall acoustic power is given by the Π-function. It is a variation of the classic V^8 power law and attempts to account for the changes in jet density and the deviations from the power law as the jet velocity changes. Both of these are incorporated through tabulated values of a density exponent ω and a power deviation factor, both as functions of V_j. The directivity function D is tabulated versus both the directivity angle θ, measured from the inlet, and the jet velocity V_j. F is the normalized spectral distribution factor that determines the 1/3-octave spectra for each frequency as a function of the jet velocity, directivity angle, and temperature. The frequencies of the normalized spectra are given in terms of a corrected Strouhal number S_c that depends on an empirical function of the jet velocity. Finally, the results may be modified for the effects of forward velocity through the f-function.

4.1.2 ANOPP Module ST2JET (Mixing)

The ST2JET module predicts jet noise for one or two stream circular nozzles. The nozzles can be either convergent or convergent-divergent and can be operated at subsonic or supersonic conditions. As such, it includes both mixing noise and shock-associated noise sources.

For single stream jets, the radiated mixing noise is modeled to come from three sources: 1) The small scale mixing noise that comes from near the nozzle exit. This noise has relatively high frequency content. 2) The intermediate scale mixing noise that comes from the shear layer as the jet mixes with the ambient air. This noise contains mid- to high-frequency content. 3) The large scale mixing noise that comes from the fully developed jet. It contains the lower frequency noise. Though each of these mixing noise source models have different frequency content and different spectral amplitudes, they all may be represented by an equation for the far field mean-square acoustic pressure of the form

$$\langle p^2 \rangle \propto \frac{1}{r^2}\,\Pi(\rho_j, V_j, M_\infty)\,\mathrm{D}(\theta', V_j)\,\mathrm{F}(S', \theta') \tag{7}$$

For each source, the acoustic power function Π is computed using a correlation equation and both the directivity function D and the spectrum function F are determined from an interpolation of tabulated values. To be clear, each of the three mixing noise sources has its own set of correlations and tabulated values. The directivity and spectral functions depend on an effective directivity angle θ' and an effective Strouhal number S'. The effective directivity angle has an empirical modification to account for the effects of the jet flow and the freestream flow on the directivity angle of the noise radiated from the jet. S' depends on the effective directivity angle and includes additional effects due to jet temperature.

4.2 Shock-Associated Noise Models

Supersonic jet flows from convergent nozzles are imperfectly expanded creating shocks in the flow. The turbulence normally created by jet flows interacts with the shock structure producing a noise source in addition to that produced by turbulent mixing. This source may emit tones, known as screech, and a wide band of noise called broadband shock-associated noise. This latter noise is of main interest here. Though considered a broadband noise, shock-associated noise has a characteristic spectrum with a fundamental peak and has spectral levels that vary with the directivity angle. It is also most dominant at angles upstream of the nozzle exit. A prediction model for shock-associated noise was first proposed by Harper-Bourne & Fisher.[13] Deneuville[14] used ideas from Harper-Bourne & Fisher (HBF) and experimental data to develop a simplified version of the model. Both models are discussed further and compared to measured data in Balsa et al.[15] Later Tam[16,17] used the physics of large-scale turbulent structures in shock-containing jets to develop a model for shock-associated noise. Both the HBF and Tam models have been incorporated into ANOPP as the SAESHK and the TAMSHK modules. In addition to these modules, the ST2JET module also predicts shock-associated noise. The simplified model from Deneuville was programmed based on the work of Gliebe et al.[18] Finally, a model was recently developed by Morris & Miller[19] to use a RANS-based flow solution as part of a shock-associated noise model.

4.2.1 ANOPP Module SAESHK

The SAESHK module in ANOPP contains the HBF shock-associated noise model as given in the formulas of the SAE ARP 876 document.[12] These formulas closely follow those given in Harper-Bourne & Fisher[13] after the equation for the far field pressure spectrum is integrated to obtain the sound pressure spectrum in 1/3-octave bands as described by Balsa et al.[15]

The form of the equation for the far field mean-square acoustic pressure is given by

$$\langle p^2 \rangle \propto \frac{1}{r^2}\,\left[1 + \mathrm{W}(\sigma, \theta, V_j)\right]\,\beta^\eta\,\mathrm{H}(\sigma) \tag{8}$$

where β is the shock noise parameter defined in equation (4), η is an exponent that is equal to 4 if $\beta \leq 1$ or if $\beta > 1$, it equals 1 for unheated jets or 2 for heated jets, σ is a frequency parameter based on shock cell spacing and Mach number, H is the group source strength spectrum tabulated from measured data, and W is a shock cell noise source interference function. The interference function uses a tabulated correlation

coefficient spectrum and accounts for the constructive and destructive interference between the shock cell noise sources.

4.2.2 Simplified Shock-Associated Noise Model

The 'Simplified' model is an empirical correlation for the spectrum of shock-associated noise based on two straight lines that join at the peak of the spectrum.[14] The peak frequency is computed from

$$f_p = \frac{0.7\,V_j}{1.1\beta D(1 + M_c \cos\theta)}, \tag{9}$$

where for no ambient flow $M_c = 0.7\,V_j/c_\infty$, and the peak sound level is of the form

$$\langle p^2 \rangle_{max} \propto \frac{1}{r^2}\,\beta^4. \tag{10}$$

The far field sound spectrum is then given by

$$\langle p^2 \rangle = \langle p^2 \rangle_{max} \left(\frac{f}{f_p}\right)^n \tag{11}$$

where $n = 7$ for $f/f_p \leq 1$ and $n = -1$ for $f/f_p > 1$. The program for this model is taken from the 'MGB' code found in Gliebe et al.[18]

4.2.3 ANOPP Module TAMSHK

The broadband shock-associated noise model of Tam[16,17] is based on the theory that large-scale turbulent structures generated in the supersonic jet mixing layer interact with the periodic-like shock cell structure that exists in imperfectly expanded jets. This interaction causes pressure perturbations that radiate as sound. The large structures are modeled as a sum of instability waves each with their own amplitude envelope and phase speed characteristics. These characteristics affect the amplitude and directivity of the radiated noise. The model is applicable to both the under-expanded and the over-expanded jets that can issue from convergent-divergent nozzles. In this report, it is applied only to convergent nozzle jet flows.

The form for the far field mean-square acoustic pressure is

$$\langle p^2 \rangle \propto \frac{1}{r^2}\,\Pi(A_j, M_j, T_j)\,\mathrm{F}(\theta, f) \tag{12}$$

where Π is the overall shock noise acoustic power function and F is the spectral distribution function. Using the nozzle exit area and the jet Mach number and temperature, the overall acoustic power is computed from correlated equations based on the theoretical development of equations describing the physical jet flow. These include equations for the spatial extent of the noise source, the jet core length, the shock cell strength, and the fully expanded jet area. The spectral distribution function is computed from a sum of modes that result from the instability wave theory. Correlated equations for the wave number and convection velocity are used to enable rapid calculation of the modal summation at each frequency. The summed results are integrated across bands of frequency to obtain the desired 1/3-octave spectrum.

4.2.4 ANOPP Module ST2JET (Shock)

The shock-associated noise predicted by the ST2JET module is based on an equation that has the same form as equation (7) but written as

$$\langle p^2 \rangle \propto \frac{1}{r^2}\,\Pi(\beta, \theta_c, M_j, M_\infty)\,\mathrm{D}(\theta_c)\,\mathrm{F}(S', \theta_c) \tag{13}$$

The acoustic power function depends on a correlation using the shock parameter β and a corrected directivity angle. The latter also determines the interpolated value for the directivity function D. The spectrum function F also requires the effective Strouhal number to obtain its interpolated value.

4.2.5 RANS-Based Model

Morris & Miller[19] developed a broadband shock-associated noise prediction model that uses a RANS-based flow solution as input. This enables the prediction of shock-associated noise from one or two stream jets from nozzles with realistic geometries. Using the inviscid compressible equations of motion, the flow field variables are separated into four components: the mean value, the perturbations associated with the shock cell structure, the turbulent fluctuations, and the disturbances generated by the interaction between the turbulence and the shock cell structure. Linearized inhomogeneous equations for the interaction disturbances are derived where the sources are products of the shock cell perturbations and the turbulent fluctuations. An integral solution is derived using the Green's function approach. After considerable manipulation, the solution for the far field spectral density is found to have the form

$$S(\mathbf{x},\omega) \sim \frac{\omega^2}{c_\infty^4 |\boldsymbol{x}|^2} \int_{-\infty}^{\infty} \frac{1}{l^2} p_s(\mathbf{y}) p_s(\mathbf{y}+\boldsymbol{\eta}) R^v(\mathbf{y},\boldsymbol{\eta},\tau) \exp\left[i\omega \left(\tau - \frac{\boldsymbol{x}\cdot\boldsymbol{\eta}}{|\boldsymbol{x}| c_\infty} \right) \right] \mathrm{d}\tau \, \mathrm{d}\boldsymbol{\eta} \, \mathrm{d}\mathbf{y} \tag{14}$$

where l is a characteristic turbulent length scale, p_s is the shock cell pressure perturbation, R^v is a two-point, cross-correlation function of turbulent velocity fluctuations, and the exponential term represents the far field Green's function. The $R^v(\mathbf{y},\boldsymbol{\eta},\tau)$ term must be modeled in order to obtain a solution. The model contains turbulent length and time scales that are computed using the RANS turbulent kinetic energy and viscous dissipation rate data with an additional constant coefficient. The chosen form of the model for R^v has three constant coefficients. In addition, equation (14) requires a constant to set the proper amplitude of the spectrum. Once these four constant coefficients are set by fitting predictions to experimental data, all the other required parameters in the final form of the integral are found from the RANS solution.

5 Results for Jet Noise Component Predictions

The 1/3-octave spectral data shown in Figures 3 to 5 will now be compared to predicted results using the empirical jet noise prediction models. The comparisons are shown as lossless 1/3-octave spectra in terms of sound pressure level (dB reference 2×10^{-5} Pa) versus the Strouhal number for the operating conditions shown in Table 1. The first set of figures compares predictions for the mixing noise component spectra to velocity-scaled mixing noise spectra determined from data with and without the amplification effects. The second set of figures makes comparisons between predictions and measured data for the shock-associated noise component spectra. Finally in this section, the third set of figures compares predictions to both the total measured jet noise spectra and the shock-associated noise component spectra. For each set of figures, the predicted spectra are compared to the measured spectral data taken at the directivity angles of 50, 90, and 120 degrees to the jet inlet.

5.1 Mixing Noise Component Spectra

Figures 6 to 8 compare predictions for the mixing noise from the ANOPP modules SGLJET and ST2JET to the mixing component of the jet noise spectrum. Starting at the cold jet conditions and the 50 degree inlet angle, Figures 6(a)–(f) show qualitatively good comparisons between the two predictions and the mixing noise with amplification at the low frequencies less than the peak frequency for the shock-associated noise. As the amplification effect becomes more important as the jet speed increases, the predicted spectra tend to be closer to the amplified mixing noise at low frequencies and close to the normally scaled mixing noise at the high frequencies. For all these cold jet conditions, the SGLJET predictions, in general, produce spectrum levels that are slightly higher than those produced by the mixing noise part of the ST2JET predictions.

As the jet total temperature ratio increases with $T_t/T_\infty \approx 1.76$ in Figures 6(g)–(l), $T_t/T_\infty \approx 2.16$ in Figures 6(m)–(r), and $T_t/T_\infty \approx 2.65$ in Figures 6(s)–(x), the levels of mixing noise increase. This follows from the scaling of mixing noise with jet velocity which, as shown in Table 1, has increased as the jet temperature increased in order to approximately maintain a constant fully expanded jet Mach number. There are few general trends in these comparisons to which there are not exceptions. One general trend is that the mixing noise predictions are all closer to the mixing noise with amplification spectra. Another is that the SGLJET predicted levels continue to be generally higher than those from the ST2JET predictions.

When predicted spectra are compared to the mixing noise with amplification spectra, there is qualitative agreement at the low frequencies and a general trend to predict lower spectral levels than the component levels at higher frequencies especially at higher jet velocities. The predictions are always higher than the velocity-scaled mixing noise without the amplification effects included.

At 90 degrees, Figures 7(a)–(f) show comparisons for the cold jet. The predictions are qualitatively as good as they were at 50 degrees except here the ST2JET predictions are generally slightly higher than the SGLJET predictions. The mixing component and the mixing with amplification component are close for these cold jet conditions. However, as the jet total temperature ratio increases, the mixing noise component spectra with amplification have generally a greater level than just the velocity-scaled mixing noise. This separation in level becomes larger as the jet Mach number increases. As with the 50 degree comparisons, the predicted spectra in Figures 7(g)–(x) follow the mixing component with amplification spectra as the total temperature ratio changes. In general, both prediction modules produce spectral levels that are a little higher than the mixing component spectra with amplification, with the ST2JET spectra levels being higher at all the operating conditions.

Figure 8 shows the mixing noise component spectra comparisons at a 120 degree inlet angle. At this angle, the measured data component separation is showing very little in the way of amplification effects on the mixing noise. Both predicted spectra are higher than the measured data at just about all frequencies and operating conditions. The ST2JET spectra are higher than the SGLJET spectra except at the higher frequencies where the ST2JET spectra drops to a lower level than the SGLJET spectra.

Given that these two jet mixing noise prediction models depend on measured data and that the supersonic conditions used here are within the original data range used when these models were developed, it is possible that the original jet spectral data were measured from supersonic jets that had a sufficient amount of screech that resulted in amplified mixing noise. The comparisons in Figures 6 to 8 show that the mixing noise predicted spectra are closer to the mixing noise component spectra with amplification. Even then, the predictions are typically higher in amplitude than measured amplitudes by as much as 9 dB at low to mid frequencies at 120 degrees. To summarize this, it is noted that the low frequency measured and predicted mixing noise spectra are similar in shape and often nearly constant in separation, hence the difference between the predicted level and the measured component level with amplification at a Strouhal number of 0.1 is used to indicate the quality of the prediction or the prediction error. Figure 9 shows contour plots using those errors as a function of the jet operating conditions. Within the limitations of interpolating within the set of data points used in the plots, the plots show that more often than not both models predict higher amplitude levels of mixing noise than was measured, especially for higher speed and/or higher temperature jets. Both models have similar behavior for the mixing noise level error. At 50 degrees, the predicted noise levels are too high for lower speed, higher temperature jets. Basically all the higher temperature jets have predicted levels too high at 90 degrees. Finally at 120 degrees, all levels are predicted too high with the highest levels occurring for the higher speed, higher temperature jets. Based on the levels of the extreme values indicated by the scale on each plot, the mixing noise predictions from the SGLJET module tend to give more accurate predictions than the mixing noise predictions from the ST2JET module for shock containing jets. The variations in the SGLJET module predictions are 5.7 dB at 50 degrees, 4.4 dB at 90 degrees, and 3.6 dB at 120 degrees. The ST2JET module predictions have variations of 6.5 dB at 50 degrees, 4.7 dB at 90 degrees, and 7.1 dB at 120 degrees. These results are based on the data at the actual measurement points and not on any interpolated results.

5.2 Shock-Associated Noise Component Spectra

The broadband shock-associated noise component spectrum for an under-expanded supersonic jet was obtained by subtracting the velocity-scaled mixing noise component spectrum from the total jet noise spectrum.[7,9] As shown in Figures 3 to 5, and discussed previously, the noise amplification phenomenon resulting from the presence of any screech tones increases the noise levels of the component spectra. In this report, all of the noise due to amplification is assigned to the mixing noise component. Figures 10 to 12 show the comparison of the predicted broadband shock-associated noise spectra to the resulting shock-associated noise component spectra without any amplification.

Figure 10 shows the shock-associated noise component comparisons between measured data and model predictions at a 50 degree inlet angle. Harper-Bourne & Fisher[13] and Tanna[20] discuss the variations of

total shock-associated noise intensity with β found in their experimental data. The predictions from the three empirical models follow these experimental results in terms of the behavior of their computed 1/3-octave spectra. Each group of jet temperature operating conditions shown in Table 1 have six similar values for β. At the lowest β, Figures 10(a), (g), (m), and (s) all show that the ST2JET shock-associated noise component predictions peak at a frequency lower than the other predictions and has a peak level higher than the other predictions. This is followed by the 'Simplified' spectra which have a lower level and a higher peak frequency. The peak for the TAMSHK predictions have yet a lower level, but about the same or slightly higher peak frequency than the 'Simplified' model. The four plots have similar high frequency behavior for the predictions. As β increases, the peak levels and frequencies become to have greater agreement with each other and with the measured data as in Figures 10(d), (j), (p), and (v). The high frequency slope behavior of the spectra are similar across these four plots, also, though the TAMSHK high frequency levels are lower. At the two highest β's, we see that levels predicted by the 'Simplified' model are getting higher compared to the other predictions and the measured data and the TAMSHK spectra has larger peaks and valleys than previous. Though the higher frequency behaviors are quite varied between predictions, they are consistent across the plots with constant β and the peak frequency is predicted quite well by all models.

Similar comments can be made about the 90 degree spectral comparisons in Figure 11 as was made for the 50 degree comparisons. An obvious exception is that the ST2JET predictions are consistently lower in level than the other predictions at the higher β's.

At the 120 degree angle, Figure 12 shows more variability across the predicted shock-associated noise spectra with constant β. The peak frequency predicted by ST2JET is lowest at low β. As β increases, the peak frequency from ST2JET comes to agree with the TAMSHK prediction for cold jets. As the jet temperature increases, the ST2JET prediction for peak frequency is higher than the TAMSHK prediction at higher β's. For all higher speed, heated jet cases, the 'Simplified' model predicts a higher peak frequency than the other two models. The spectral levels for the ST2JET predictions are always lowest and lower than the shock-associated noise component spectra. The TAMSHK predictions for spectral levels agree with the data from cold jets, but under predicts for heated jets. The high frequency spectral predictions from the 'Simplified' model tend to agree with the total noise spectra even though the peak frequencies are predicted to be higher than that shown in the data for heated jets.

The quality of the shock-associated noise predictions is determined by computing the error in predicting both the peak level and the peak frequency. For each of the three model predictions shown in Figures 10 to 12, the peak level error is computed by subtracting the measured 1/3-octave peak level from the predicted 1/3-octave peak level. The error in peak frequency is determined relatively by dividing the predicted peak frequency by the measured peak frequency. Figures 13 to 15 show contour plots of peak level error and peak frequency error as a function of the jet operating conditions and angle for each of the three shock-associated noise prediction models. The levels shown on the legends indicate the range of values on the plot. The largest errors on the peak level error plots are found at either the $M_j \approx 1.05$ or the $M_j \approx 1.8$ conditions. Using the results for all jet temperatures between about $M_j = 1.2$ and $M_j = 1.7$, the following variations in peak level error are found for the three broadband shock-associated noise prediction models:

Simplified Model
- 50 degrees, +3.8 dB, −2.5 dB for a 6.2 dB variation.
- 90 degrees, +2.3 dB, −3.8 dB for a 6.1 dB variation.
- 120 degrees, +1.7 dB, −3.9 dB for a 5.6 dB variation.

TAMSHK Module
- 50 degrees, +4.0 dB, −0.0 dB for a 4.0 dB variation.
- 90 degrees, +2.1 dB, −2.2 dB for a 4.3 dB variation.
- 120 degrees, +1.3 dB, −6.2 dB for a 7.5 dB variation.

ST2JET Module
- 50 degrees, +0.0 dB, −3.8 dB for a 3.8 dB variation.
- 90 degrees, −0.2 dB, −7.0 dB for a 6.8 dB variation.
- 120 degrees, +0.0 dB, −8.7 dB for a 8.7 dB variation.

On the basis of the these values shown for the peak level error in the $1.2 \lesssim M_j \lesssim 1.7$ operating range, the TAMSHK module provides more accurate predictions over the range of directivity angles shown. The peak frequency error plots all contain large areas of constant error due to the 1/3-octave band accuracy of the

spectra. The peak frequency is only known within a 1/3-octave band which limits the accuracy of the peak frequency error and provides only an approximate or qualitative indication of the ability to predict the peak frequency.

5.3 Total Jet Noise Spectra

Jet noise spectral predictions computed by the ST2JET module and the SAESHK module are shown in Figures 16 to 18. These results are compared to the total measured noise spectra and to the measured shock-associated noise component spectra. While the ST2JET module was used to compute the total noise spectrum for these comparisons, it should be recalled that the SAESHK module was designed to predict broadband shock-associated noise using the HBF model. However, the SAESHK model predictions were found to compare favorably with measured total noise spectra, especially at upstream angles, for many operating conditions. Hence those results are included in these figures to more clearly highlight the comparisons with measured data rather than adding another model result for shock-associated noise in Figures 10 to 12.

The ST2JET predictions contain both the mixing and shock-associated noise components of the model. Given the issues discussed with the separate component comparisons, the ST2JET predicted total noise spectra compare as follows to the measured spectra at 50 degrees, Figure 16, and 90 degrees, Figure 17: (1) ST2JET predicts the low frequency mixing noise well, (2) ST2JET predicts the shock-associated noise peak frequency where shock-associated noise dominates except at lower β's, (3) ST2JET predicts the shock-associated noise peak level more accurately at 50 degrees than at 90 degrees, (4) ST2JET predicts high frequency levels consistently lower than the measured data. At the 120 degree inlet angle, the ST2JET predictions in Figure 18 are dominated by the mixing noise component model and typically has levels much higher than the measured spectra at low to mid frequencies. At higher frequencies, the presence of shock-associated noise is only clearly seen in the predicted spectra for the cold, lower speed jets, Figure 18(a)–(d).

The predicted spectra from the SAESHK module are also shown in Figures 16 to 18. As mentioned above, this module contains the HBF model which was designed to predict broadband shock-associated noise. As can be seen in the comparisons at 50 degrees in Figure 16, the SAESHK module predicts the shock-associated noise quite well for low-speed, low β jets, especially at $\beta \approx 0.6$. At higher speeds, the predicted spectra compare favorably with the entire total noise spectra especially at lower frequencies where mixing noise is dominant, but not quite as well at frequencies higher than the peak frequency where shock-associated noise dominates. At 90 degrees in Figure 17, the higher frequency predictions for the shock-associated noise are lower creating a larger difference between predicted and measured spectra. In addition, a low frequency hump develops in the predicted spectra as β increases above 0.6 that does not exist in the shock noise component spectra and does not represent the total noise spectral shape, either. This low frequency hump further develops at 120 degrees, as shown in Figure 18, and comes to dominate the spectra over that of the shock-associated noise related peak as β and the jet temperature increase. There is little agreement between the SAESHK module predictions and the measured data at these conditions.

6 Results for Shock-Associated Noise Component Predictions

The comparisons of the RANS-based model predictions with measured spectral data are shown in Figures 19 and 20. The RANS-based model predictions are taken from Morris & Miller[19] for a converging nozzle with $M_j = 1.5$ and either cold, $T_t/T_\infty = 1.00$, or hot, $T_t/T_\infty = 2.20$, conditions. The measurement conditions are not identical to those used for the prediction calculations. Table 1 shows the measured conditions that are closest to those used in the predictions to be Rdg# 2082 for the cold jet and Rdg# 2096 for the hot jet. Using the prediction value for β of 1.118 and the measurement value of β of 1.109, an estimate of the peak level difference between these two conditions is found using equation (10). Substituting for the β values and taking the difference in decibels, with all other parameters assumed equal, results in a ± 0.14 dB variation between the two operating conditions. A similar test for the peak frequency in terms of the Strouhal number uses equation (9) to ratio the two peak Strouhal numbers resulting in at most a $\pm 1.8\%$ variation in the peak Strouhal number between the two operating conditions at inlet angles less than 120 degrees. Hence, the measured spectra for these readings are used for comparison to the predictions performed by Morris & Miller plotted in Figures 19 and 20. Both figures show power spectral density and 1/3-octave spectra for each inlet directivity angle from 50 degrees to 120 degrees in 10 degree increments.

The results for the cold jet are shown in Figure 19. For the power spectral density plots, the RANS-based model and the Tam model are compared to the measured jet noise component spectra. In order to obtain power spectral density in this case, the Tam model was programmed separately from the TAMSHK module in ANOPP (which produces only 1/3-octave spectra output.) The peak frequencies and the peak levels are in good agreement between the two predictions at the upstream angles. At 90 degrees and downstream, the two predictions deviate with higher peak frequencies predicted by the RANS-based model. When the spectral data are combined into 1/3-octave levels, the RANS-based model, the Tam model, and the 'Simplified' model are in general agreement in the peak frequency, the peak level, and the higher frequency broadband levels at all the directivity angles shown in the figure. The ST2JET predictions have the least agreement with the data at the higher frequencies and under predicts the peak frequencies and levels as the directivity angle increases downstream.

Figure 20 shows the hot jet results. There are larger differences between the shock-associated noise models for the hot jet than there were for the cold jet. There is agreement between the peak frequencies and levels at the upstream angles for the RANS-based model and the Tam model. But at higher frequencies, both models predict much lower levels than the measured data. At the downstream angles, both models deviate from each other and neither compare favorably with the data. The 1/3-octave spectra show some agreement in the peak frequency at the upstream angles, but a wide difference exists in the predictions for the higher frequency levels. At downstream angles, the predictions have even less agreement. In general for the nozzle and jet flow conditions in this case, the 'Simplified' model predictions give the best agreement with the measured data.

A summary of these prediction results in terms of the error in peak level and in peak Strouhal number are given in Figure 21 for the power spectral density results and in Figure 22 for the 1/3-octave band results. For the cold jet, Figure 21(a) shows that the Tam model has peak level errors varying between ± 2 dB and the RANS-based model ± 2.5 dB over the range of directivity angles. The peak Strouhal number error for both is less than 20%, Figure 21(b). When the jet is hot, both models have large peak amplitude errors in the downstream direction and the RANS-based model approaches 40% in the peak Strouhal number error. The errors derived from the 1/3-octave data, Figure 22, show similar results for the peak level errors for these two models. The 'Simplified' model exhibits less peak level error overall compared to the Tam and RANS-based models. The ST2JET model has much larger errors. The accuracy of using 1/3-octave spectra to determine the peak Strouhal number error depends on both the position of the peak relative to the 1/3-octave band cutoff frequencies and the quality of the measured spectra. At 90 degrees, for example, a screech tone exists near the peak of the broadband shock-associated noise spectrum that lowers the peak Strouhal number in the 1/3-octave spectrum. This results in a large peak Strouhal number error for the RANS-based predictions at 90 degrees.

7 Summary

An assessment has been completed of the predictive capability of jet mixing noise and jet broadband shock-associated noise prediction codes using an acoustic database created from the far-field noise measurements of single-stream, round, shock-containing jets operated at 24 under-expanded conditions covering a matrix of jet velocities and temperatures. The following is a summary for the five semi-empirical models that produced 1/3-octave spectra for comparison to the measured spectra from all the jet operating conditions. A summary of the assessment for the newer RANS-based model using two cases is given at the end of the previous section.

ANOPP Module SGLJET – The SGLJET module predicted the radiated jet mixing noise from supersonic jets issuing from a round, convergent nozzle at frequencies less than the peak frequency for shock-associated noise. The levels of predicted mixing noise were found to be in closer agreement to measured mixing noise component levels when the amplification effects were included in the mixing noise. Over the range of operating conditions for which measurements were taken, the SGLJET module predicted mixing noise levels within an accuracy variation of 5.7 dB or less for directivity angles of 50 to 120 degrees.

ANOPP Module ST2JET – The ST2JET module predicted the jet noise for both the mixing noise

and the shock-associated noise components radiated from a supersonic, shock-containing jet. The predicted mixing noise component was found to be in closer agreement to measured mixing noise levels with amplification with accuracy variations of 7.1 dB or less over the range of operating conditions for directivity angles of 50 to 120 degrees. The ST2JET module predicted the shock-associated noise peak level more accurately at 50 degrees, within a 3.8 dB variation, than at 90 degrees, a 6.8 dB variation. The high frequency levels for shock-associated noise were predicted consistently lower that the measured data. At 120 degrees, the ST2JET predictions were dominated by the mixing noise component of the model.

ANOPP Module SAESHK – The SAESHK module predicted the broadband shock-associated noise using the HBF model. The model gave reasonable predictions for shock-associated noise for lower speed jets and predicted the total jet noise spectra for higher speed jets including low frequency mixing noise at the 50 degree direction. The predictions at 90 degrees were still qualitatively good for peak shock-associated noise levels at lower jet temperatures but becoming less accurate with increasing jet temperature. At 120 degrees, there was little agreement between the SAESHK module predicted spectra and the measured spectra.

ANOPP Module TAMSHK – The broadband shock-associated noise model of Tam is based on the theory that large-scale turbulent structures generated in the supersonic jet mixing layer interact with the periodic-like shock cell structure that exists in imperfectly expanded jets. The TAMSHK module predicted the shock-associated noise peak levels with similar accuracy at 50 and 90 degrees, within 4.0 dB and 4.3 dB variations, respectively. The model predicted high frequency levels lower than measured levels especially as the jet speed increased. At 120 degrees, the model performed well for cold jets, but consistently predicted much lower spectral levels compared to measured levels for heated jets.

Simplified Shock-Associated Noise Model – The 'Simplified' model is an empirical correlation for the spectrum of shock-associated noise based on two straight lines that join at the peak of the spectrum. Between the extremes of tested jet velocities, this model gave consistent peak level predictions within about a 6 dB variation at all angles. There was a trend to predict higher levels than measured for higher temperature jets. The peak frequencies were predicted well except at 120 degrees where the peak frequencies were predicted to be higher than measured for higher speed jets.

References

[1] Dahl, M. D., "A Process for Assessing NASA's Capability in Aircraft Noise Prediction Technology," AIAA Paper No. 2008-2813, 2008.

[2] Bridges, J. E., Khavaran, A., and Hunter, C., "Assessment of Current Jet Noise Prediction Capabilities," AIAA Paper No. 2008-2933, 2008.

[3] Bridges, J. and Brown, C. A., "Validation of the Small Hot Jet Acoustic Rig for Aeroacoustic Research," AIAA Paper No. 2005-2846, 2005.

[4] Bridges, J. and Wernet, M. P., "Measurements of the Aeroacoustic Sound Sources in Hot Jets," AIAA Paper No. 2003-3130, 2003.

[5] Brown, C. A. and Bridges, J., "Small Hot Jet Acoustic Rig Validation," NASA TM-2006-214234, 2006.

[6] Bridges, J. and Wernet, M. P., "Effect of Temperature on Jet Velocity Spectra," AIAA Paper No. 2007-3628, 2007.

[7] Khavaran, A. and Bridges, J., "SHJAR Jet Noise Data and Power Spectral Laws," NASA TM-2009-215608, 2009.

[8] NACA Ames Research Staff, "Equations, Tables, and Charts for Compressible Flow," NACA Report 1135, 1953.

[9] Khavaran, A. and Bridges, J., "Development of Jet Noise Power Spectral Laws Using SHJAR Data," AIAA Paper No. 2009-3378, 2009.

[10] Deneuville, P. and Jacques, J., "Jet Noise Amplification: A Practically Important Problem," AIAA Paper No. 77-1368, 1977.

[11] Zorumski, W. E., "Aircraft Noise Prediction Program Theoretical Manual, Parts 1 & 2, (Revised)," NASA TM-83199, February 1982.

[12] SAE, "Gas Turbine Jet Exhaust Noise Prediction," ARP876 Rev. E, SAE International, 2006.

[13] Harper-Bourne, M. and Fisher, M. J., "The Noise from Shock Waves in Supersonic Jets," *Noise Mechanisms*, AGARD-CP-131, 1974, pp. 11.1–11.13.

[14] Deneuville, P., "Simplified Prediction Method of Shock Cell Noise of Supersonic Jets from Conical Nozzles," SNECMA YKA No. 5982/76, Societe Nationale d'Edute et de Construction de Moteurs d'Avion, France, 1976.

[15] Balsa, T. F., Gliebe, P. R., Kantola, R. A., Mani, R., Stringes, E. J., and Wang, J. F. C., "High Velocity Jet Noise Source Location and Reduction. Task 2. Theoretical Developments and Basic Experiments; Final Report," FAA-RD-76-79-2, FAA, 1978.

[16] Tam, C. K. W., "Forward Flight Effects on Broadband Shock Associated Noise of Supersonic Jets," AIAA Paper No. 89-1088, 1989.

[17] Tam, C. K. W., "Broadband Shock-Associated Noise of Moderately Imperfectly Expanded Supersonic Jets," *J. Sound Vib.*, Vol. 140, No. 1, 1990, pp. 55–71.

[18] Gliebe, P. R., Motsinger, R. E., and Sieckman, A., "High Velocity Jet Noise Source Location and Reduction. Task 6. Supplement. Computer Programs: Engineering Correlation (MS) Jet Noise Prediction Method and Unified Aeroacoustic Prediction Model (M*G*B) for Nozzles of Arbitrary Shape; Final Report," FAA-RD-76-79-6A, FAA, 1979.

[19] Morris, P. J. and Miller, S. A. E., "The Prediction of Broadband Shock-Associated Noise Using RANS CFD," AIAA Paper No. 2009-3315, 2009.

[20] Tanna, H. K., "An Experimental Study of Jet Noise, Part II: Shock Associated Noise," *J. Sound Vib.*, Vol. 50, 1977, pp. 429–444.

Rdg	T_t/T_∞	NPR	M_j	V_j/c_∞	β	γ_j	T_∞(K)	p_∞(Pa)	c_∞(m/s)
2079	1.01	2.005	1.049	0.954	0.315	1.4000	279.4	97789	335.04
2080	1.01	2.358	1.178	1.047	0.623	1.4000	279.2	97783	334.92
2081	1.01	3.147	1.392	1.186	0.969	1.4000	279.2	97788	334.93
2082	1.01	3.636	1.493	1.245	1.109	1.4000	279.2	97790	334.93
2083	1.01	4.647	1.660	1.338	1.325	1.4000	279.2	97796	334.89
2085	1.01	5.708	1.796	1.406	1.491	1.4000	279.1	97794	334.87
2088	1.77	2.004	1.050	1.264	0.319	1.3951	280.1	97814	335.44
2089	1.77	2.365	1.182	1.388	0.630	1.3963	280.2	97817	335.52
2090	1.76	3.143	1.392	1.568	0.968	1.3978	280.2	97826	335.49
2091	1.76	3.627	1.492	1.647	1.108	1.3983	280.2	97831	335.50
2092	1.77	4.644	1.660	1.775	1.325	1.3990	280.0	97826	335.37
2093	1.76	5.674	1.792	1.858	1.487	1.3994	279.8	97814	335.30
2100	2.16	1.989	1.045	1.390	0.305	1.3872	279.9	97851	335.34
2098	2.16	2.356	1.181	1.533	0.628	1.3896	279.9	97842	335.34
2097	2.16	3.130	1.390	1.734	0.966	1.3929	279.8	97837	335.25
2096	2.16	3.629	1.494	1.828	1.109	1.3942	279.6	97839	335.18
2095	2.16	4.638	1.659	1.959	1.324	1.3961	279.6	97825	335.16
2094	2.16	5.685	1.794	2.056	1.489	1.3973	279.7	97830	335.23
2102	2.66	1.987	1.048	1.542	0.314	1.3736	280.2	97865	335.54
2103	2.65	2.327	1.175	1.691	0.617	1.3769	280.3	97857	335.58
2104	2.66	3.120	1.391	1.926	0.967	1.3823	280.3	97859	335.59
2105	2.65	3.597	1.490	2.020	1.105	1.3849	280.4	97864	335.61
2106	2.64	4.630	1.660	2.168	1.325	1.3889	280.4	97857	335.61
2107	2.65	5.638	1.789	2.276	1.484	1.3913	280.3	97854	335.58

Table 1: Test conditions for a convergent nozzle designated smc021 grouped according to total temperature.

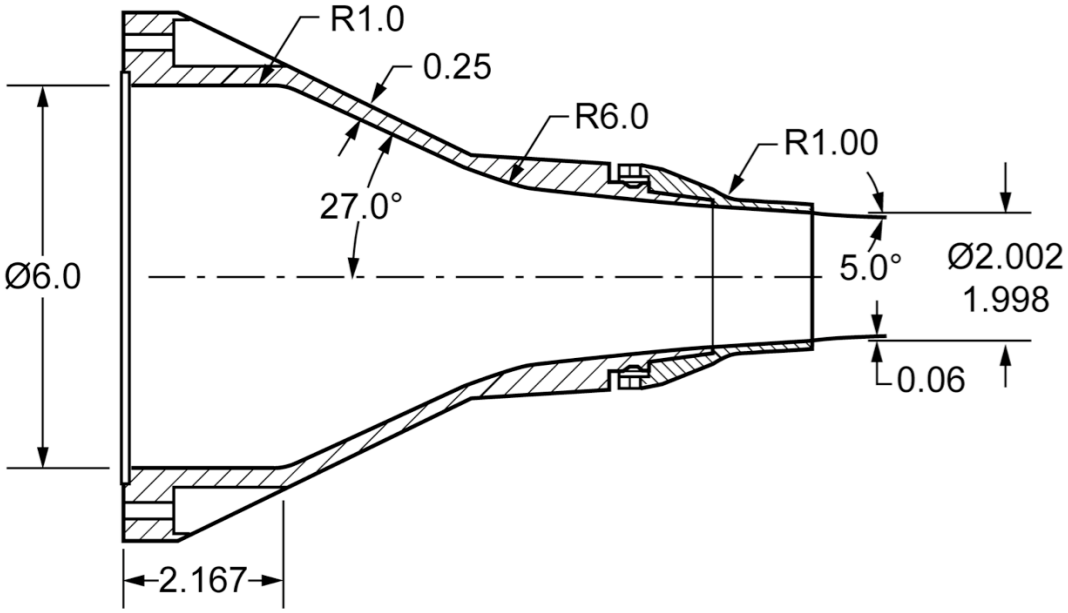

Figure 1: Diagram of the smc000 nozzle.

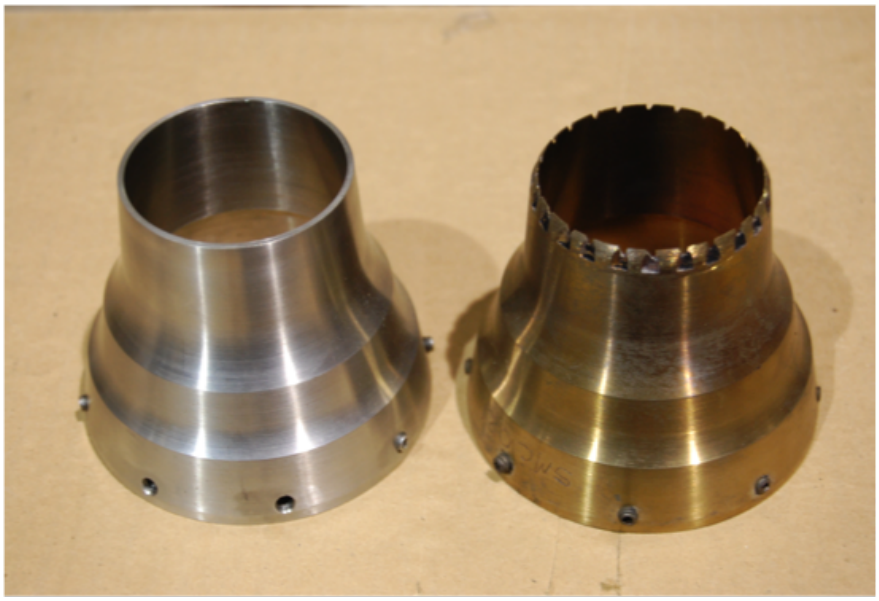

Figure 2: Nozzles: smc000 on the left, smc021 on the right.

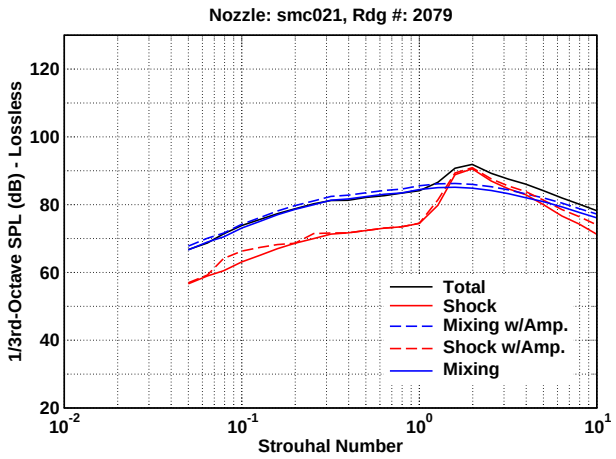

(a) $M_j = 1.049, \text{NPR} = 2.005, T_t/T_\infty = 1.01$

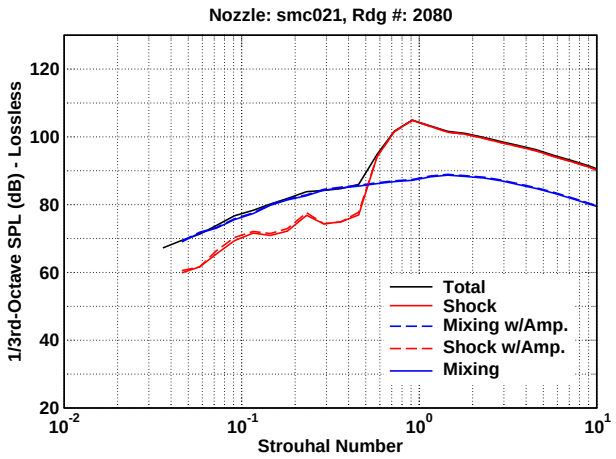

(b) $M_j = 1.178, \text{NPR} = 2.358, T_t/T_\infty = 1.01$

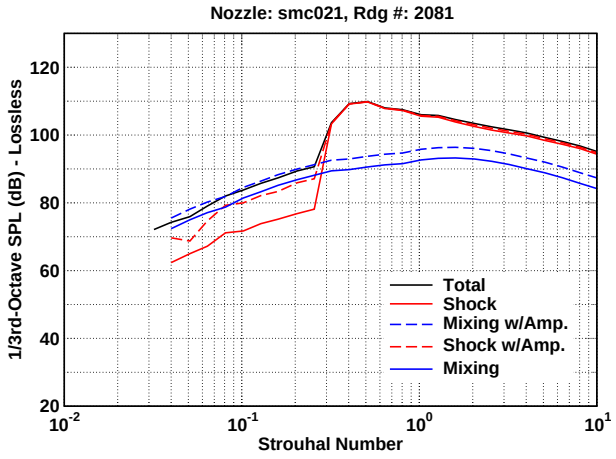

(c) $M_j = 1.392, \text{NPR} = 3.147, T_t/T_\infty = 1.01$

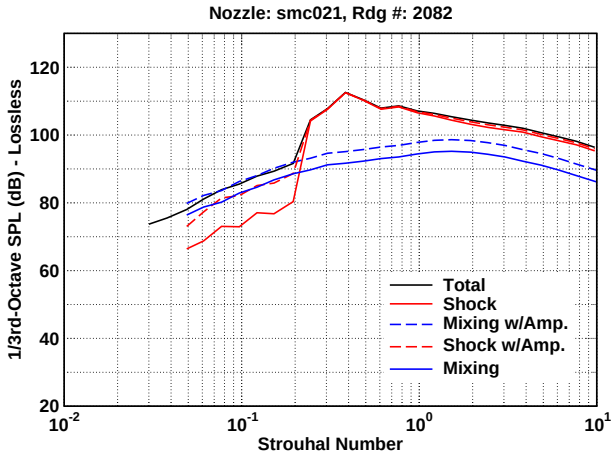

(d) $M_j = 1.493, \text{NPR} = 3.636, T_t/T_\infty = 1.01$

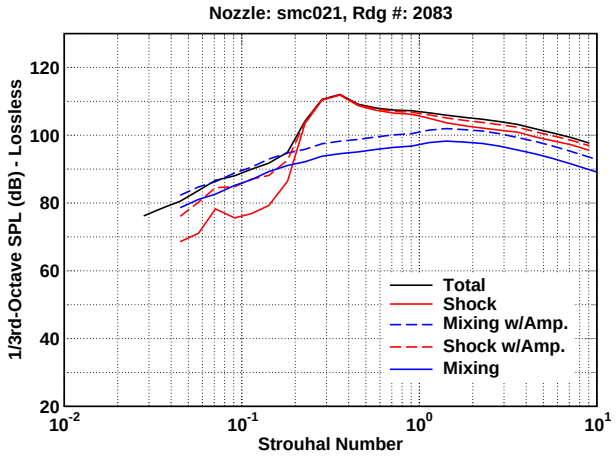

(e) $M_j = 1.660, \text{NPR} = 4.647, T_t/T_\infty = 1.01$

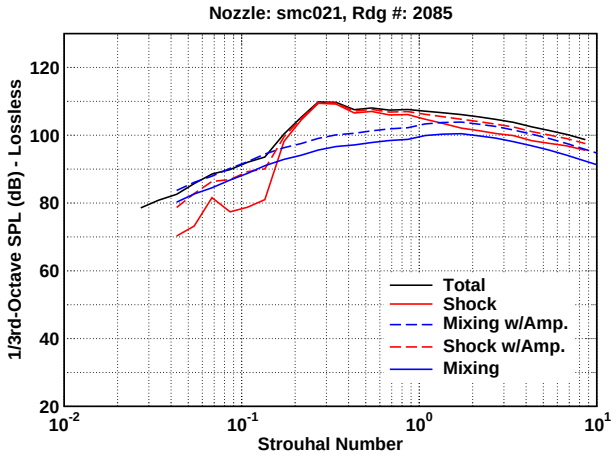

(f) $M_j = 1.796, \text{NPR} = 5.708, T_t/T_\infty = 1.01$

Figure 3: 1/3-Octave measured total jet noise spectra and derived jet noise component spectra from jets with shocks at a 50 degree inlet angle and distance $100D$.

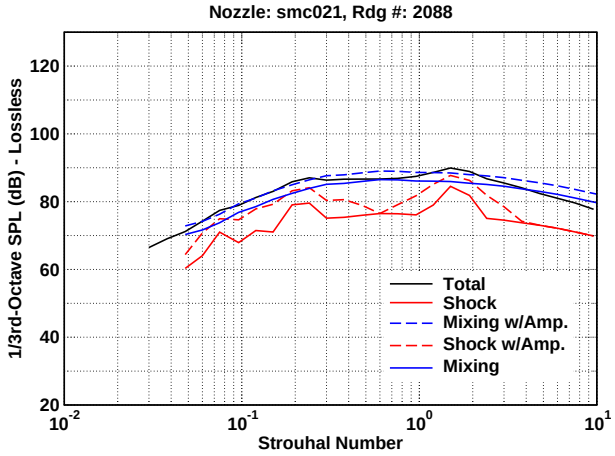

(g) $M_j = 1.050, \mathrm{NPR} = 2.004, T_t/T_\infty = 1.77$

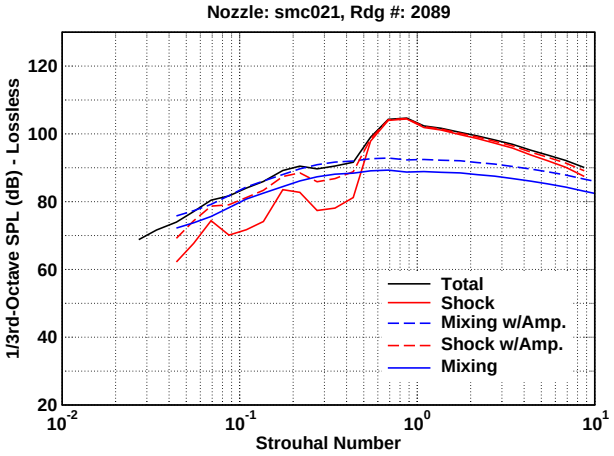

(h) $M_j = 1.182, \mathrm{NPR} = 2.365, T_t/T_\infty = 1.77$

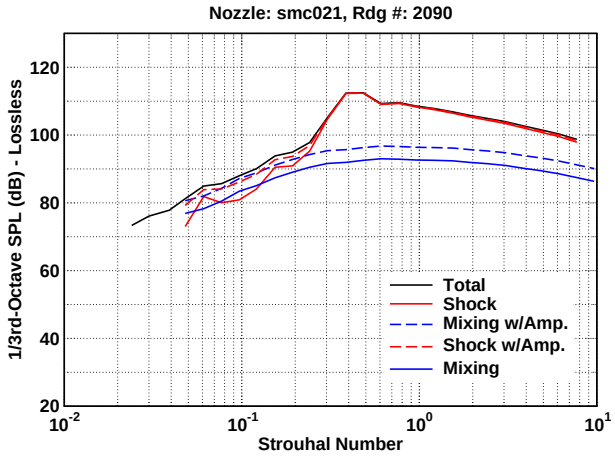

(i) $M_j = 1.392, \mathrm{NPR} = 3.143, T_t/T_\infty = 1.76$

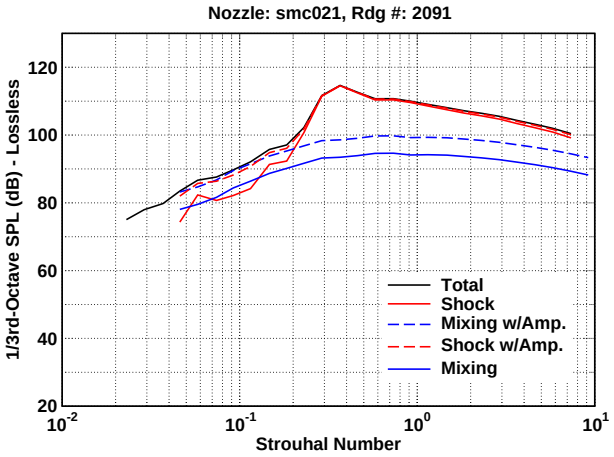

(j) $M_j = 1.492, \mathrm{NPR} = 3.627, T_t/T_\infty = 1.76$

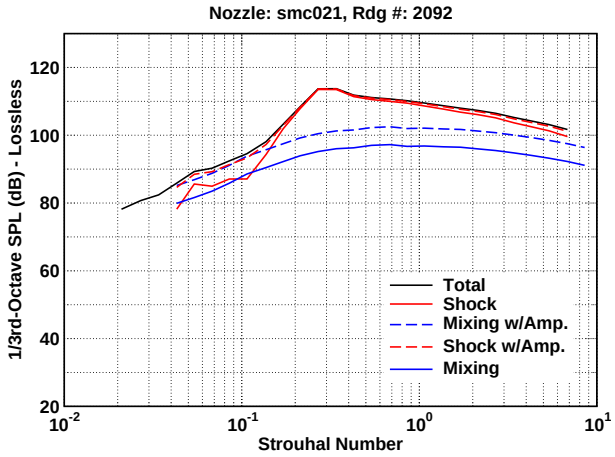

(k) $M_j = 1.660, \mathrm{NPR} = 4.644, T_t/T_\infty = 1.77$

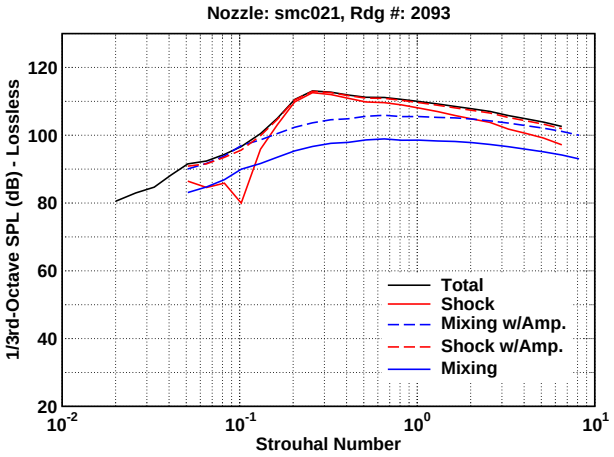

(l) $M_j = 1.792, \mathrm{NPR} = 5.674, T_t/T_\infty = 1.76$

Figure 3: (50 Deg., Cont.)

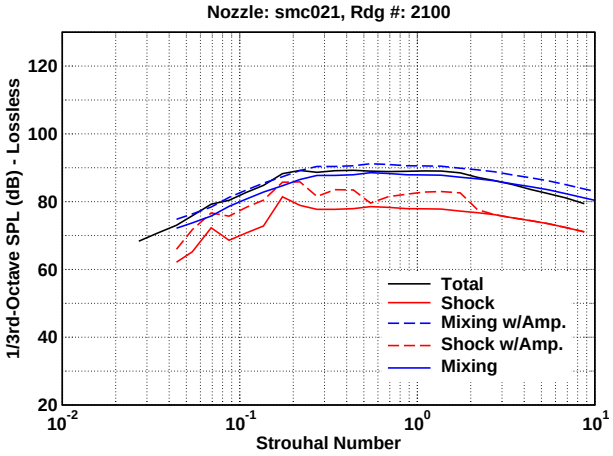

(m) $M_j = 1.045, \text{NPR} = 1.989, T_t/T_\infty = 2.16$

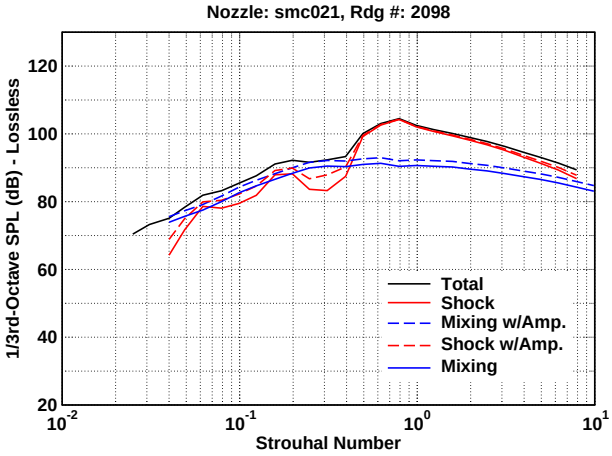

(n) $M_j = 1.181, \text{NPR} = 2.356, T_t/T_\infty = 2.16$

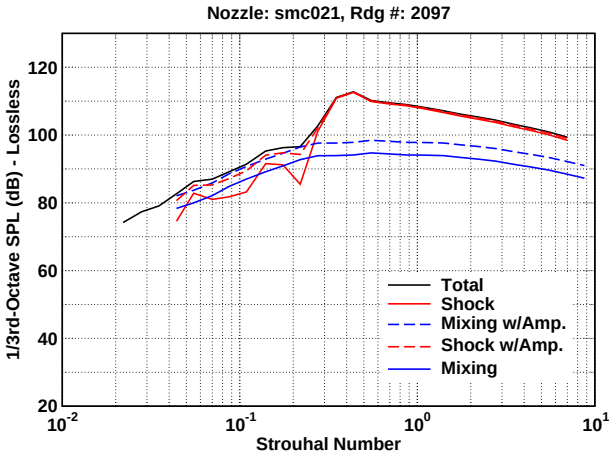

(o) $M_j = 1.390, \text{NPR} = 3.130, T_t/T_\infty = 2.16$

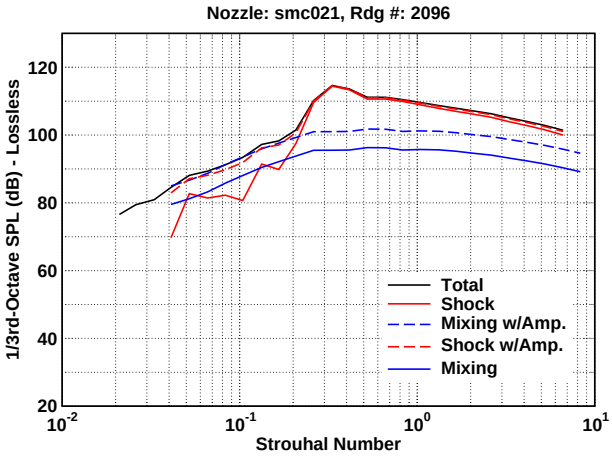

(p) $M_j = 1.494, \text{NPR} = 3.629, T_t/T_\infty = 2.16$

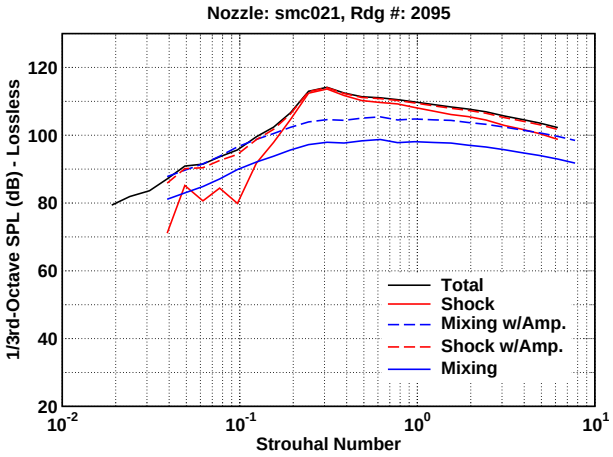

(q) $M_j = 1.660, \text{NPR} = 4.638, T_t/T_\infty = 2.16$

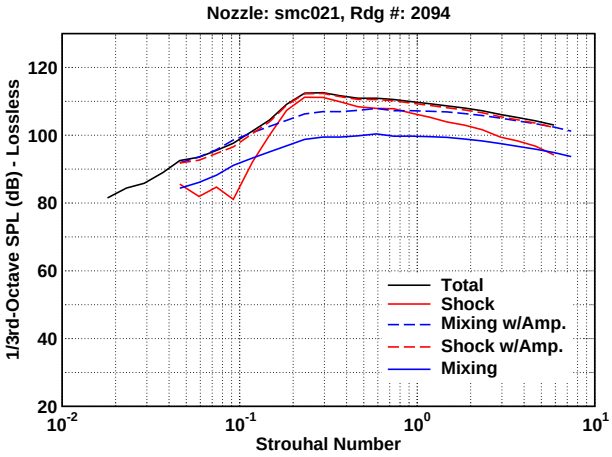

(r) $M_j = 1.794, \text{NPR} = 5.685, T_t/T_\infty = 2.16$

Figure 3: (50 Deg., Cont.)

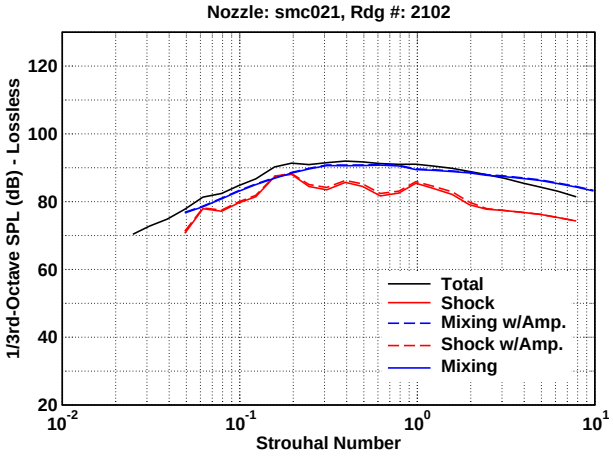

(s) $M_j = 1.048, \mathrm{NPR} = 1.987, T_t/T_\infty = 2.66$

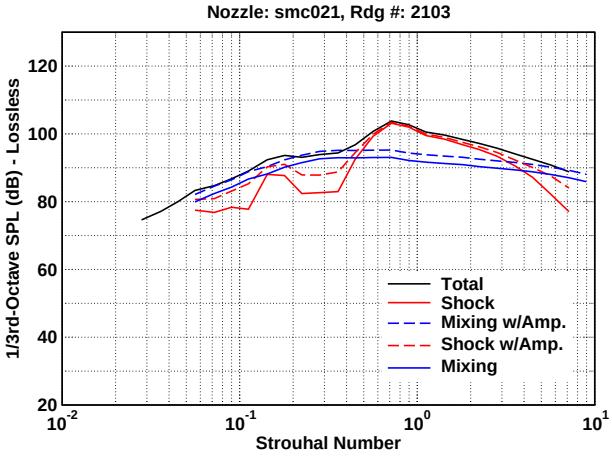

(t) $M_j = 1.175, \mathrm{NPR} = 2.327, T_t/T_\infty = 2.65$

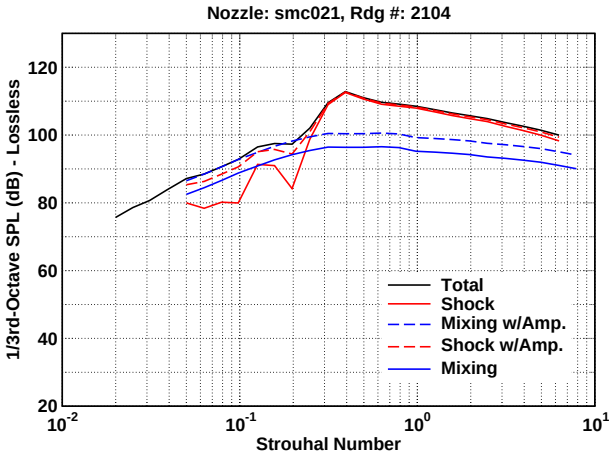

(u) $M_j = 1.391, \mathrm{NPR} = 3.120, T_t/T_\infty = 2.66$

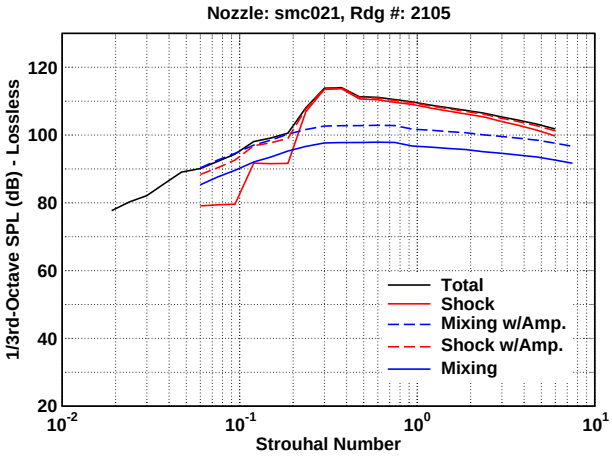

(v) $M_j = 1.490, \mathrm{NPR} = 3.597, T_t/T_\infty = 2.65$

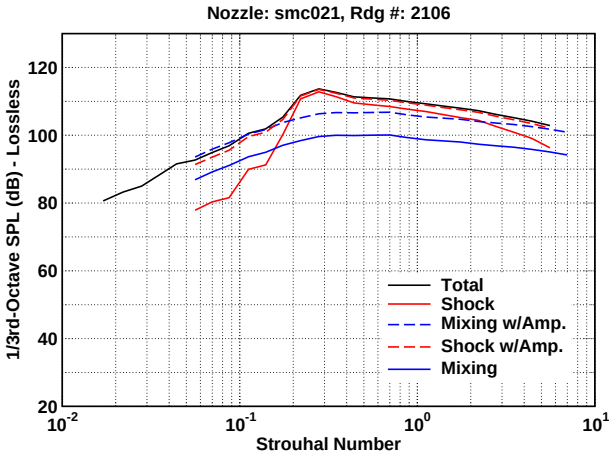

(w) $M_j = 1.660, \mathrm{NPR} = 4.630, T_t/T_\infty = 2.64$

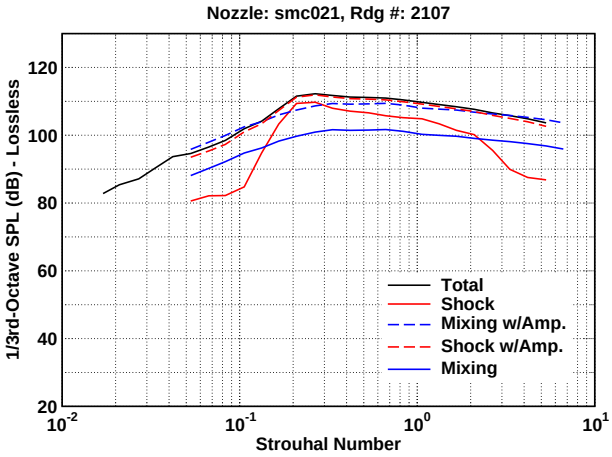

(x) $M_j = 1.789, \mathrm{NPR} = 5.638, T_t/T_\infty = 2.65$

Figure 3: (50 Deg., Cont.)

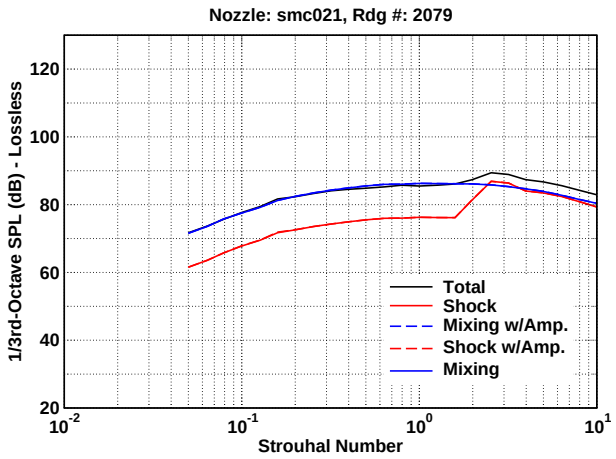

(a) $M_j = 1.049, \text{NPR} = 2.005, T_t/T_\infty = 1.01$

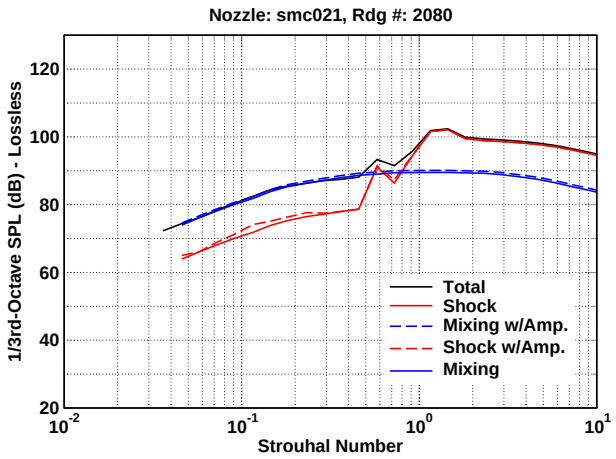

(b) $M_j = 1.178, \text{NPR} = 2.358, T_t/T_\infty = 1.01$

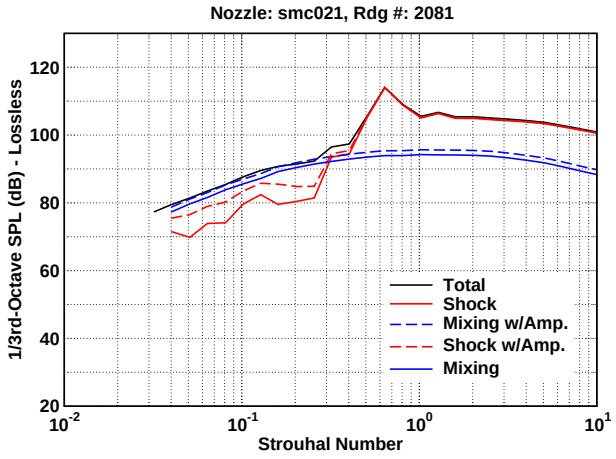

(c) $M_j = 1.392, \text{NPR} = 3.147, T_t/T_\infty = 1.01$

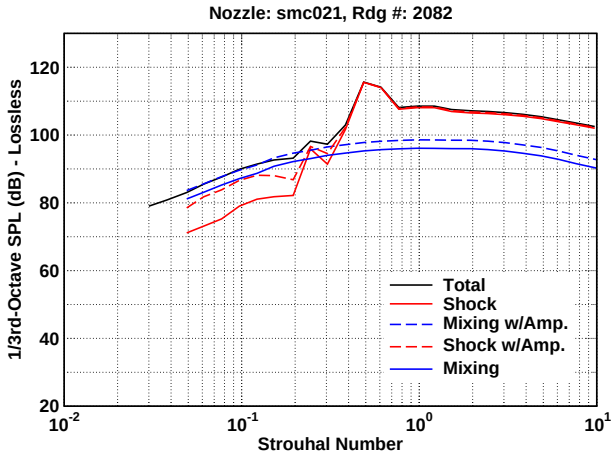

(d) $M_j = 1.493, \text{NPR} = 3.636, T_t/T_\infty = 1.01$

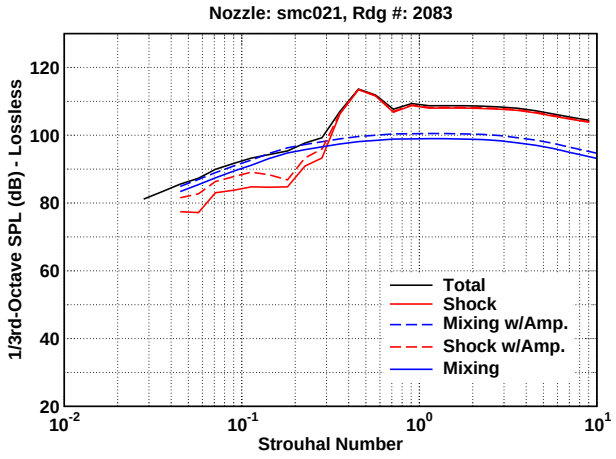

(e) $M_j = 1.660, \text{NPR} = 4.647, T_t/T_\infty = 1.01$

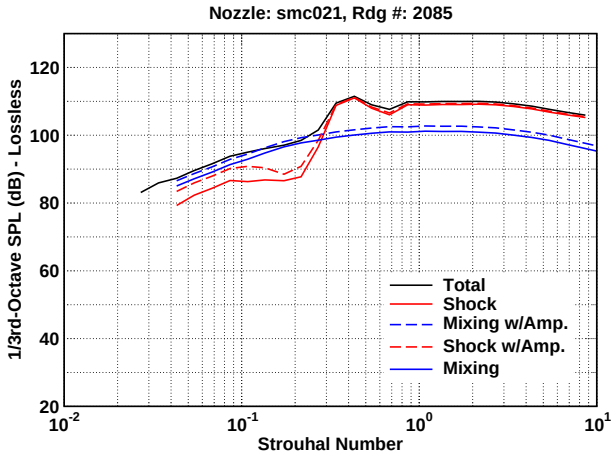

(f) $M_j = 1.796, \text{NPR} = 5.708, T_t/T_\infty = 1.01$

Figure 4: 1/3-Octave measured total jet noise spectra and derived jet noise component spectra from jets with shocks at a 90 degree inlet angle and distance $100D$.

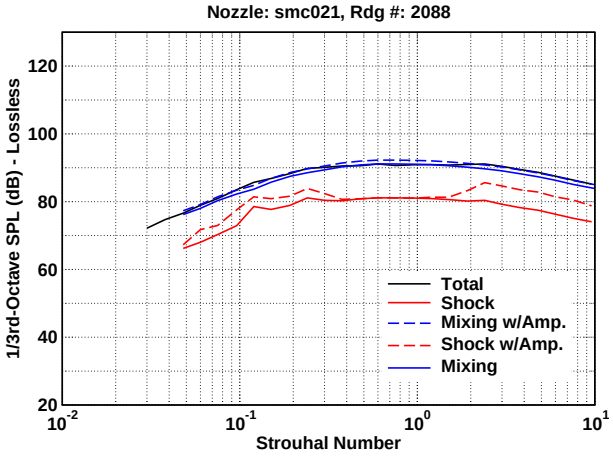

(g) $M_j = 1.049, \text{NPR} = 2.004, T_t/T_\infty = 1.77$

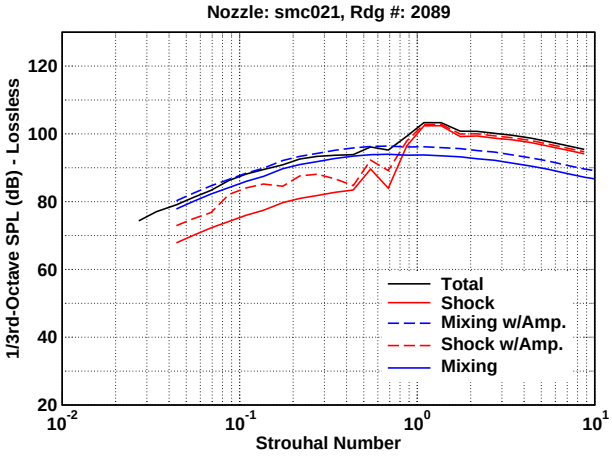

(h) $M_j = 1.182, \text{NPR} = 2.365, T_t/T_\infty = 1.77$

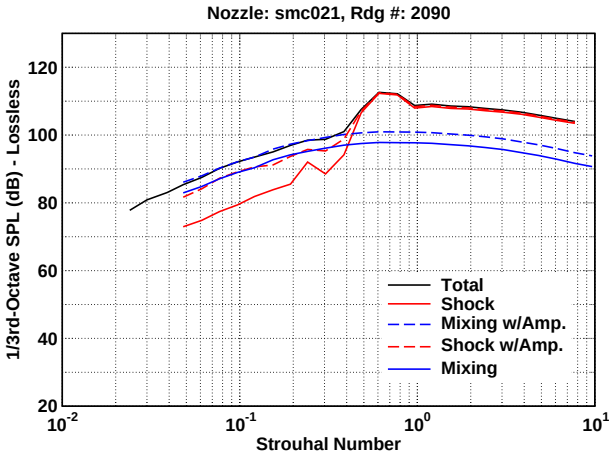

(i) $M_j = 1.392, \text{NPR} = 3.143, T_t/T_\infty = 1.76$

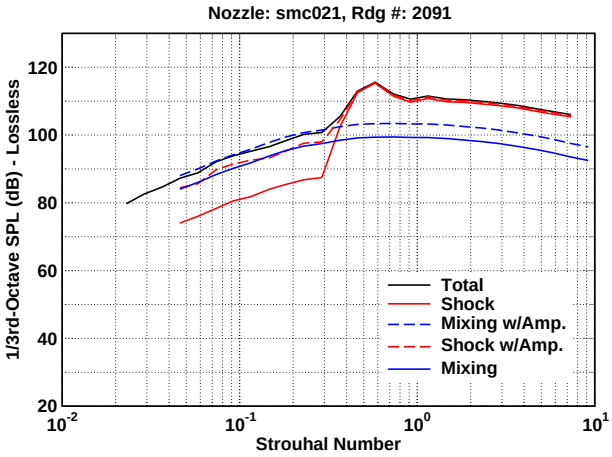

(j) $M_j = 1.492, \text{NPR} = 3.627, T_t/T_\infty = 1.76$

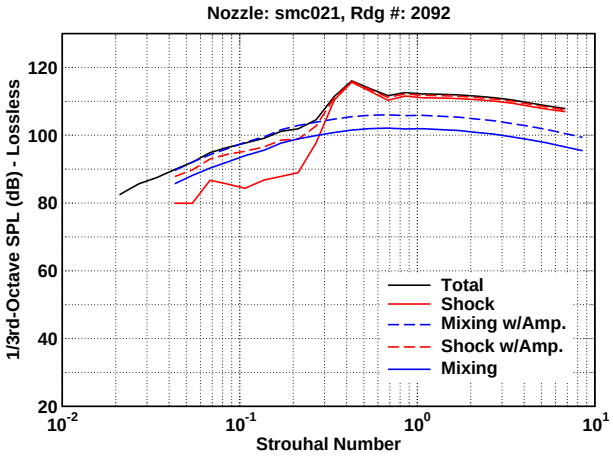

(k) $M_j = 1.660, \text{NPR} = 4.644, T_t/T_\infty = 1.77$

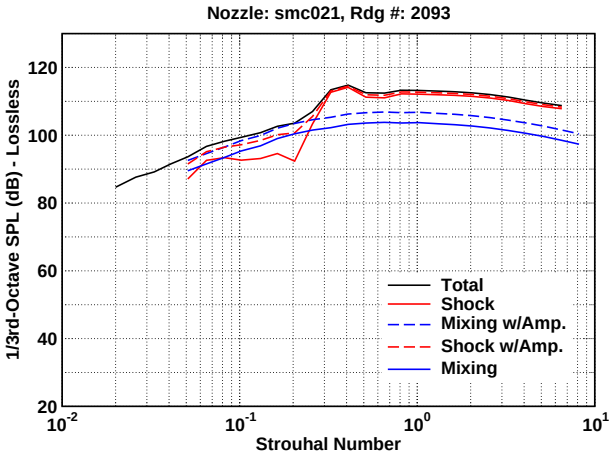

(l) $M_j = 1.792, \text{NPR} = 5.674, T_t/T_\infty = 1.76$

Figure 4: (90 Deg., Cont.)

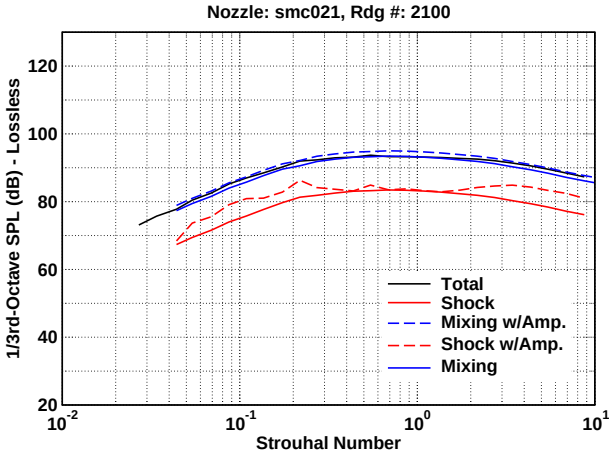

(m) $M_j = 1.045, \text{NPR} = 1.989, T_t/T_\infty = 2.16$

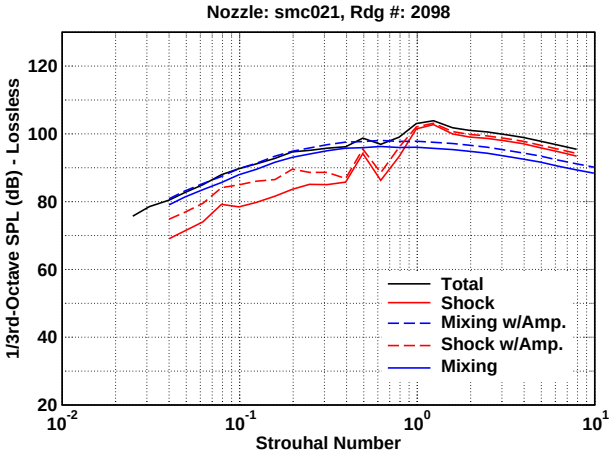

(n) $M_j = 1.181, \text{NPR} = 2.356, T_t/T_\infty = 2.16$

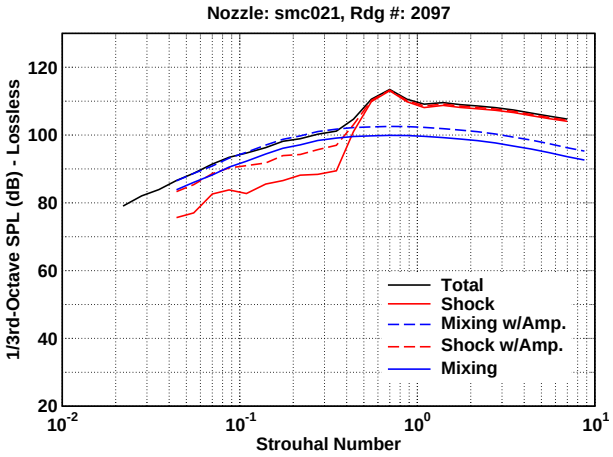

(o) $M_j = 1.390, \text{NPR} = 3.130, T_t/T_\infty = 2.16$

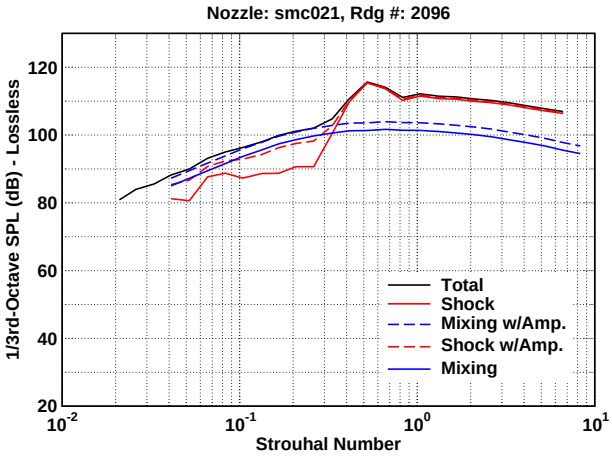

(p) $M_j = 1.494, \text{NPR} = 3.629, T_t/T_\infty = 2.16$

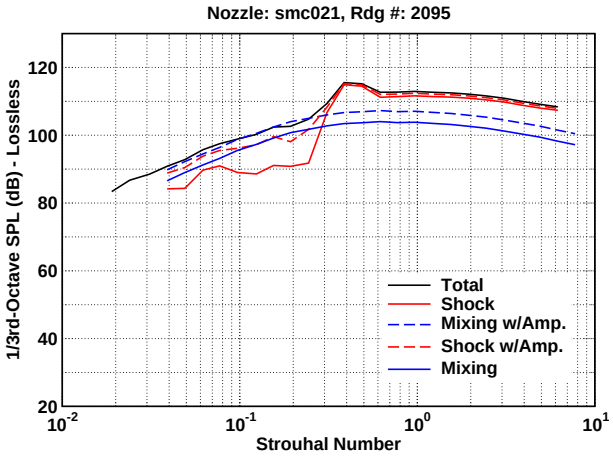

(q) $M_j = 1.660, \text{NPR} = 4.638, T_t/T_\infty = 2.16$

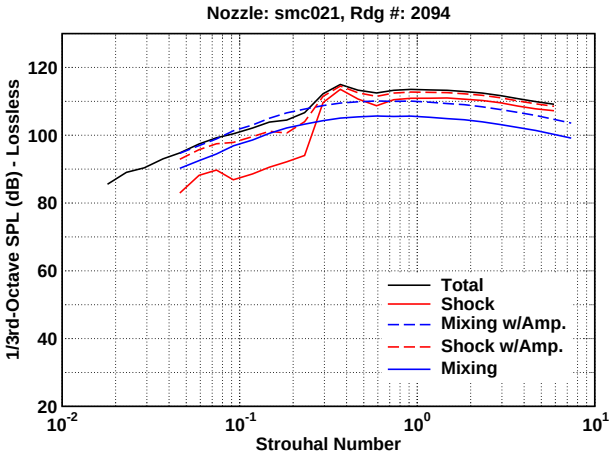

(r) $M_j = 1.794, \text{NPR} = 5.685, T_t/T_\infty = 2.16$

Figure 4: (90 Deg., Cont.)

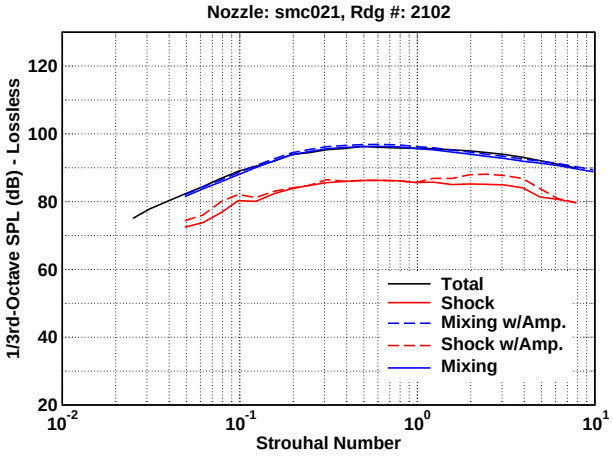

(s) $M_j = 1.048, \mathrm{NPR} = 1.987, T_t/T_\infty = 2.66$

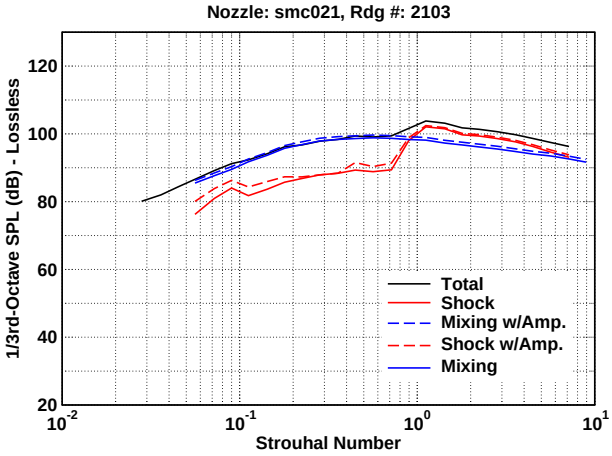

(t) $M_j = 1.175, \mathrm{NPR} = 2.327, T_t/T_\infty = 2.65$

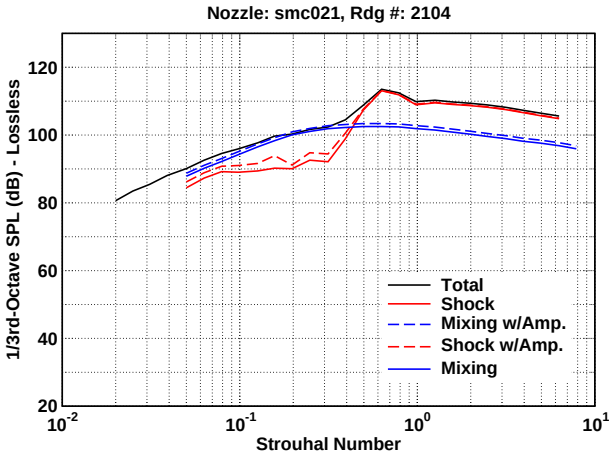

(u) $M_j = 1.391, \mathrm{NPR} = 3.120, T_t/T_\infty = 2.66$

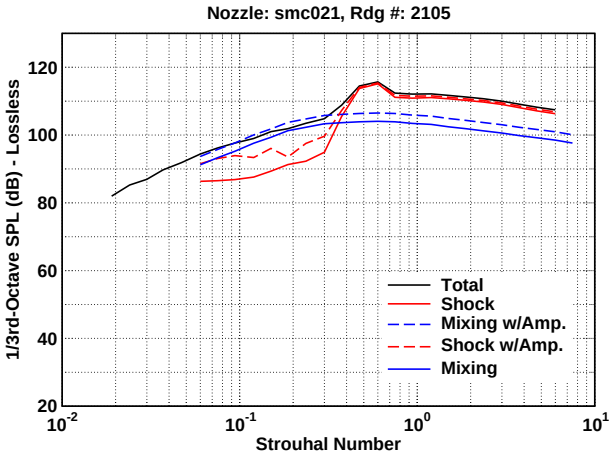

(v) $M_j = 1.490, \mathrm{NPR} = 3.597, T_t/T_\infty = 2.65$

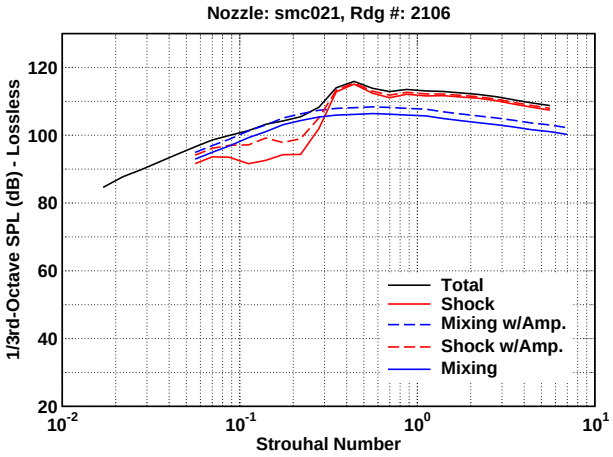

(w) $M_j = 1.660, \mathrm{NPR} = 4.630, T_t/T_\infty = 2.64$

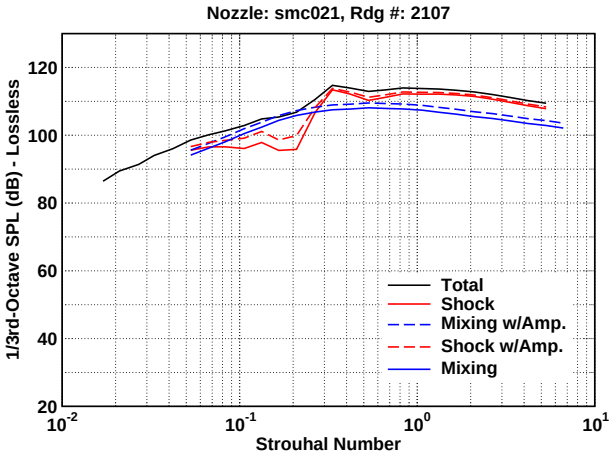

(x) $M_j = 1.789, \mathrm{NPR} = 5.638, T_t/T_\infty = 2.65$

Figure 4: (90 Deg., Cont.)

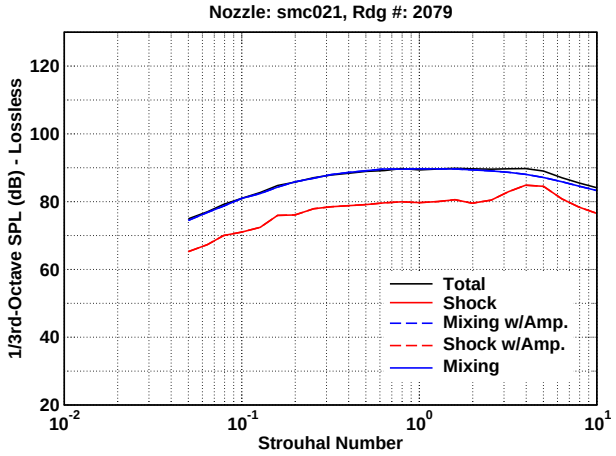

(a) $M_j = 1.049, \text{NPR} = 2.005, T_t/T_\infty = 1.01$

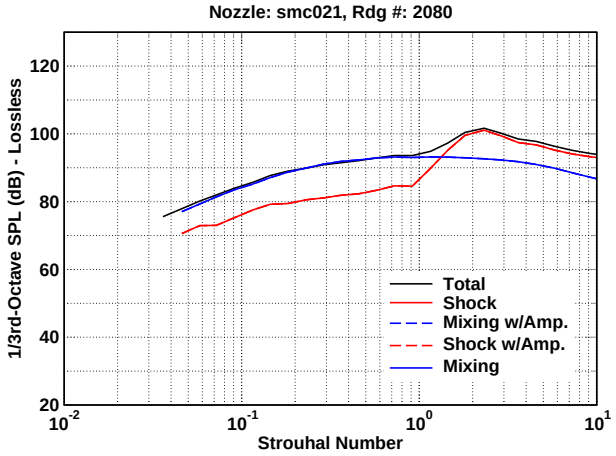

(b) $M_j = 1.178, \text{NPR} = 2.358, T_t/T_\infty = 1.01$

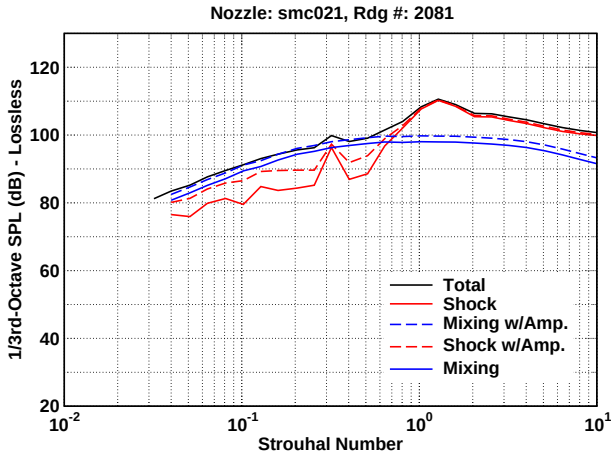

(c) $M_j = 1.392, \text{NPR} = 3.147, T_t/T_\infty = 1.01$

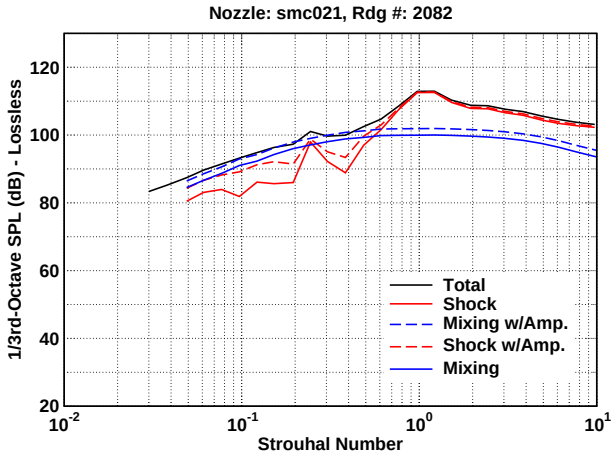

(d) $M_j = 1.493, \text{NPR} = 3.636, T_t/T_\infty = 1.01$

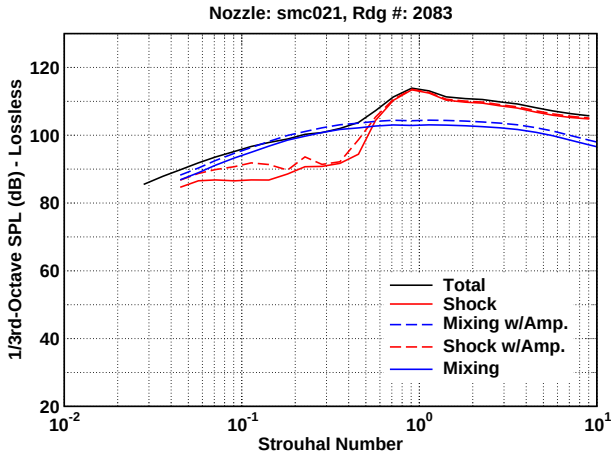

(e) $M_j = 1.660, \text{NPR} = 4.647, T_t/T_\infty = 1.01$

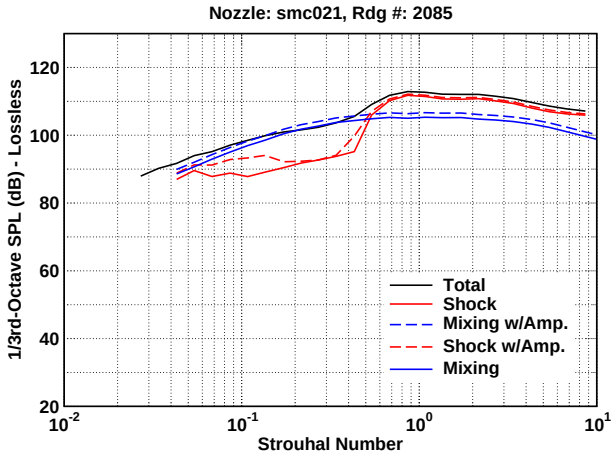

(f) $M_j = 1.796, \text{NPR} = 5.708, T_t/T_\infty = 1.01$

Figure 5: 1/3-Octave measured total jet noise spectra and derived jet noise component spectra from jets with shocks at a 120 degree inlet angle and distance $100D$.

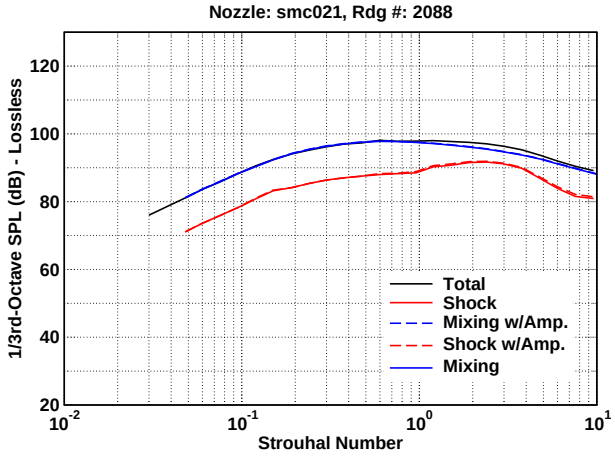

(g) $M_j = 1.049, \mathrm{NPR} = 2.004, T_t/T_\infty = 1.77$

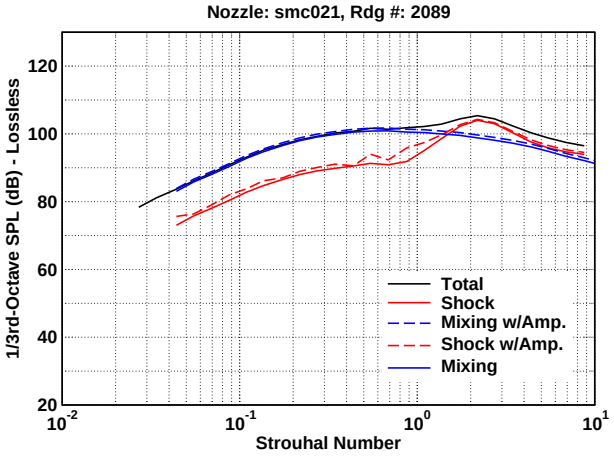

(h) $M_j = 1.182, \mathrm{NPR} = 2.365, T_t/T_\infty = 1.77$

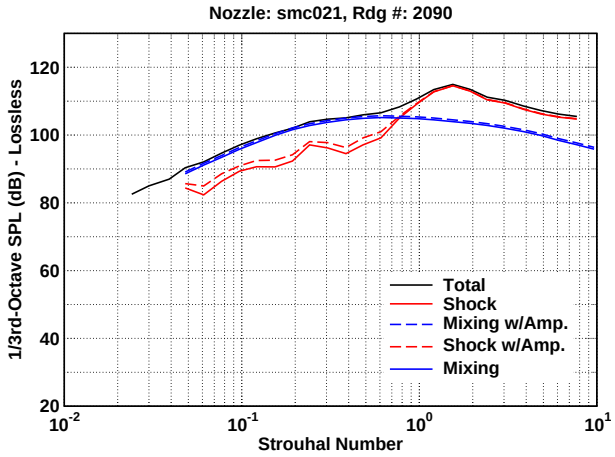

(i) $M_j = 1.392, \mathrm{NPR} = 3.143, T_t/T_\infty = 1.76$

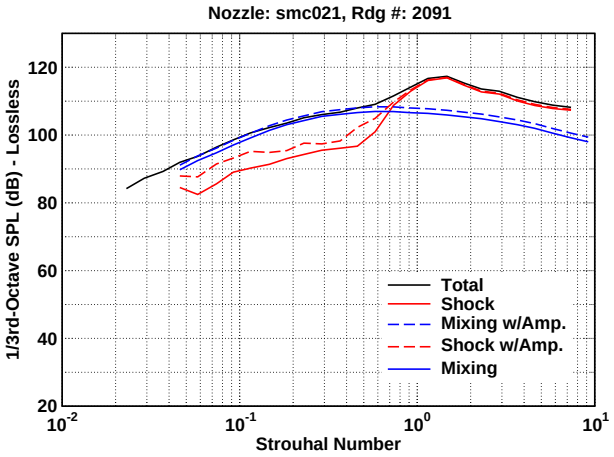

(j) $M_j = 1.492, \mathrm{NPR} = 3.627, T_t/T_\infty = 1.76$

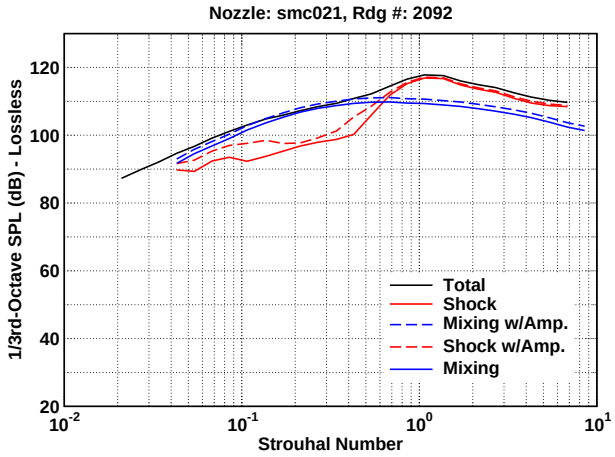

(k) $M_j = 1.660, \mathrm{NPR} = 4.644, T_t/T_\infty = 1.77$

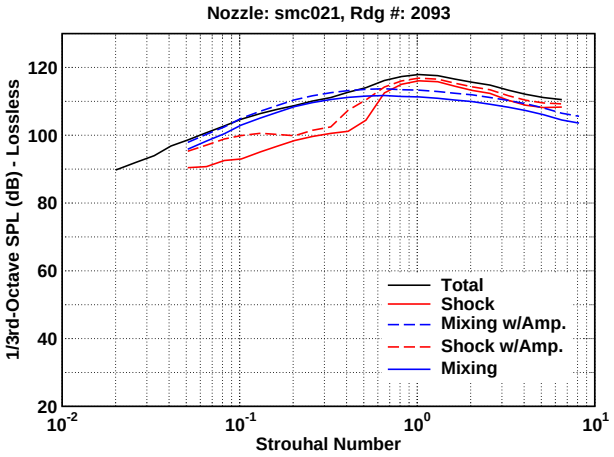

(l) $M_j = 1.792, \mathrm{NPR} = 5.674, T_t/T_\infty = 1.76$

Figure 5: (120 Deg., Cont.)

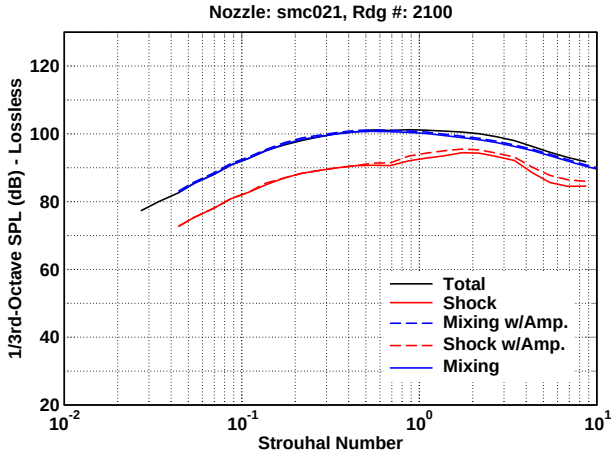

(m) $M_j = 1.045, \text{NPR} = 1.989, T_t/T_\infty = 2.16$

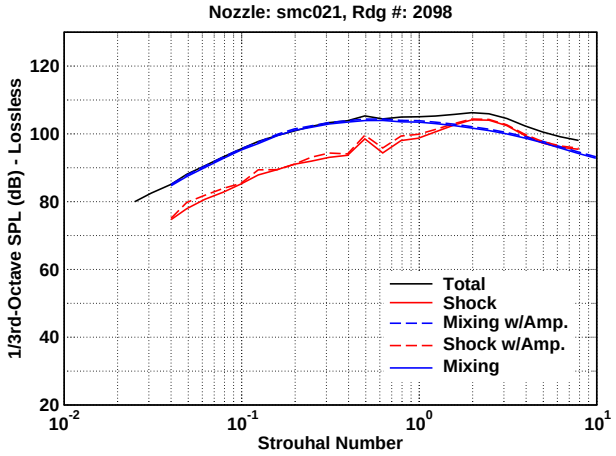

(n) $M_j = 1.181, \text{NPR} = 2.356, T_t/T_\infty = 2.16$

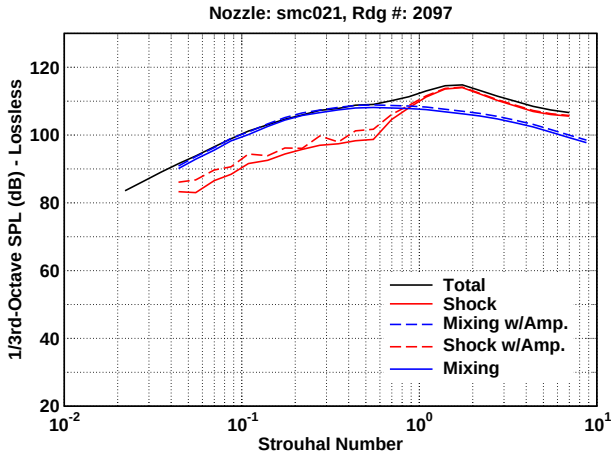

(o) $M_j = 1.390, \text{NPR} = 3.130, T_t/T_\infty = 2.16$

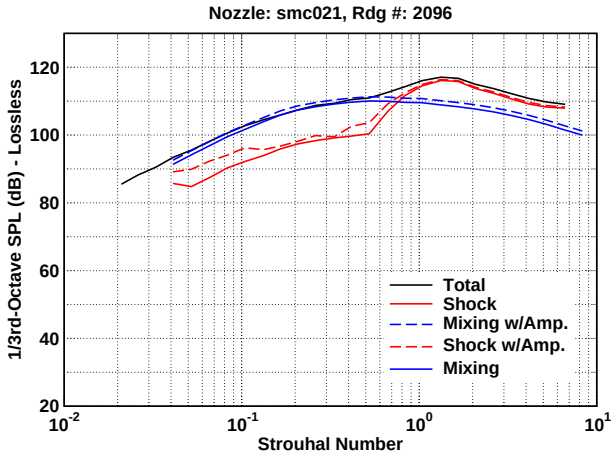

(p) $M_j = 1.494, \text{NPR} = 3.629, T_t/T_\infty = 2.16$

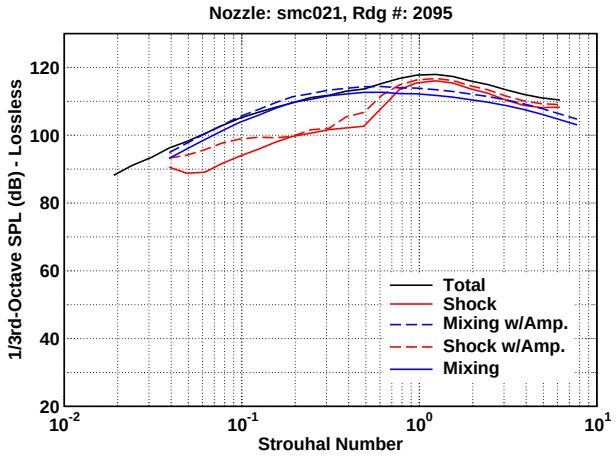

(q) $M_j = 1.660, \text{NPR} = 4.638, T_t/T_\infty = 2.16$

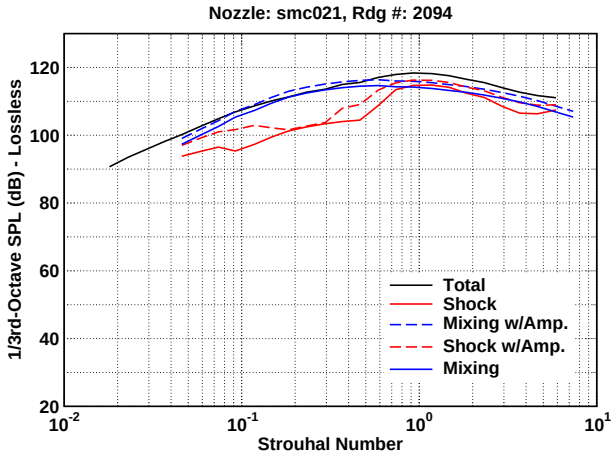

(r) $M_j = 1.794, \text{NPR} = 5.685, T_t/T_\infty = 2.16$

Figure 5: (120 Deg., Cont.)

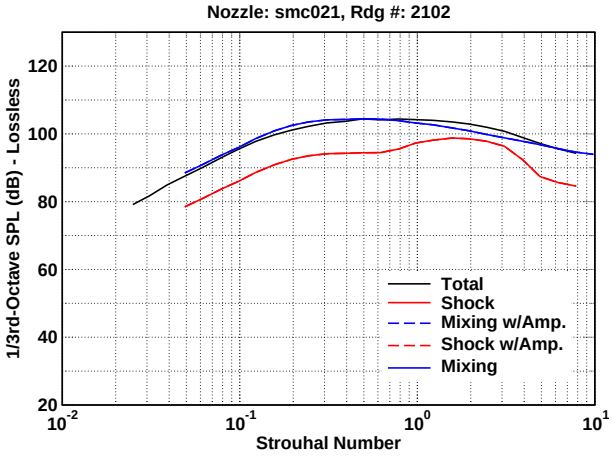

(s) $M_j = 1.048, \text{NPR} = 1.987, T_t/T_\infty = 2.66$

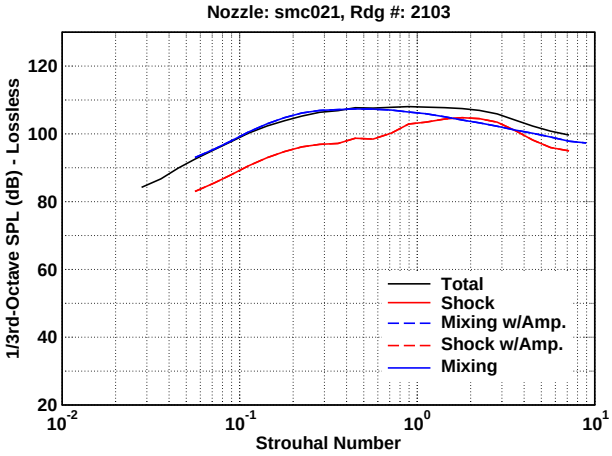

(t) $M_j = 1.175, \text{NPR} = 2.327, T_t/T_\infty = 2.65$

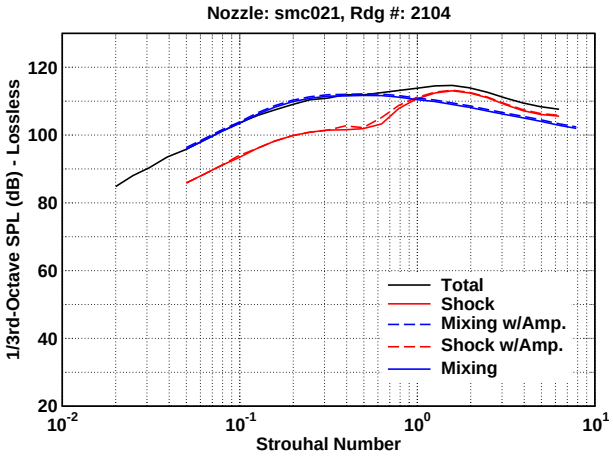

(u) $M_j = 1.391, \text{NPR} = 3.120, T_t/T_\infty = 2.66$

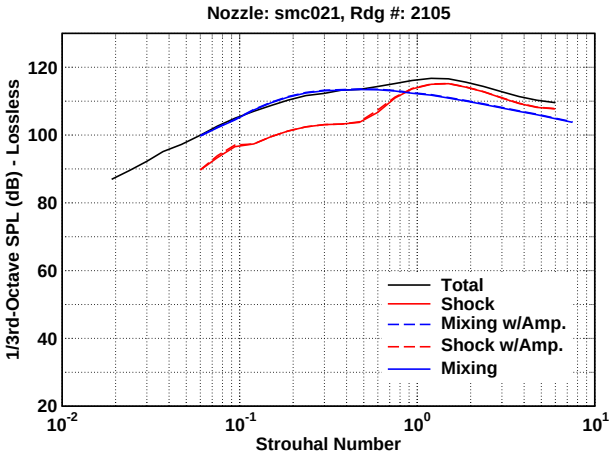

(v) $M_j = 1.490, \text{NPR} = 3.597, T_t/T_\infty = 2.65$

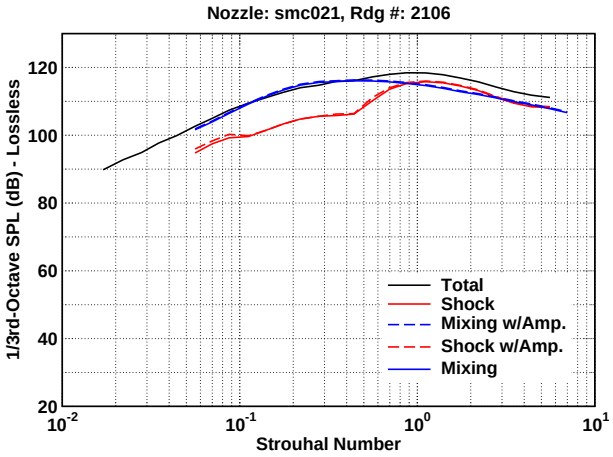

(w) $M_j = 1.660, \text{NPR} = 4.630, T_t/T_\infty = 2.64$

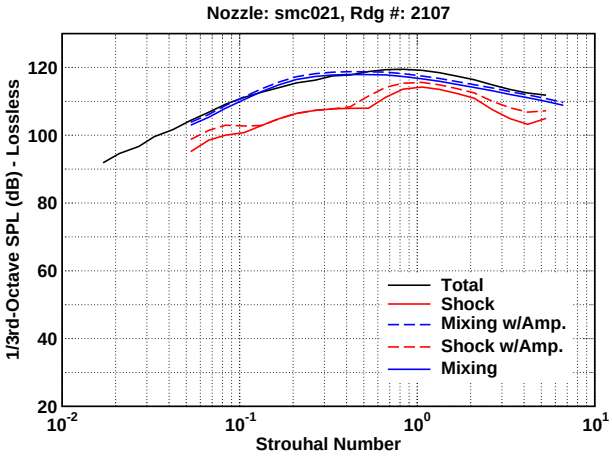

(x) $M_j = 1.789, \text{NPR} = 5.638, T_t/T_\infty = 2.65$

Figure 5: (120 Deg., Cont.)

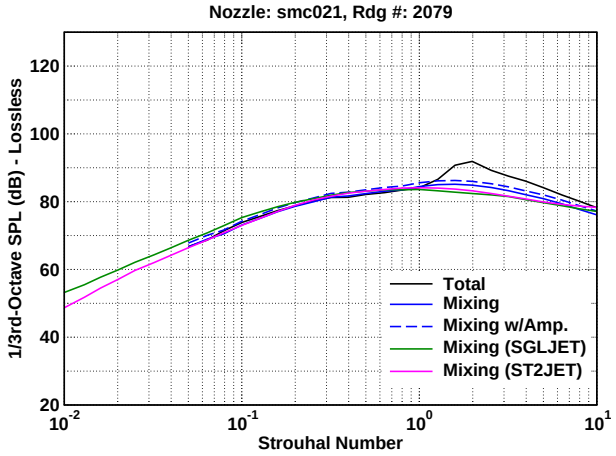

(a) $M_j = 1.049, \text{NPR} = 2.005, T_t/T_\infty = 1.01$

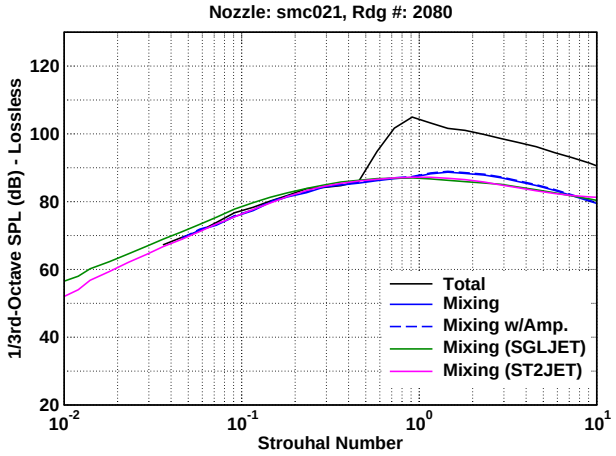

(b) $M_j = 1.178, \text{NPR} = 2.358, T_t/T_\infty = 1.01$

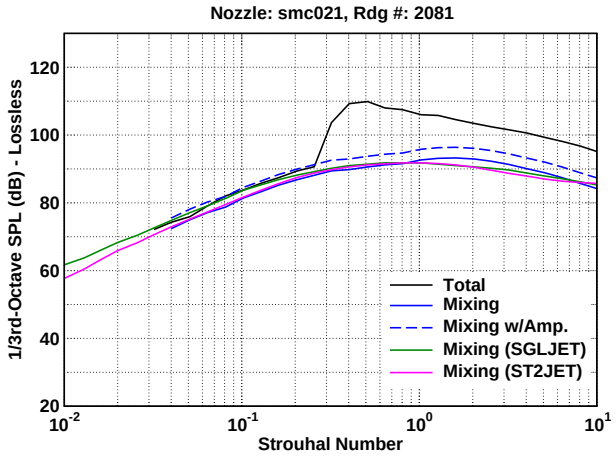

(c) $M_j = 1.392, \text{NPR} = 3.147, T_t/T_\infty = 1.01$

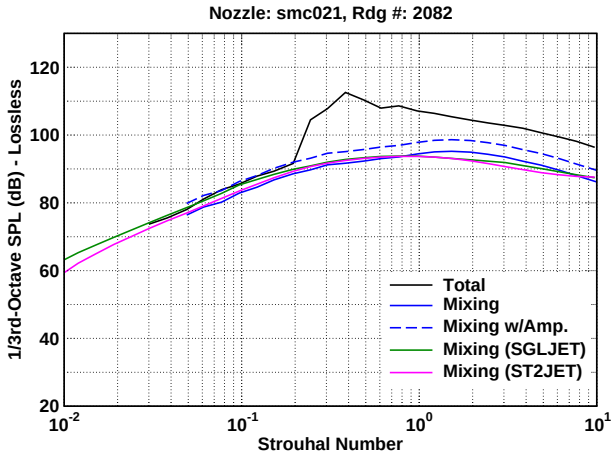

(d) $M_j = 1.493, \text{NPR} = 3.636, T_t/T_\infty = 1.01$

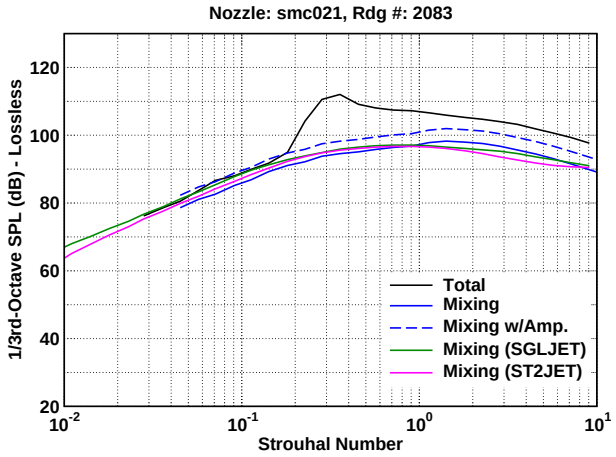

(e) $M_j = 1.660, \text{NPR} = 4.647, T_t/T_\infty = 1.01$

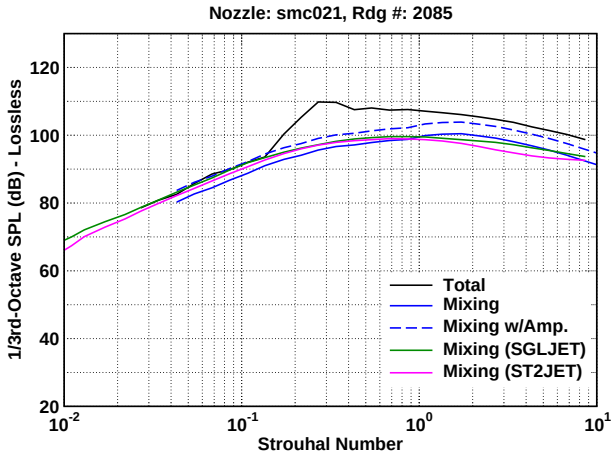

(f) $M_j = 1.796, \text{NPR} = 5.708, T_t/T_\infty = 1.01$

Figure 6: 1/3-Octave spectra comparisons of jet mixing noise prediction models to the mixing noise component spectra for measured data from jets with shocks at a 50 degree inlet angle and distance $100D$.

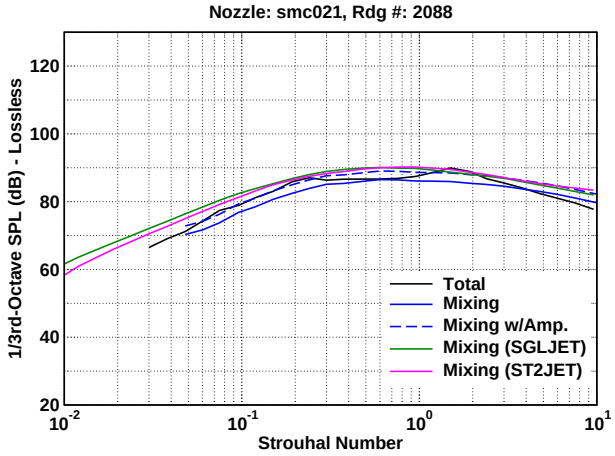

(g) $M_j = 1.050, \text{NPR} = 2.004, T_t/T_\infty = 1.77$

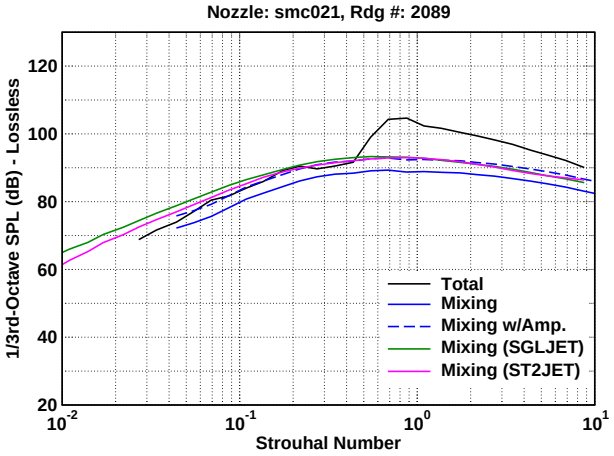

(h) $M_j = 1.182, \text{NPR} = 2.365, T_t/T_\infty = 1.77$

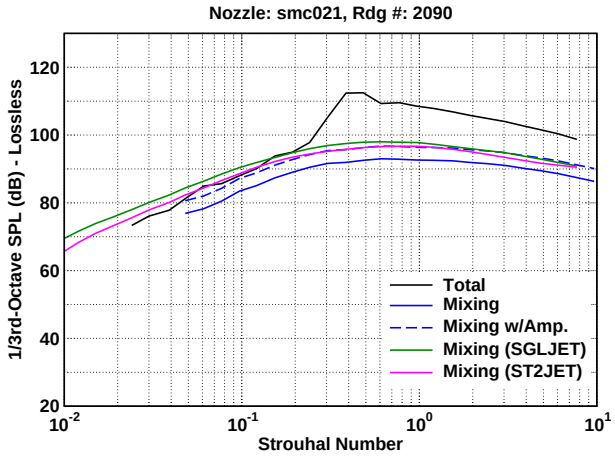

(i) $M_j = 1.392, \text{NPR} = 3.143, T_t/T_\infty = 1.76$

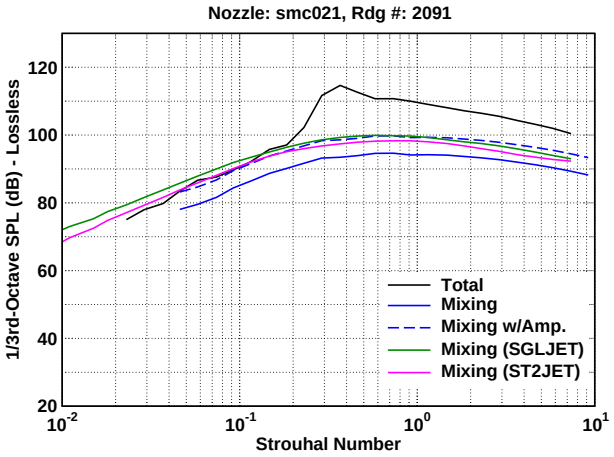

(j) $M_j = 1.492, \text{NPR} = 3.627, T_t/T_\infty = 1.76$

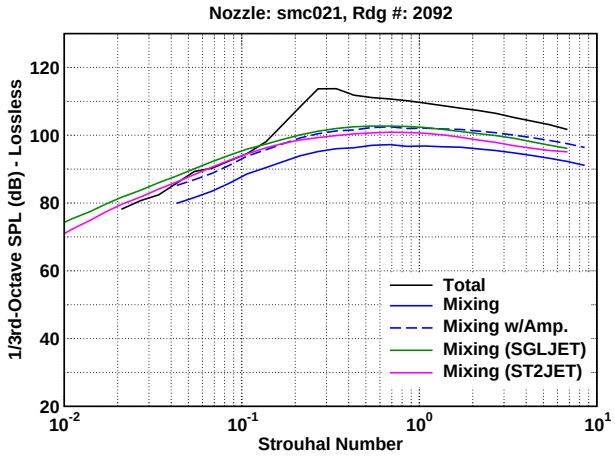

(k) $M_j = 1.660, \text{NPR} = 4.644, T_t/T_\infty = 1.77$

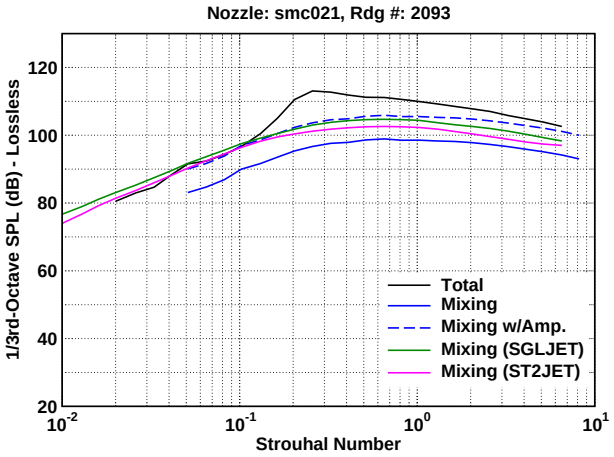

(l) $M_j = 1.792, \text{NPR} = 5.674, T_t/T_\infty = 1.76$

Figure 6: (50 Deg., Cont.)

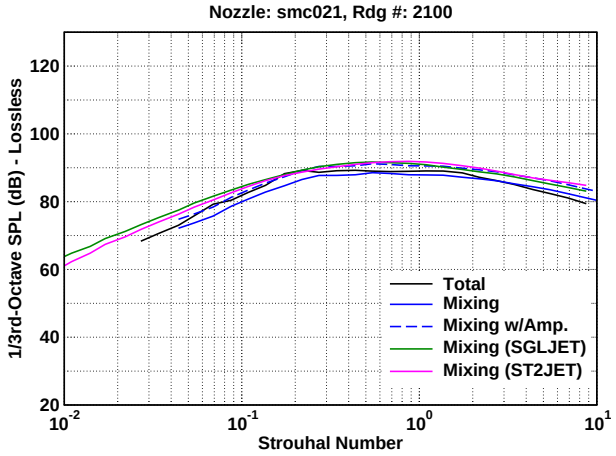

(m) $M_j = 1.045, \text{NPR} = 1.989, T_t/T_\infty = 2.16$

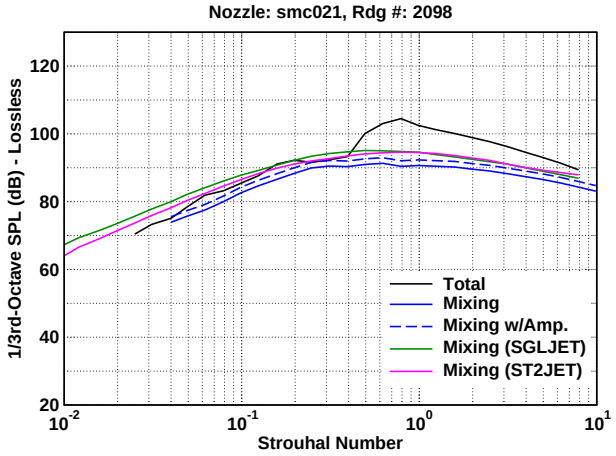

(n) $M_j = 1.181, \text{NPR} = 2.356, T_t/T_\infty = 2.16$

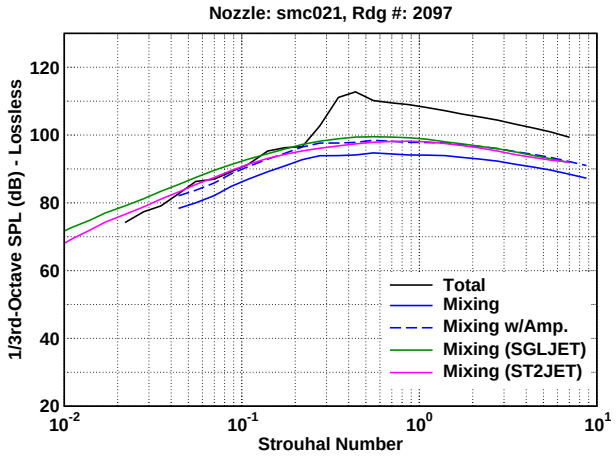

(o) $M_j = 1.390, \text{NPR} = 3.130, T_t/T_\infty = 2.16$

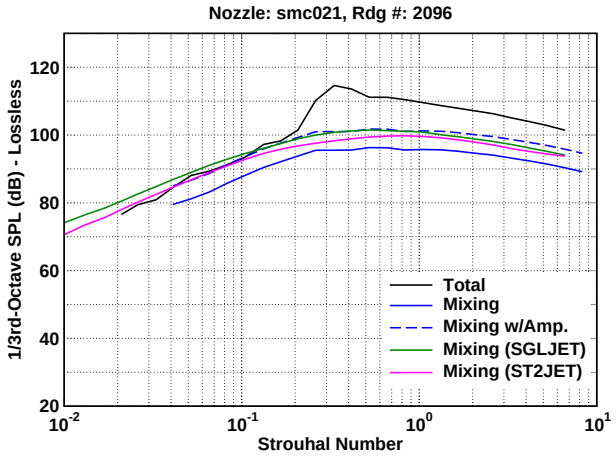

(p) $M_j = 1.494, \text{NPR} = 3.629, T_t/T_\infty = 2.16$

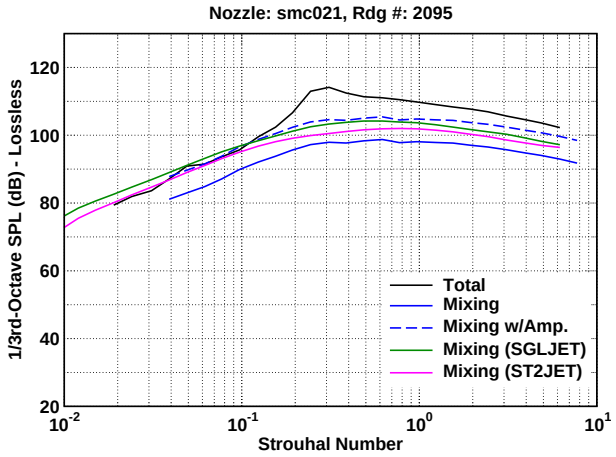

(q) $M_j = 1.660, \text{NPR} = 4.638, T_t/T_\infty = 2.16$

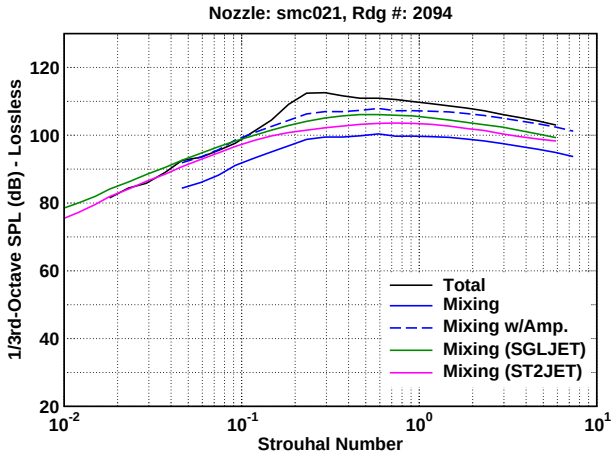

(r) $M_j = 1.794, \text{NPR} = 5.685, T_t/T_\infty = 2.16$

Figure 6: (50 Deg., Cont.)

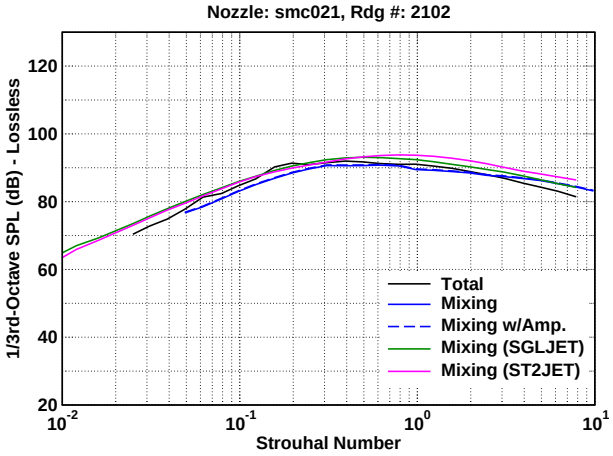

(s) $M_j = 1.048, \text{NPR} = 1.987, T_t/T_\infty = 2.66$

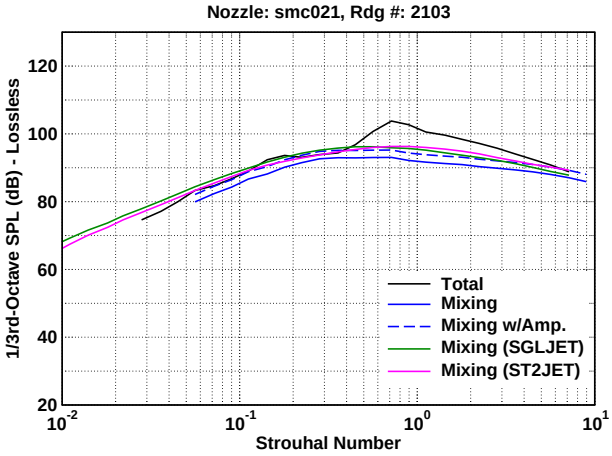

(t) $M_j = 1.175, \text{NPR} = 2.327, T_t/T_\infty = 2.65$

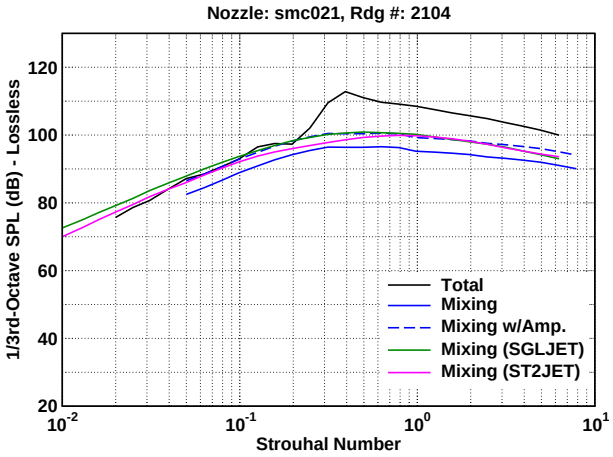

(u) $M_j = 1.391, \text{NPR} = 3.120, T_t/T_\infty = 2.66$

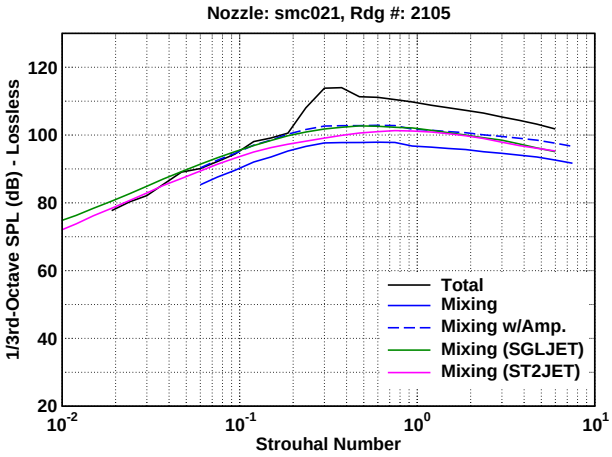

(v) $M_j = 1.490, \text{NPR} = 3.597, T_t/T_\infty = 2.65$

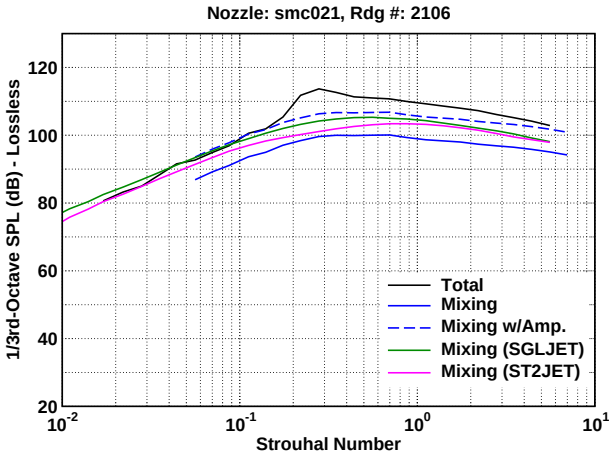

(w) $M_j = 1.660, \text{NPR} = 4.630, T_t/T_\infty = 2.64$

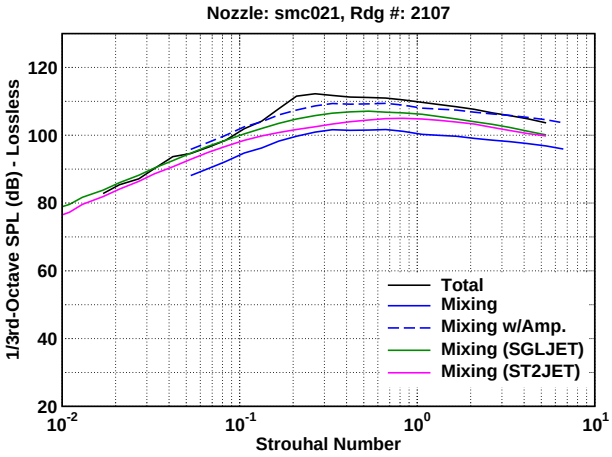

(x) $M_j = 1.789, \text{NPR} = 5.638, T_t/T_\infty = 2.65$

Figure 6: (50 Deg., Cont.)

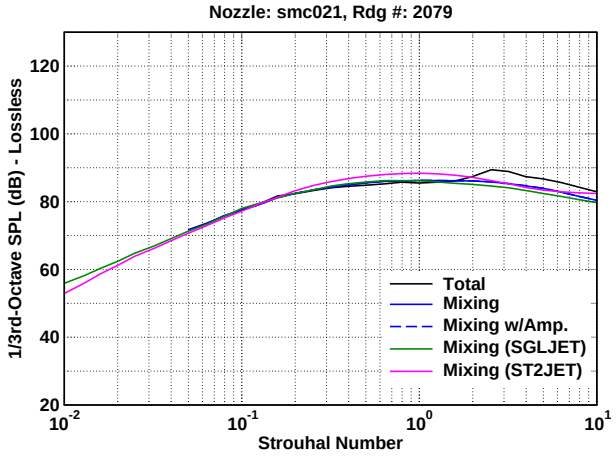

(a) $M_j = 1.049, \text{NPR} = 2.005, T_t/T_\infty = 1.01$

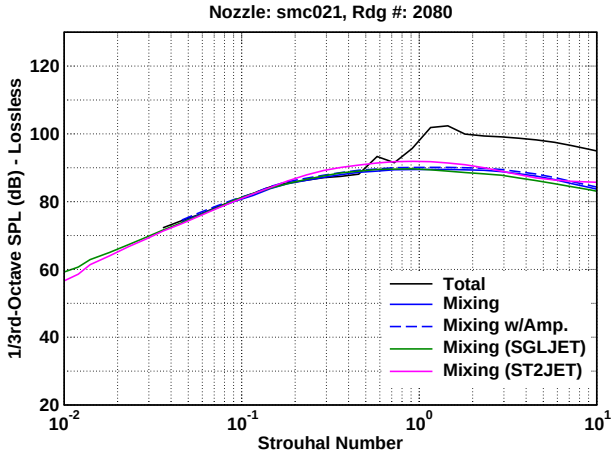

(b) $M_j = 1.178, \text{NPR} = 2.358, T_t/T_\infty = 1.01$

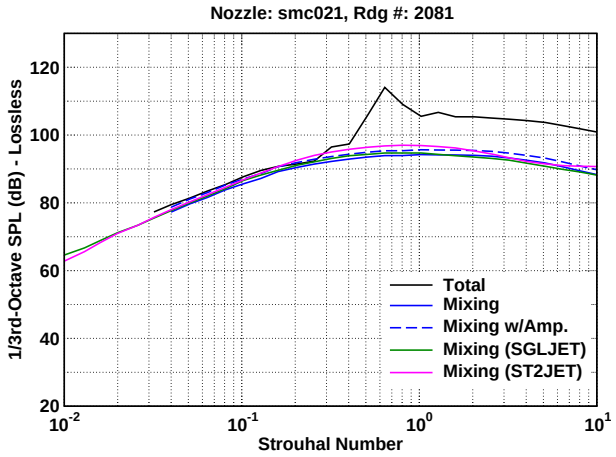

(c) $M_j = 1.392, \text{NPR} = 3.147, T_t/T_\infty = 1.01$

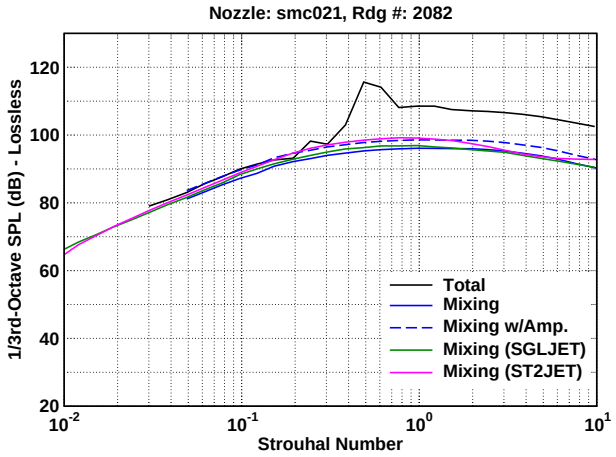

(d) $M_j = 1.493, \text{NPR} = 3.636, T_t/T_\infty = 1.01$

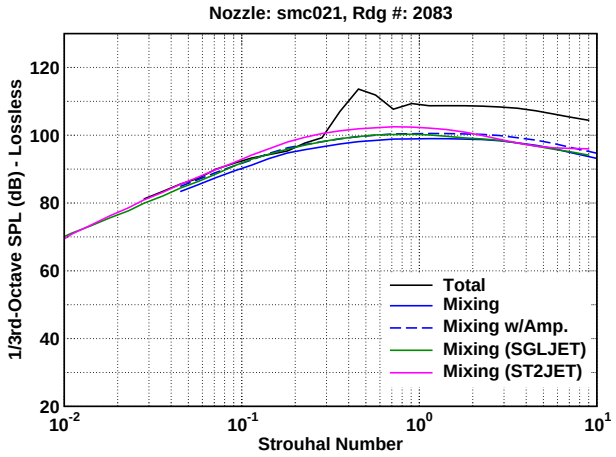

(e) $M_j = 1.660, \text{NPR} = 4.647, T_t/T_\infty = 1.01$

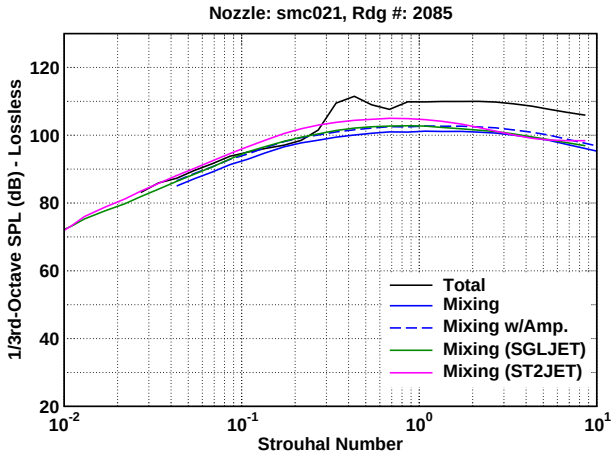

(f) $M_j = 1.796, \text{NPR} = 5.708, T_t/T_\infty = 1.01$

Figure 7: 1/3-Octave spectra comparisons of jet mixing noise prediction models to the mixing noise component spectra for measured data from jets with shocks at a 90 degree inlet angle and distance $100D$.

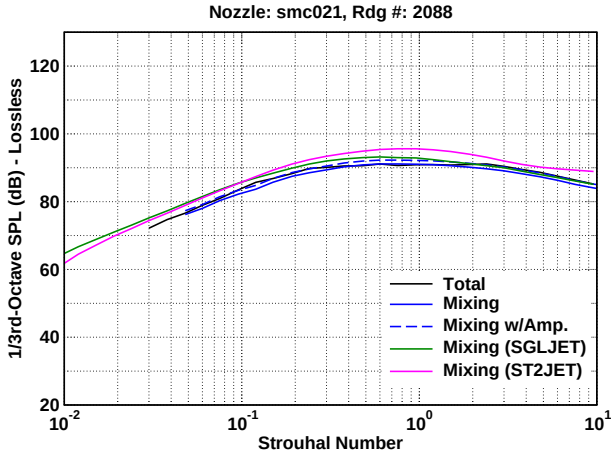

(g) $M_j = 1.049, \mathrm{NPR} = 2.004, T_t/T_\infty = 1.77$

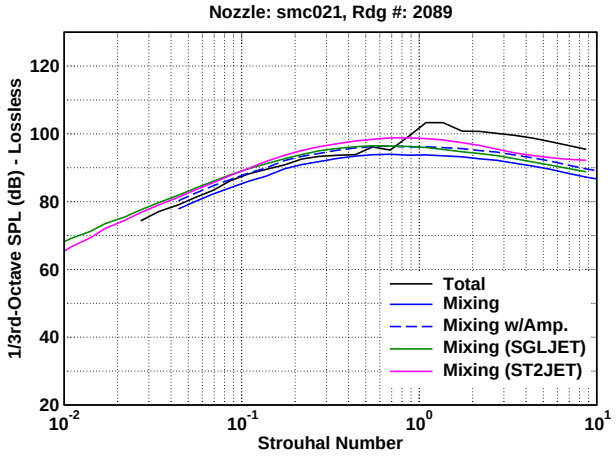

(h) $M_j = 1.182, \mathrm{NPR} = 2.365, T_t/T_\infty = 1.77$

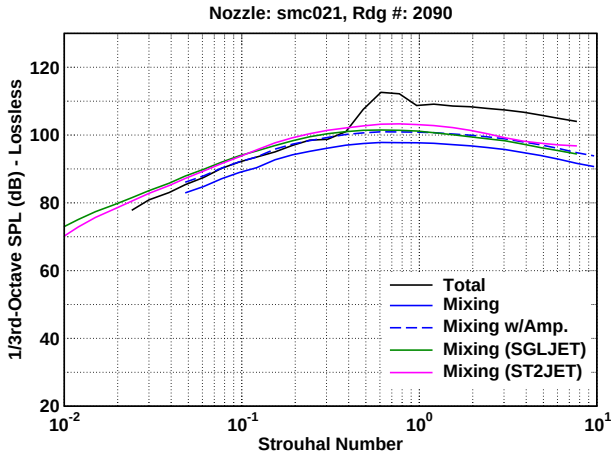

(i) $M_j = 1.392, \mathrm{NPR} = 3.143, T_t/T_\infty = 1.76$

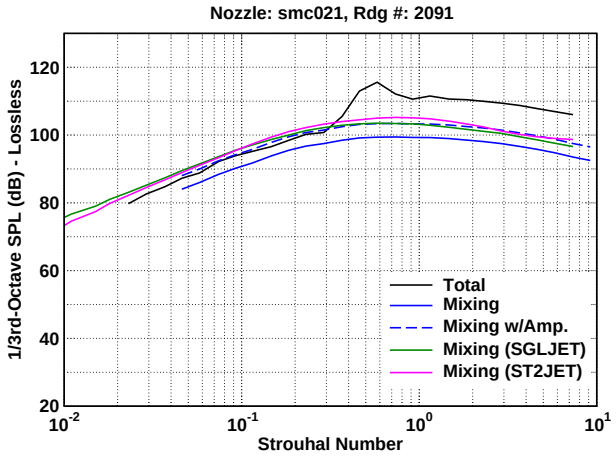

(j) $M_j = 1.492, \mathrm{NPR} = 3.627, T_t/T_\infty = 1.76$

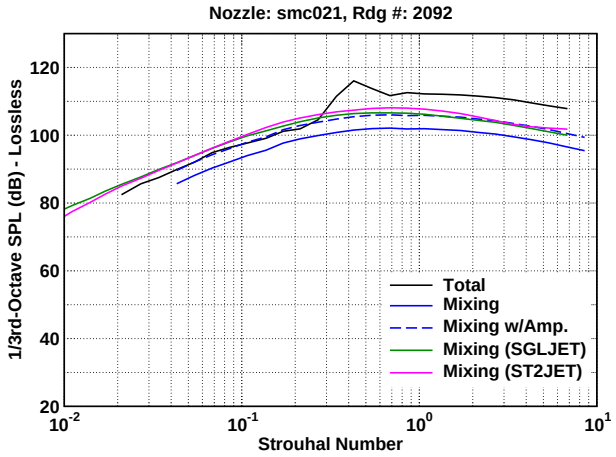

(k) $M_j = 1.660, \mathrm{NPR} = 4.644, T_t/T_\infty = 1.77$

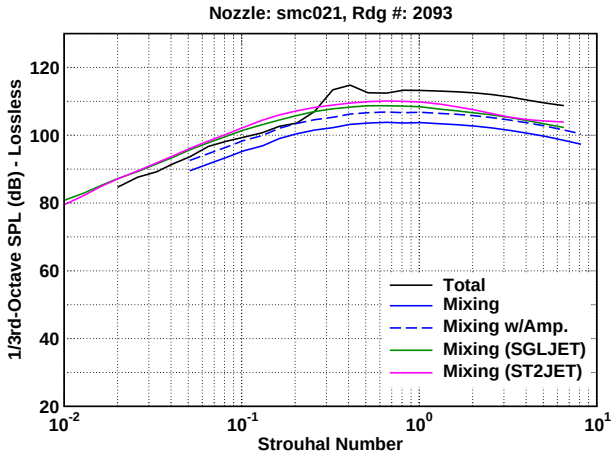

(l) $M_j = 1.792, \mathrm{NPR} = 5.674, T_t/T_\infty = 1.76$

Figure 7: (90 Deg., Cont.)

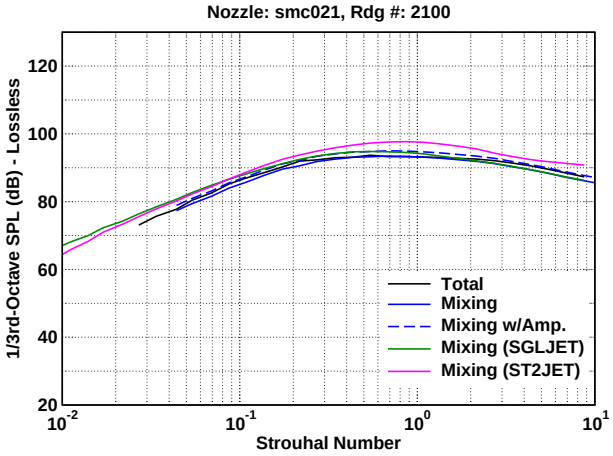

(m) $M_j = 1.045, \text{NPR} = 1.989, T_t/T_\infty = 2.16$

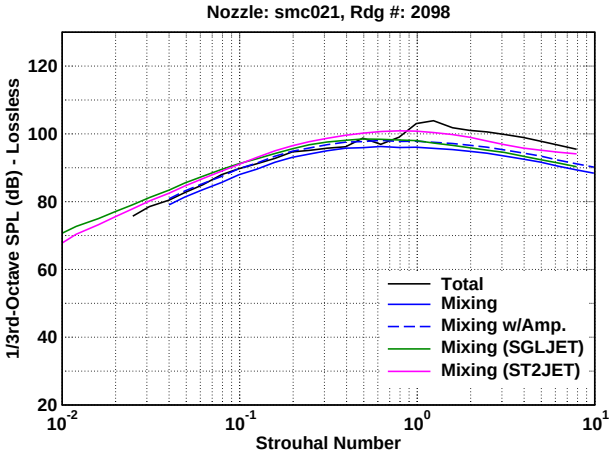

(n) $M_j = 1.181, \text{NPR} = 2.356, T_t/T_\infty = 2.16$

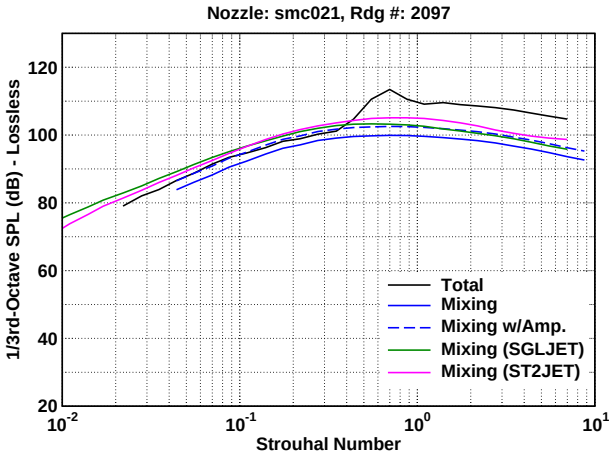

(o) $M_j = 1.390, \text{NPR} = 3.130, T_t/T_\infty = 2.16$

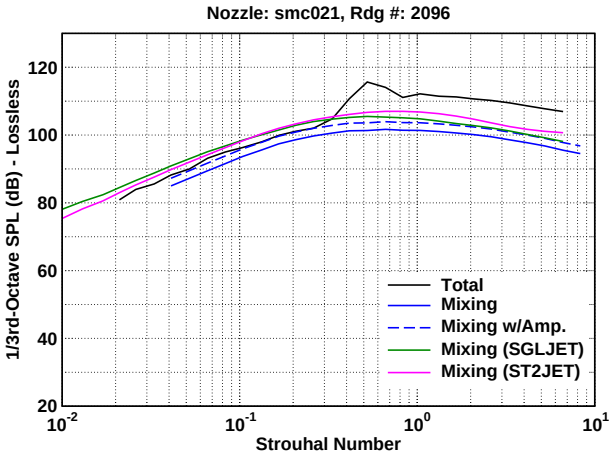

(p) $M_j = 1.494, \text{NPR} = 3.629, T_t/T_\infty = 2.16$

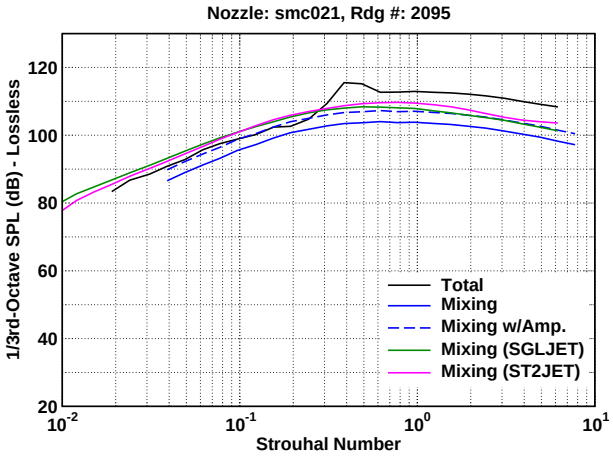

(q) $M_j = 1.660, \text{NPR} = 4.638, T_t/T_\infty = 2.16$

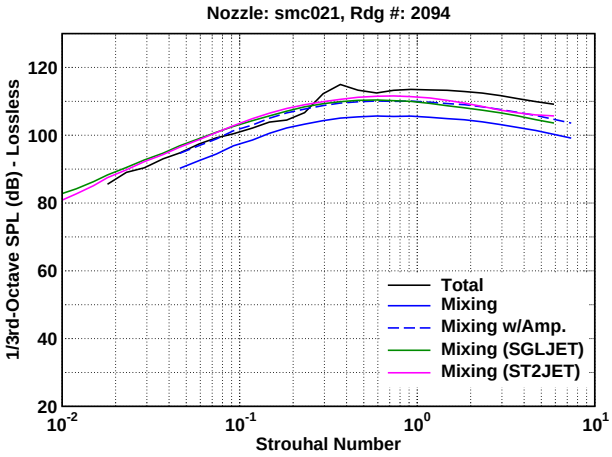

(r) $M_j = 1.794, \text{NPR} = 5.685, T_t/T_\infty = 2.16$

Figure 7: (90 Deg., Cont.)

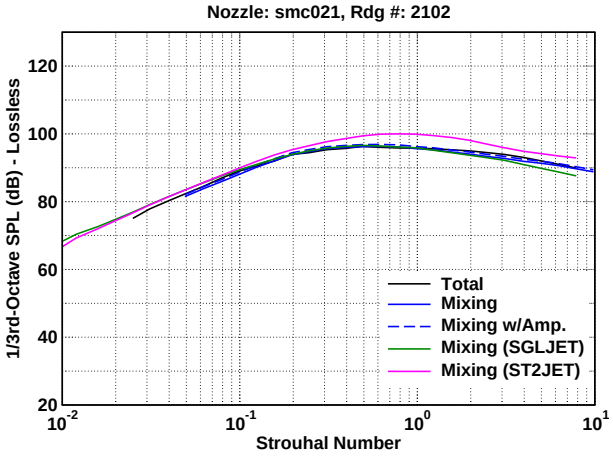

(s) $M_j = 1.048, \text{NPR} = 1.987, T_t/T_\infty = 2.66$

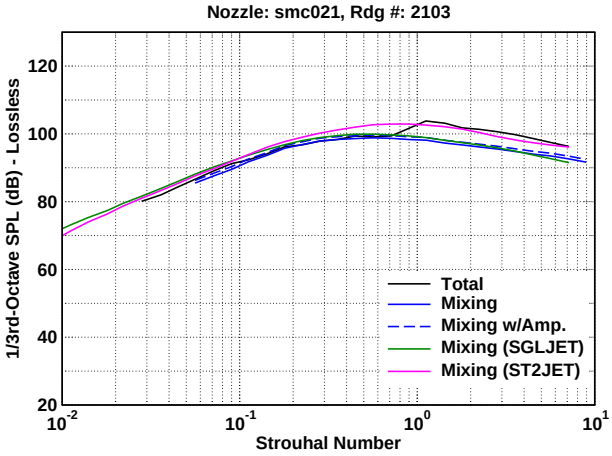

(t) $M_j = 1.175, \text{NPR} = 2.327, T_t/T_\infty = 2.65$

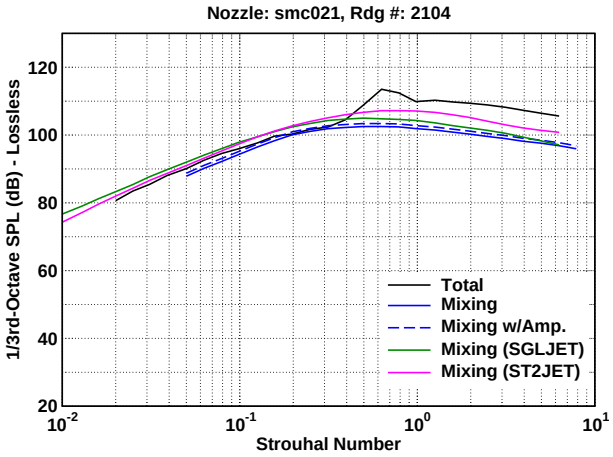

(u) $M_j = 1.391, \text{NPR} = 3.120, T_t/T_\infty = 2.66$

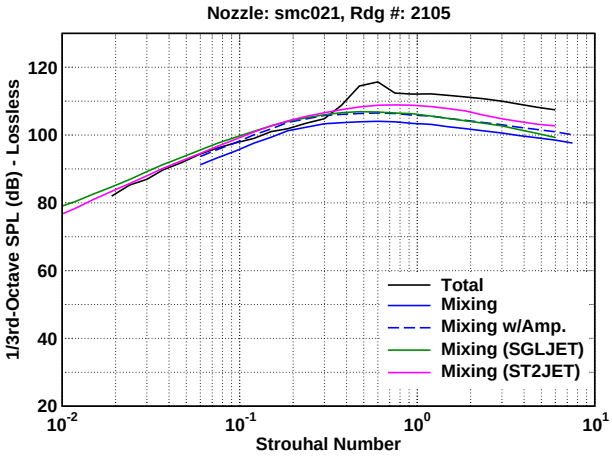

(v) $M_j = 1.490, \text{NPR} = 3.597, T_t/T_\infty = 2.65$

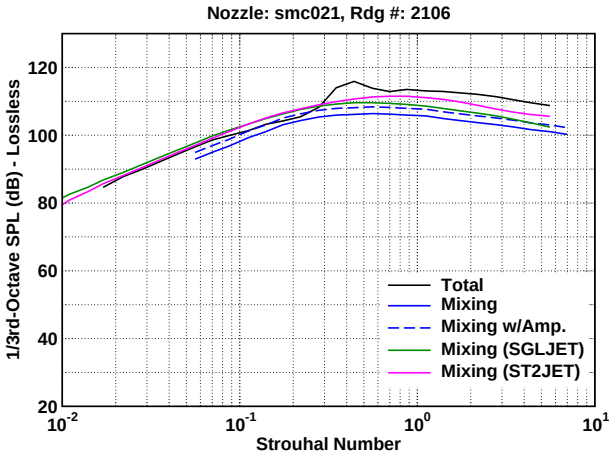

(w) $M_j = 1.660, \text{NPR} = 4.630, T_t/T_\infty = 2.64$

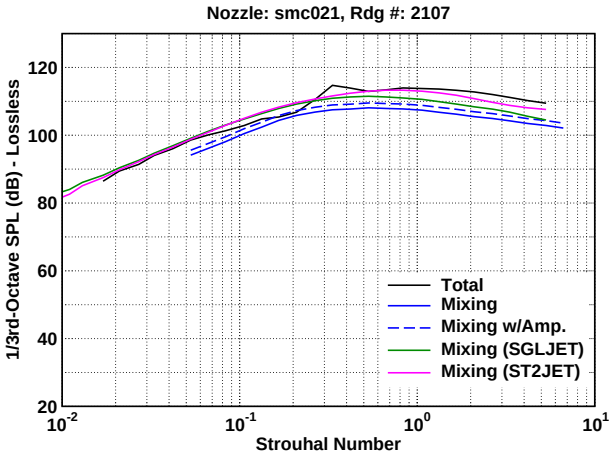

(x) $M_j = 1.789, \text{NPR} = 5.638, T_t/T_\infty = 2.65$

Figure 7: (90 Deg., Cont.)

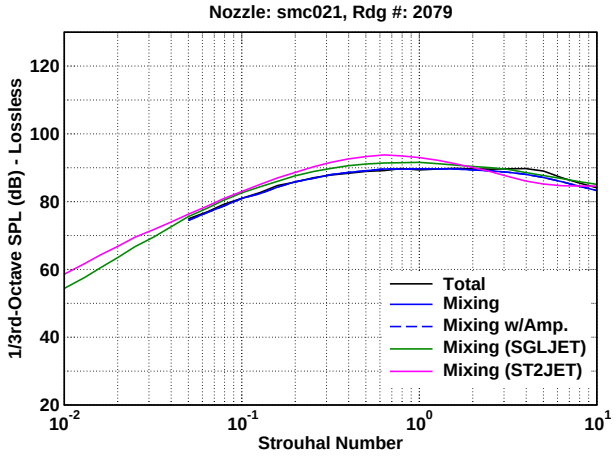

(a) $M_j = 1.049, \text{NPR} = 2.005, T_t/T_\infty = 1.01$

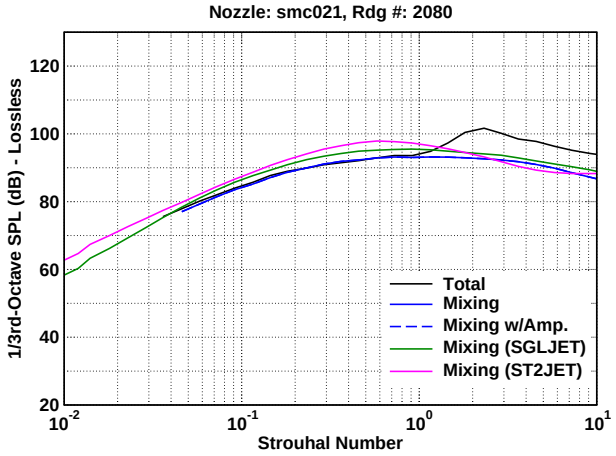

(b) $M_j = 1.178, \text{NPR} = 2.358, T_t/T_\infty = 1.01$

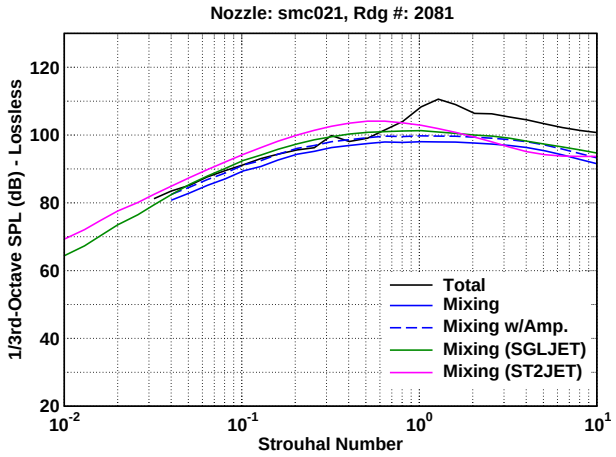

(c) $M_j = 1.392, \text{NPR} = 3.147, T_t/T_\infty = 1.01$

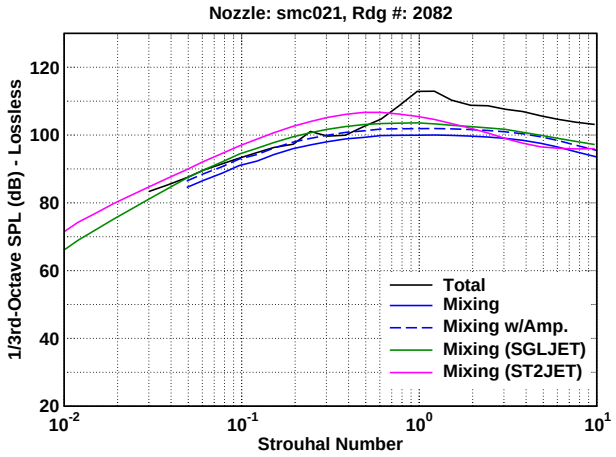

(d) $M_j = 1.493, \text{NPR} = 3.636, T_t/T_\infty = 1.01$

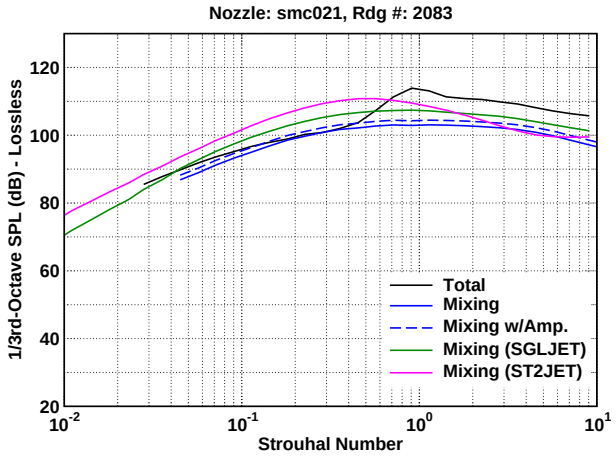

(e) $M_j = 1.660, \text{NPR} = 4.647, T_t/T_\infty = 1.01$

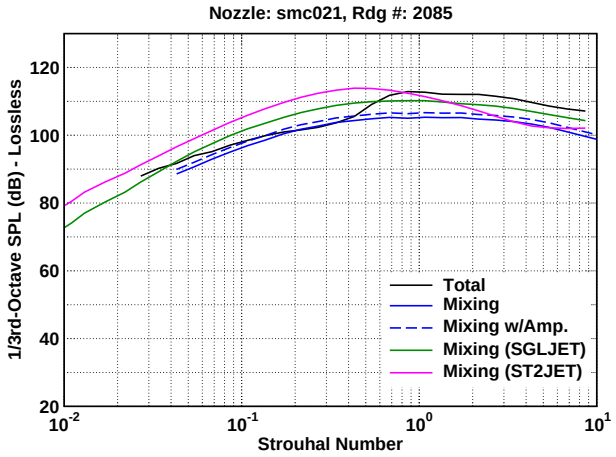

(f) $M_j = 1.796, \text{NPR} = 5.708, T_t/T_\infty = 1.01$

Figure 8: 1/3-Octave spectra comparisons of jet mixing noise prediction models to the mixing noise component spectra for measured data from jets with shocks at a 120 degree inlet angle and distance $100D$.

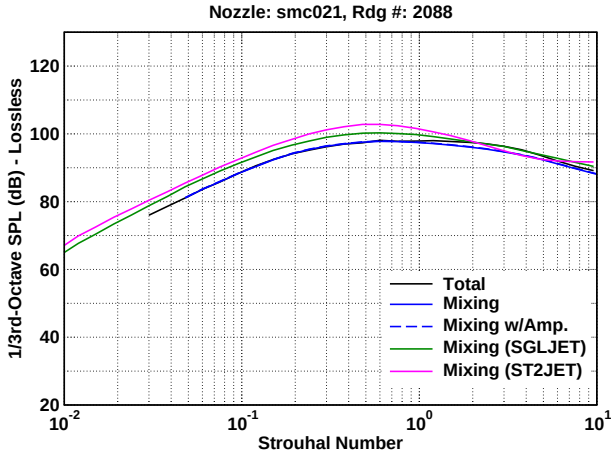

(g) $M_j = 1.049, \text{NPR} = 2.004, T_t/T_\infty = 1.77$

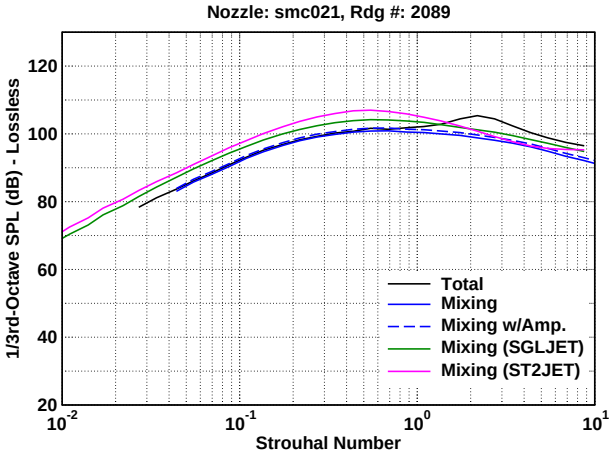

(h) $M_j = 1.182, \text{NPR} = 2.365, T_t/T_\infty = 1.77$

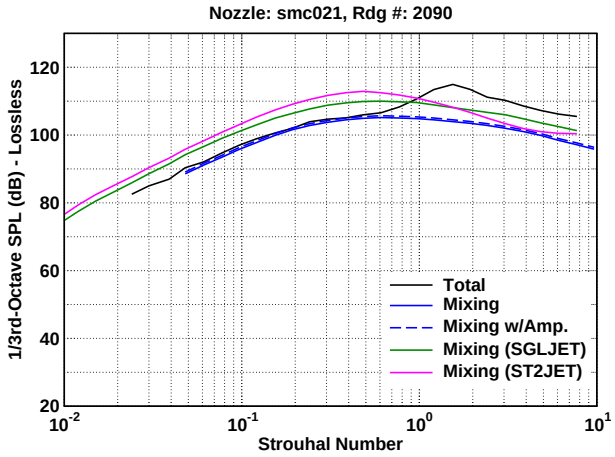

(i) $M_j = 1.392, \text{NPR} = 3.143, T_t/T_\infty = 1.76$

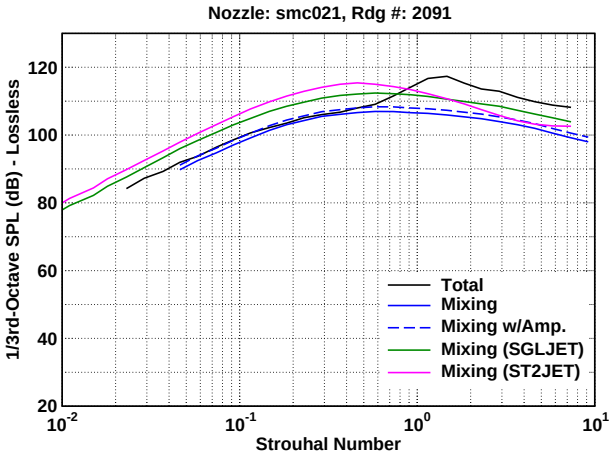

(j) $M_j = 1.492, \text{NPR} = 3.627, T_t/T_\infty = 1.76$

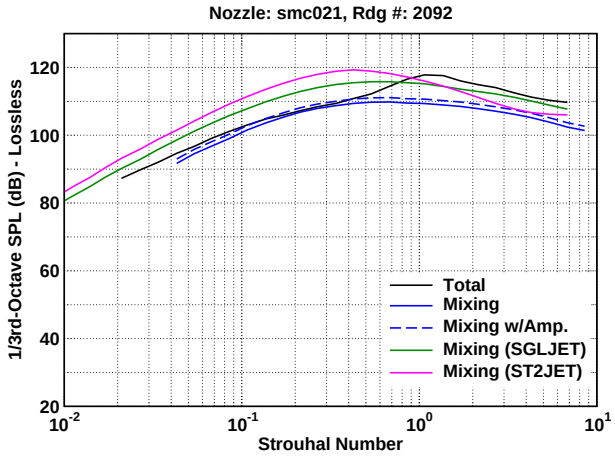

(k) $M_j = 1.660, \text{NPR} = 4.644, T_t/T_\infty = 1.77$

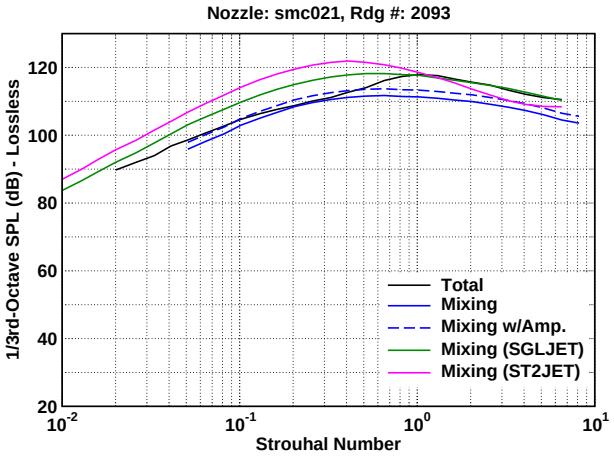

(l) $M_j = 1.792, \text{NPR} = 5.674, T_t/T_\infty = 1.76$

Figure 8: (120 Deg., Cont.)

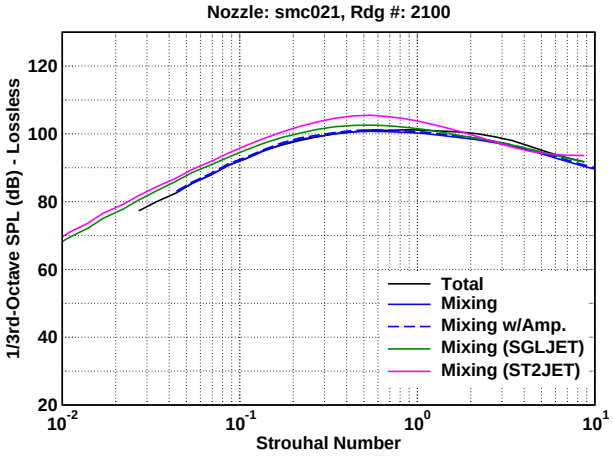

(m) $M_j = 1.045, \text{NPR} = 1.989, T_t/T_\infty = 2.16$

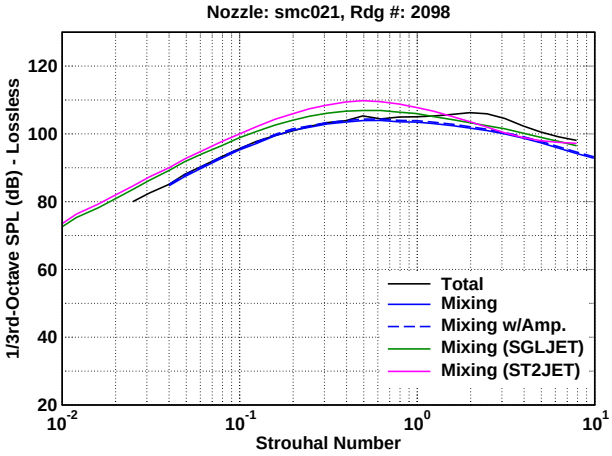

(n) $M_j = 1.181, \text{NPR} = 2.356, T_t/T_\infty = 2.16$

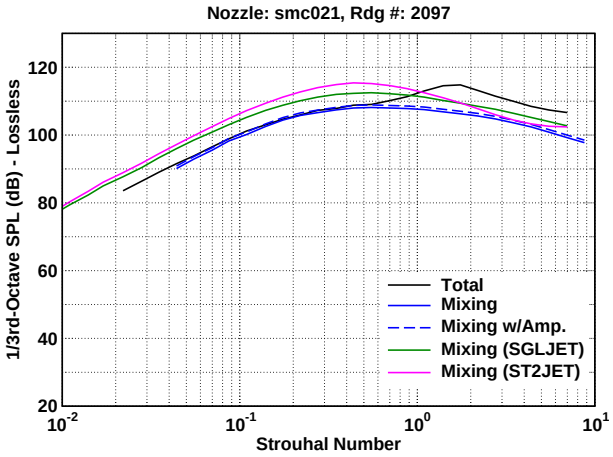

(o) $M_j = 1.390, \text{NPR} = 3.130, T_t/T_\infty = 2.16$

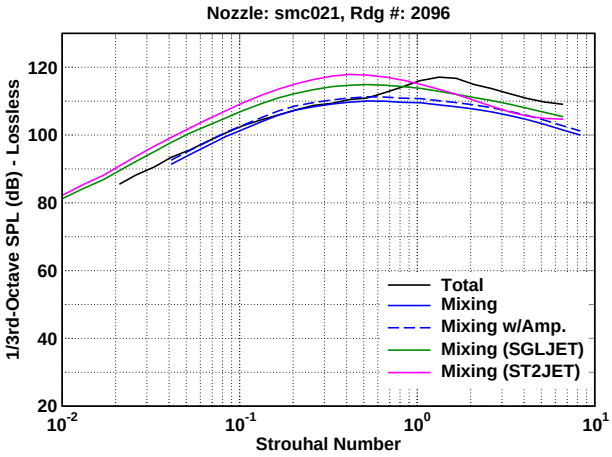

(p) $M_j = 1.494, \text{NPR} = 3.629, T_t/T_\infty = 2.16$

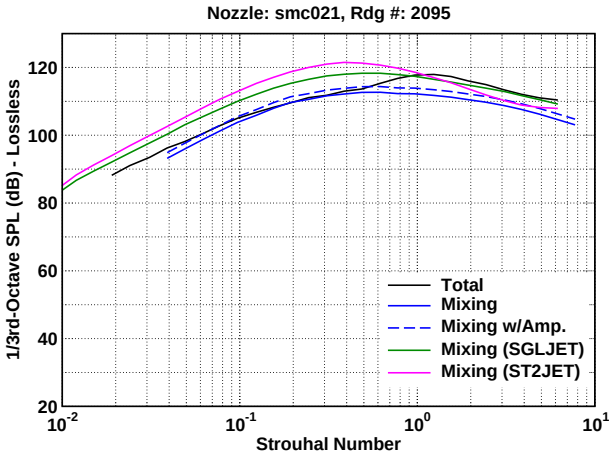

(q) $M_j = 1.660, \text{NPR} = 4.638, T_t/T_\infty = 2.16$

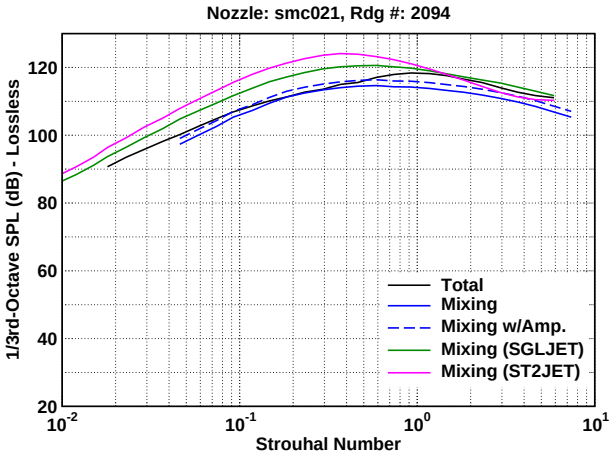

(r) $M_j = 1.794, \text{NPR} = 5.685, T_t/T_\infty = 2.16$

Figure 8: (120 Deg., Cont.)

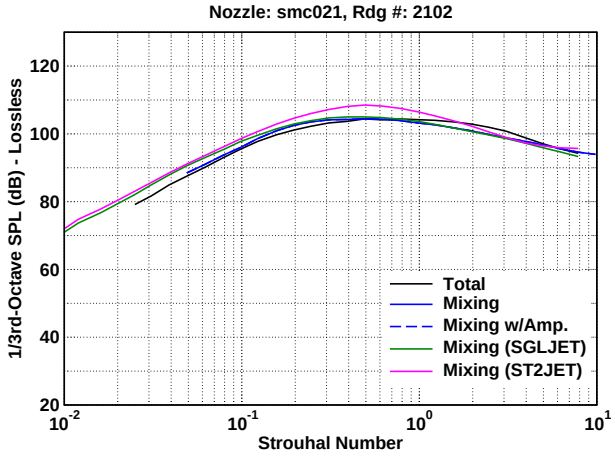

(s) $M_j = 1.048, \text{NPR} = 1.987, T_t/T_\infty = 2.66$

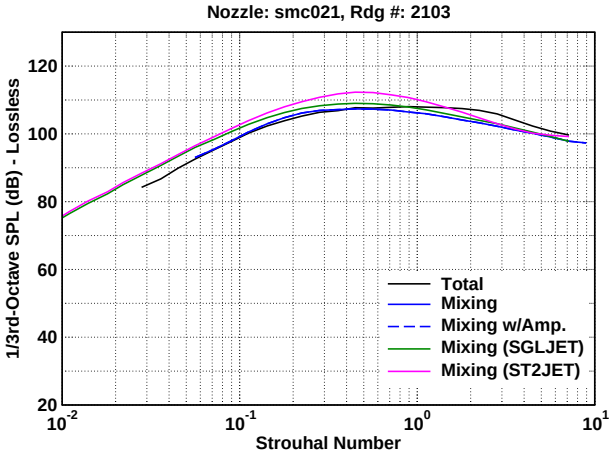

(t) $M_j = 1.175, \text{NPR} = 2.327, T_t/T_\infty = 2.65$

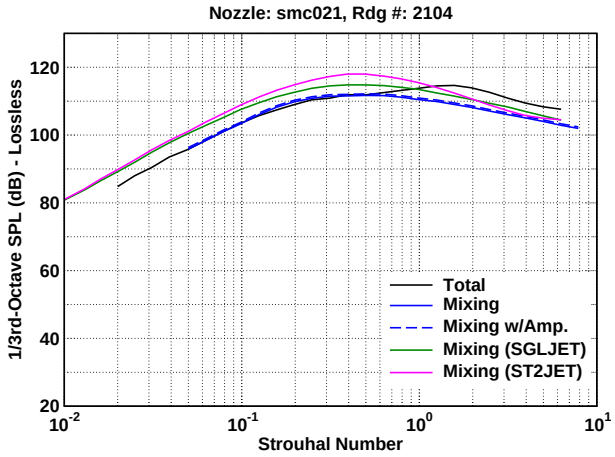

(u) $M_j = 1.391, \text{NPR} = 3.120, T_t/T_\infty = 2.66$

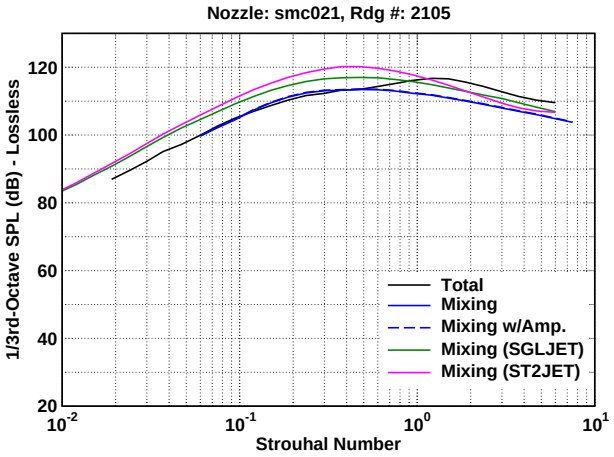

(v) $M_j = 1.490, \text{NPR} = 3.597, T_t/T_\infty = 2.65$

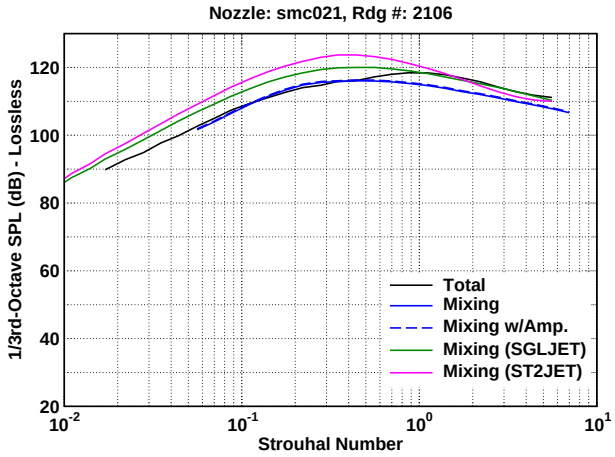

(w) $M_j = 1.660, \text{NPR} = 4.630, T_t/T_\infty = 2.64$

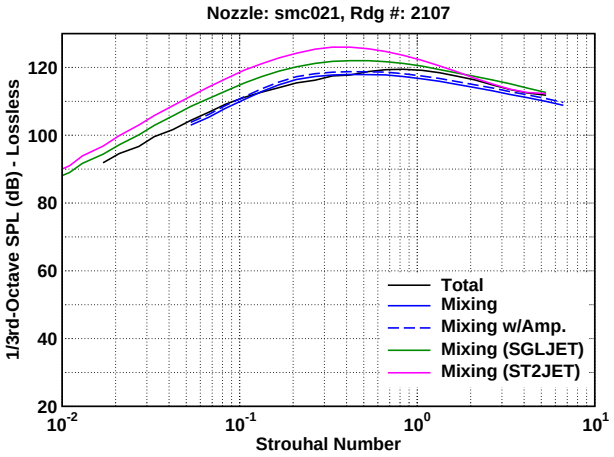

(x) $M_j = 1.789, \text{NPR} = 5.638, T_t/T_\infty = 2.65$

Figure 8: (120 Deg., Cont.)

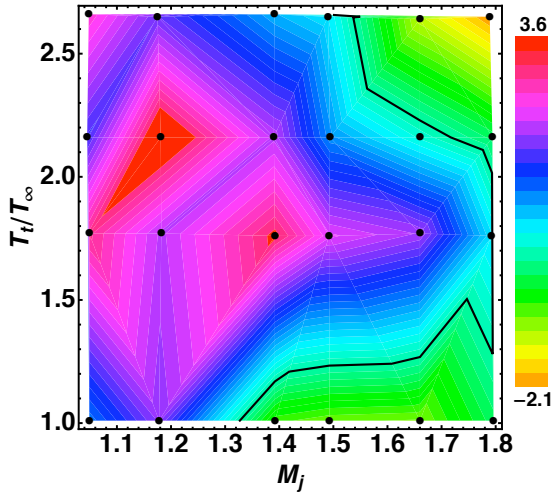

(a) SGLJET Module, 50 degrees.

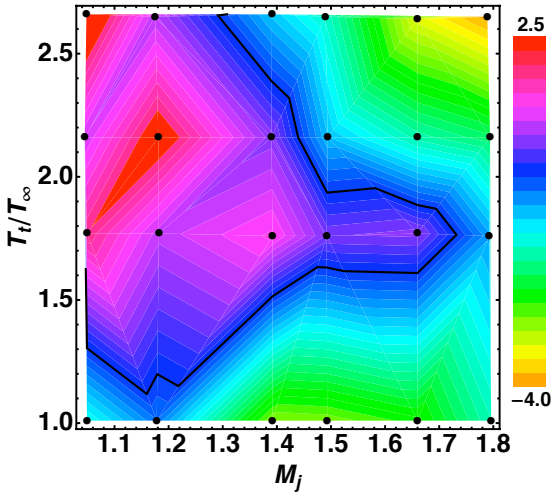

(d) ST2JET Module, 50 degrees.

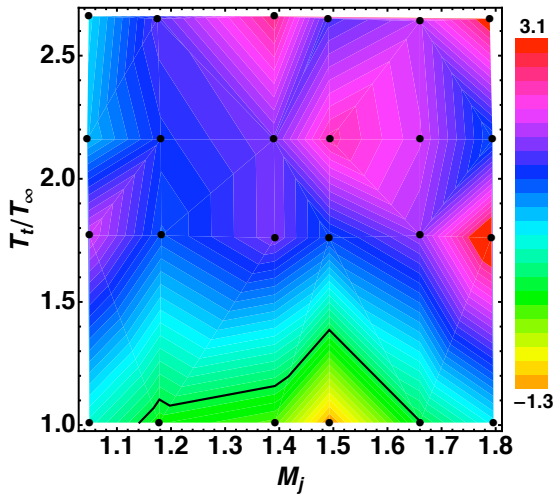

(b) SGLJET Module, 90 degrees.

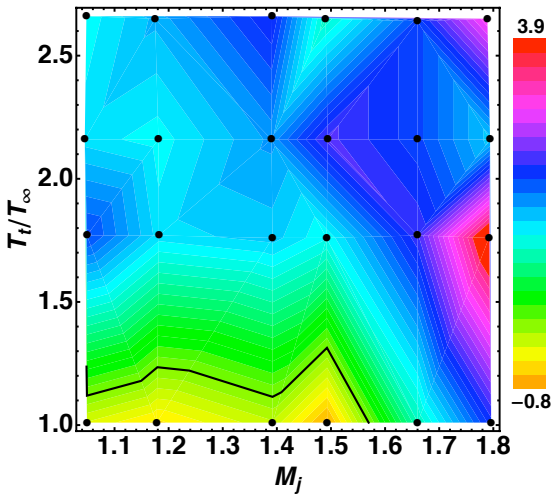

(e) ST2JET Module, 90 degrees.

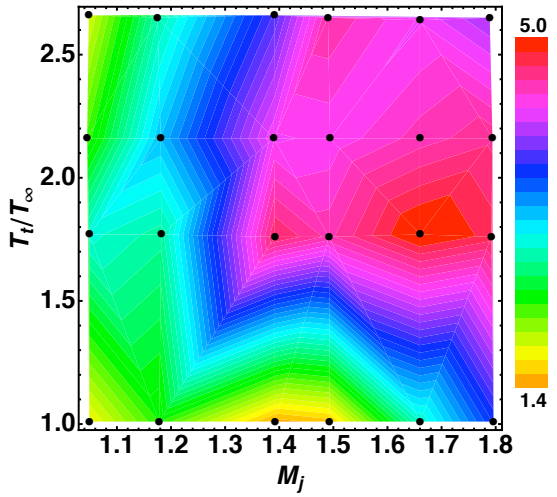

(c) SGLJET Module, 120 degrees.

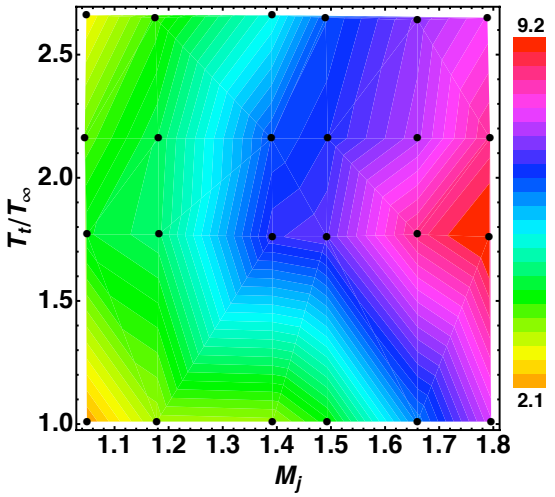

(f) ST2JET Module, 120 degrees.

Figure 9: Error in mixing noise level (dB(predicted) - dB(measured)) with amplification at the 1/3-octave band nearest the Strouhal number 0.1. Black line = 0 dB. Data located at positions of black dots.

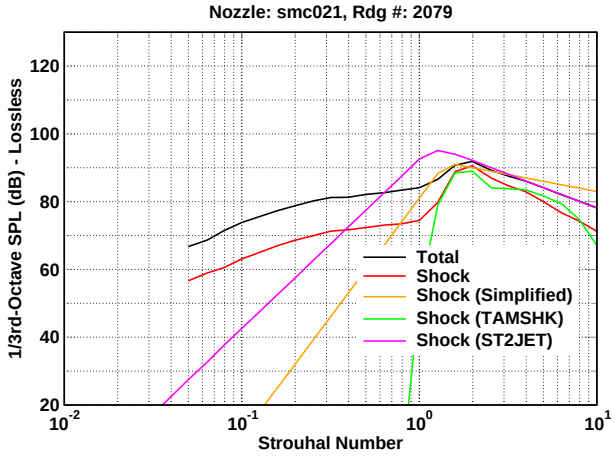

(a) $M_j = 1.049, \text{NPR} = 2.005, T_t/T_\infty = 1.01, \beta = 0.315$

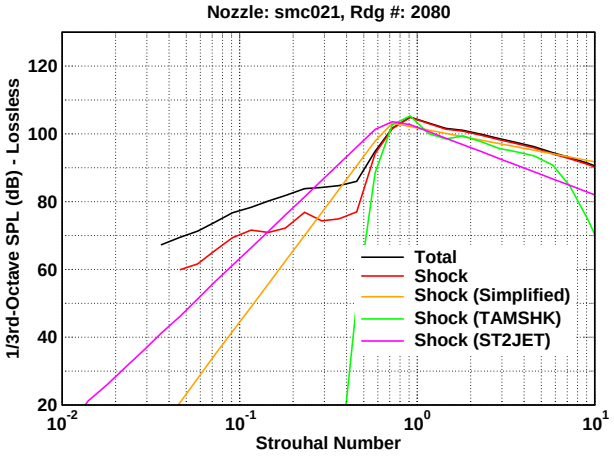

(b) $M_j = 1.178, \text{NPR} = 2.358, T_t/T_\infty = 1.01, \beta = 0.623$

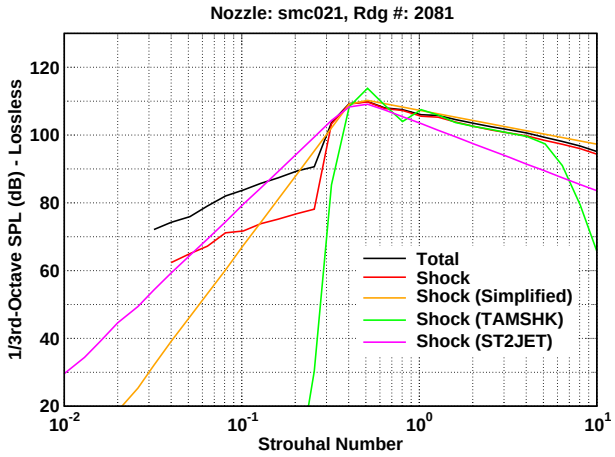

(c) $M_j = 1.392, \text{NPR} = 3.147, T_t/T_\infty = 1.01, \beta = 0.969$

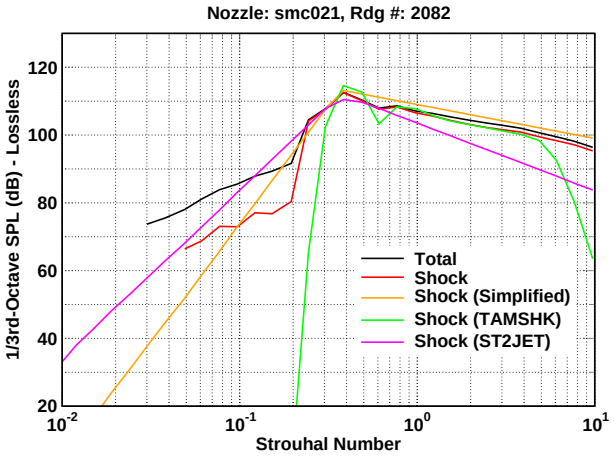

(d) $M_j = 1.493, \text{NPR} = 3.636, T_t/T_\infty = 1.01, \beta = 1.109$

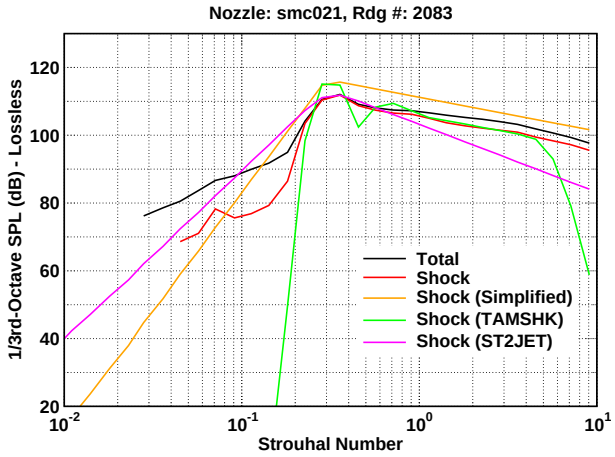

(e) $M_j = 1.660, \text{NPR} = 4.647, T_t/T_\infty = 1.01, \beta = 1.325$

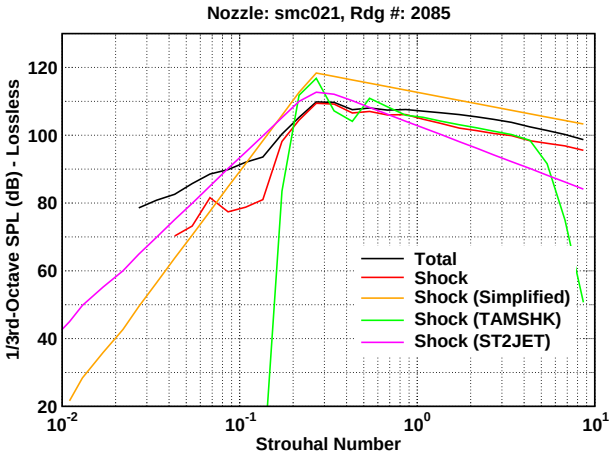

(f) $M_j = 1.796, \text{NPR} = 5.708, T_t/T_\infty = 1.01, \beta = 1.491$

Figure 10: 1/3-Octave spectra comparisons of jet shock-associated noise prediction models to the shock-associated noise component spectra for measured data from jets with shocks at a 50 degree inlet angle and distance $100D$.

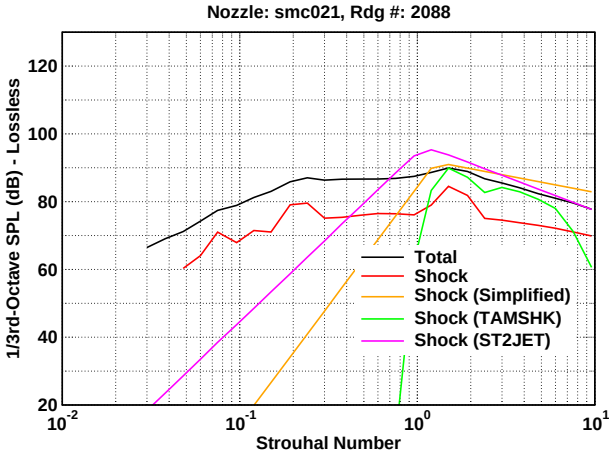

(g) $M_j = 1.050, \text{NPR} = 2.004, T_t/T_\infty = 1.77, \beta = 0.319$

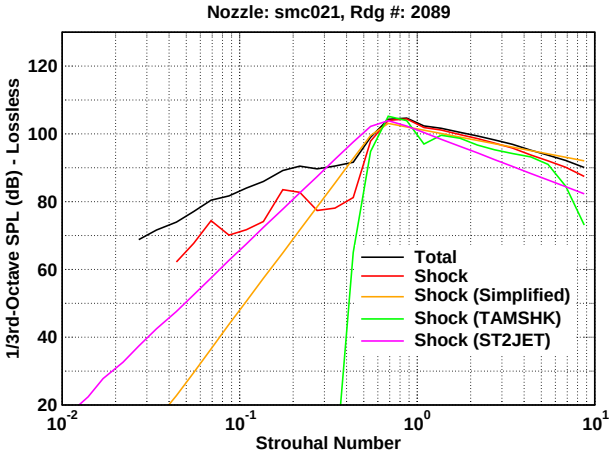

(h) $M_j = 1.182, \text{NPR} = 2.365, T_t/T_\infty = 1.77, \beta = 0.630$

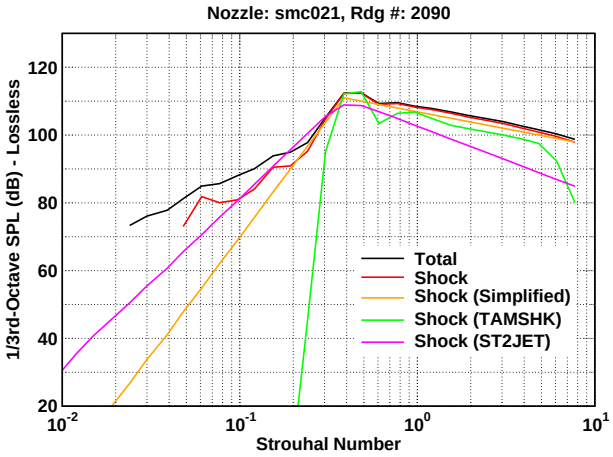

(i) $M_j = 1.392, \text{NPR} = 3.143, T_t/T_\infty = 1.76, \beta = 0.968$

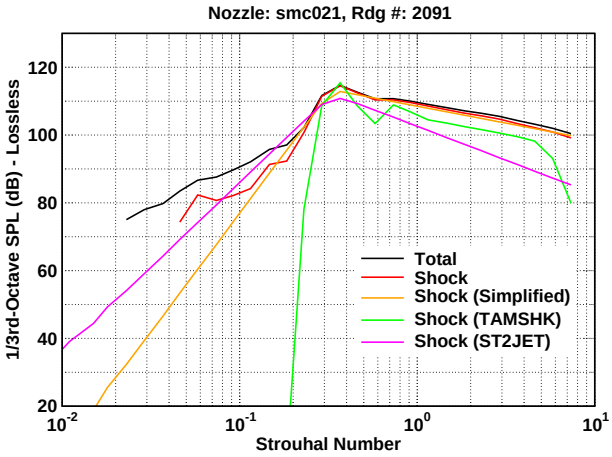

(j) $M_j = 1.492, \text{NPR} = 3.627, T_t/T_\infty = 1.76, \beta = 1.108$

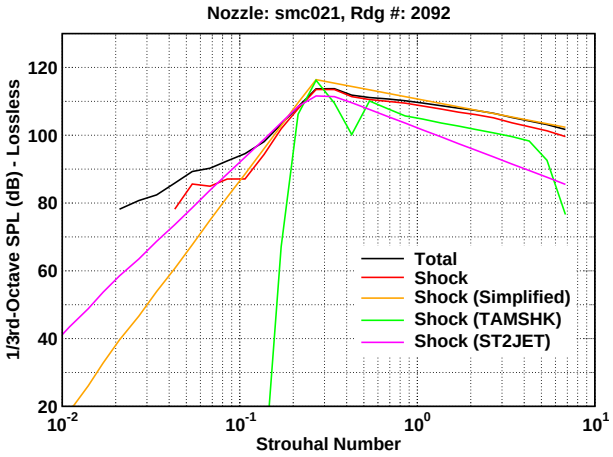

(k) $M_j = 1.660, \text{NPR} = 4.644, T_t/T_\infty = 1.77, \beta = 1.325$

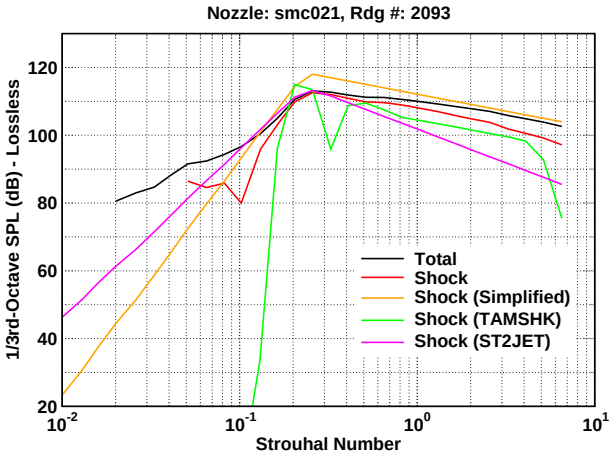

(l) $M_j = 1.792, \text{NPR} = 5.674, T_t/T_\infty = 1.76, \beta = 1.487$

Figure 10: (50 Deg., Cont.)

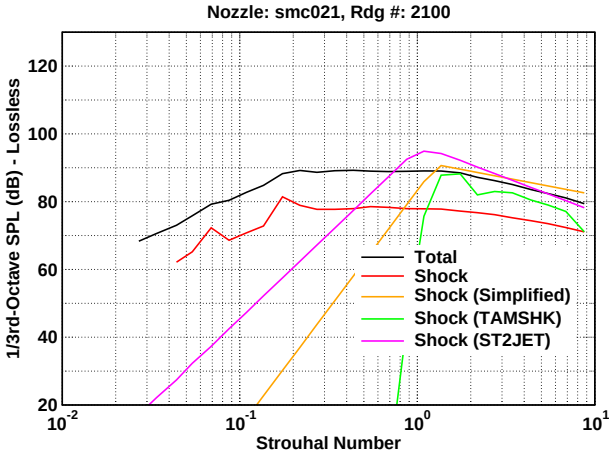

(m) $M_j = 1.045, \text{NPR} = 1.989, T_t/T_\infty = 2.16, \beta = 0.305$

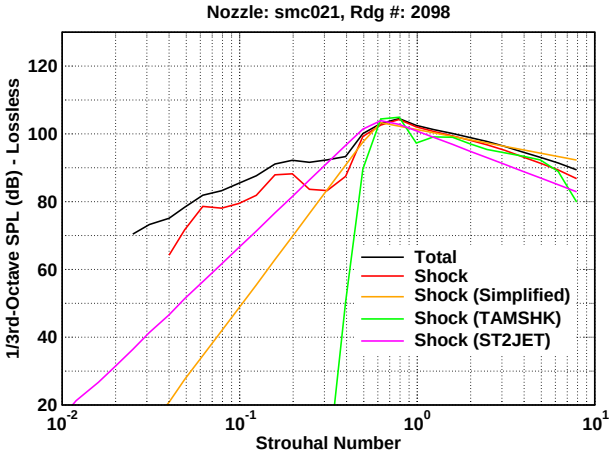

(n) $M_j = 1.181, \text{NPR} = 2.356, T_t/T_\infty = 2.16, \beta = 0.628$

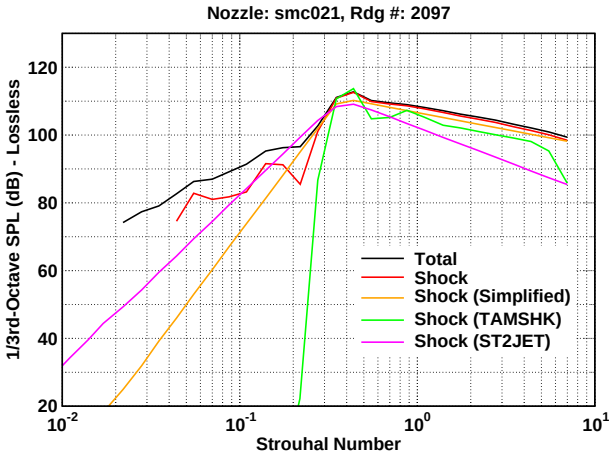

(o) $M_j = 1.390, \text{NPR} = 3.130, T_t/T_\infty = 2.16, \beta = 0.966$

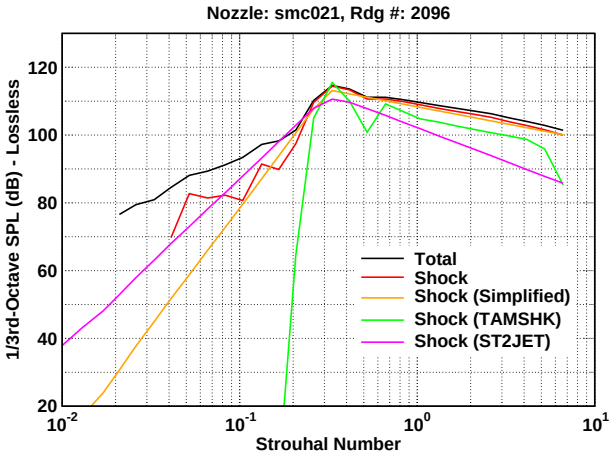

(p) $M_j = 1.494, \text{NPR} = 3.629, T_t/T_\infty = 2.16, \beta = 1.109$

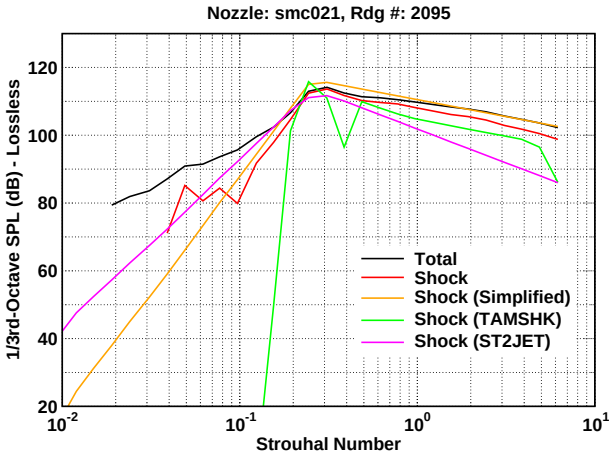

(q) $M_j = 1.660, \text{NPR} = 4.638, T_t/T_\infty = 2.16, \beta = 1.324$

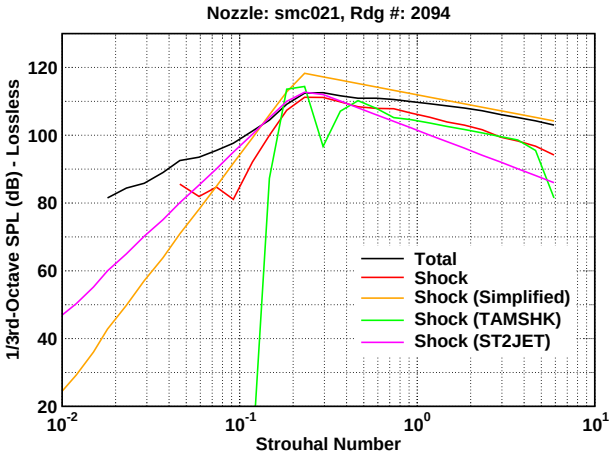

(r) $M_j = 1.794, \text{NPR} = 5.685, T_t/T_\infty = 2.16, \beta = 1.489$

Figure 10: (50 Deg., Cont.)

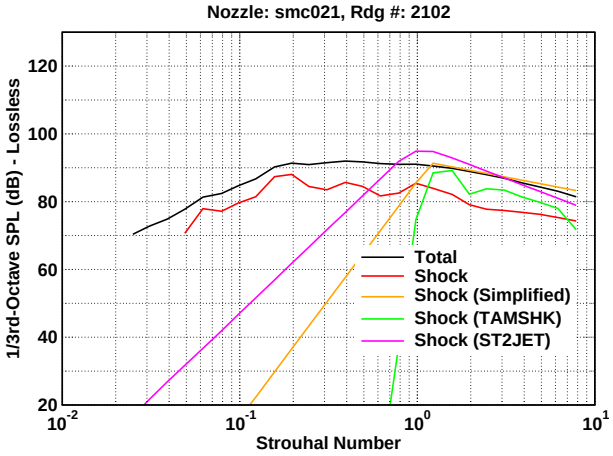

(s) $M_j = 1.048, \text{NPR} = 1.987, T_t/T_\infty = 2.66, \beta = 0.314$

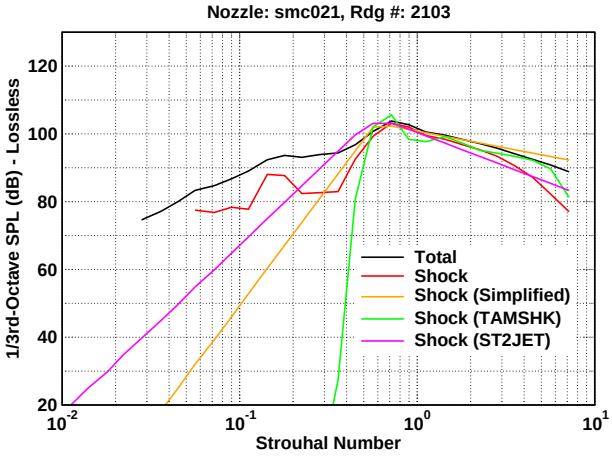

(t) $M_j = 1.175, \text{NPR} = 2.327, T_t/T_\infty = 2.65, \beta = 0.617$

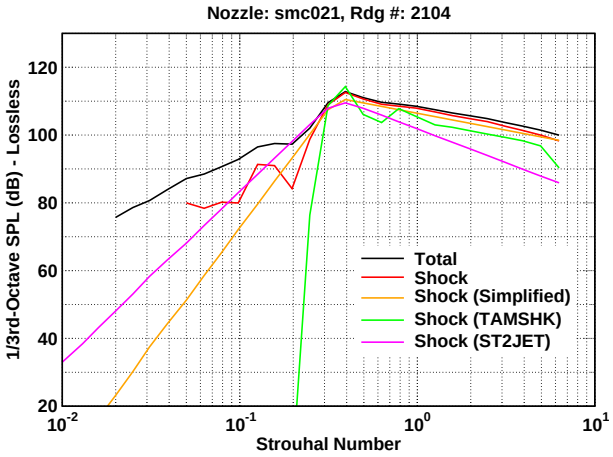

(u) $M_j = 1.391, \text{NPR} = 3.120, T_t/T_\infty = 2.66, \beta = 0.967$

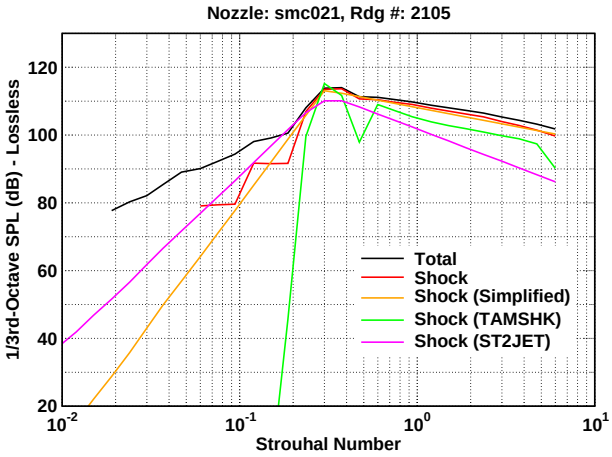

(v) $M_j = 1.490, \text{NPR} = 3.597, T_t/T_\infty = 2.65, \beta = 1.105$

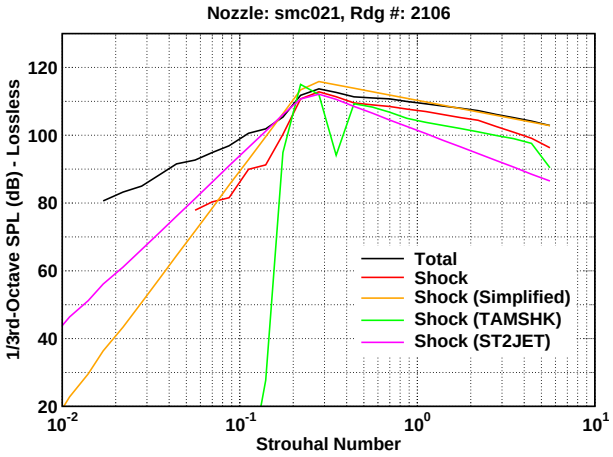

(w) $M_j = 1.660, \text{NPR} = 4.630, T_t/T_\infty = 2.64, \beta = 1.325$

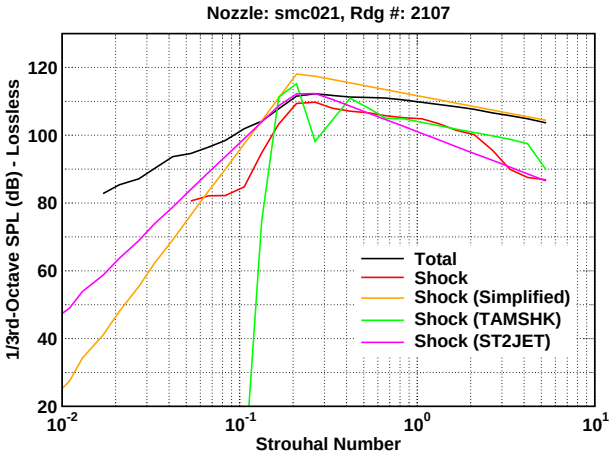

(x) $M_j = 1.789, \text{NPR} = 5.638, T_t/T_\infty = 2.65, \beta = 1.484$

Figure 10: (50 Deg., Cont.)

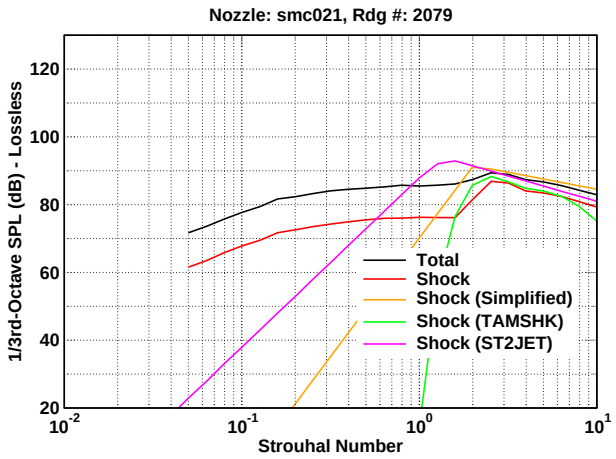

(a) $M_j = 1.049, \text{NPR} = 2.005, T_t/T_\infty = 1.01, \beta = 0.315$

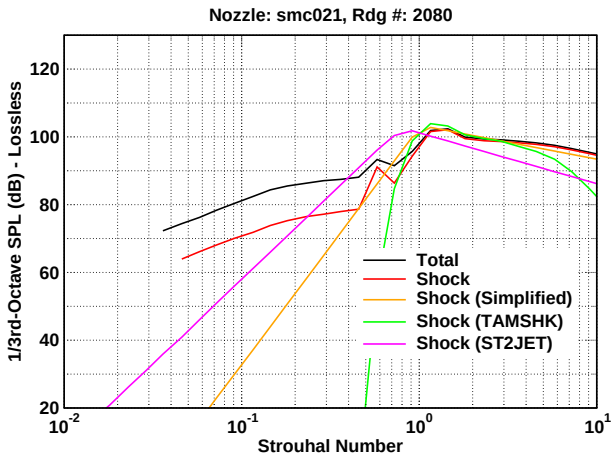

(b) $M_j = 1.178, \text{NPR} = 2.358, T_t/T_\infty = 1.01, \beta = 0.623$

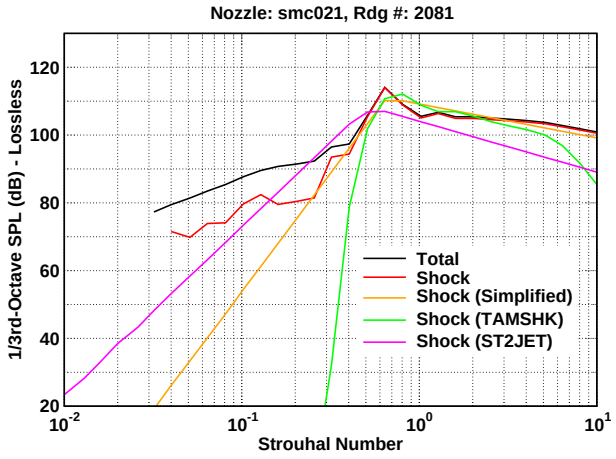

(c) $M_j = 1.392, \text{NPR} = 3.147, T_t/T_\infty = 1.01, \beta = 0.969$

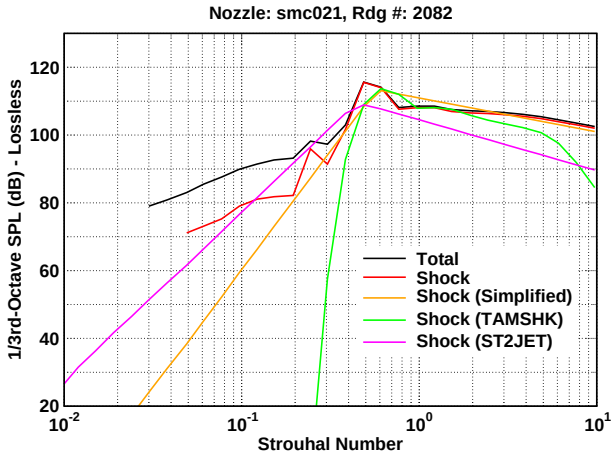

(d) $M_j = 1.493, \text{NPR} = 3.636, T_t/T_\infty = 1.01, \beta = 1.109$

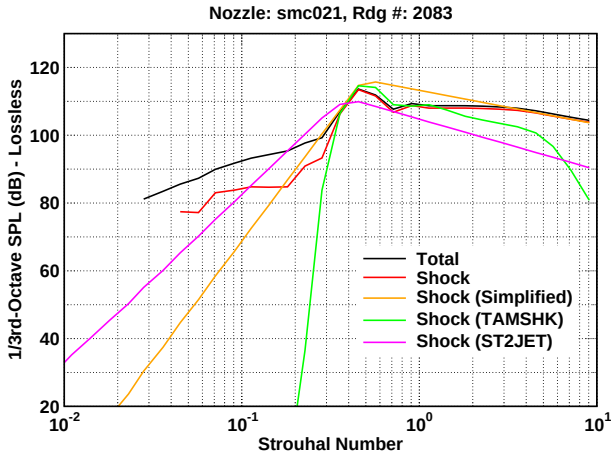

(e) $M_j = 1.660, \text{NPR} = 4.647, T_t/T_\infty = 1.01, \beta = 1.325$

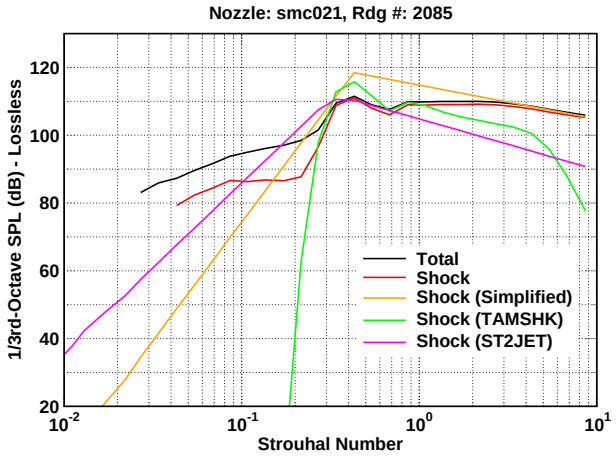

(f) $M_j = 1.796, \text{NPR} = 5.708, T_t/T_\infty = 1.01, \beta = 1.491$

Figure 11: 1/3-Octave spectra comparisons of jet shock-associated noise prediction models to the shock-associated noise component spectra for measured data from jets with shocks at a 90 degree inlet angle and distance $100D$.

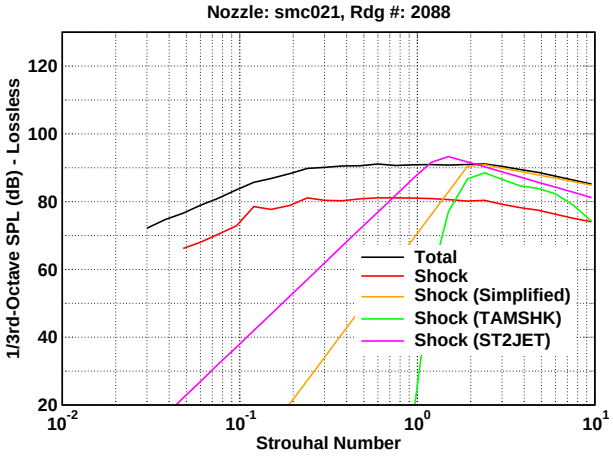

(g) $M_j = 1.049, \text{NPR} = 2.004, T_t/T_\infty = 1.77, \beta = 0.319$

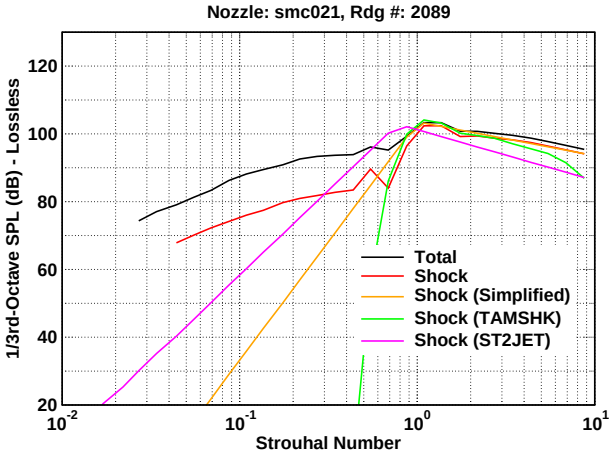

(h) $M_j = 1.182, \text{NPR} = 2.365, T_t/T_\infty = 1.77, \beta = 0.630$

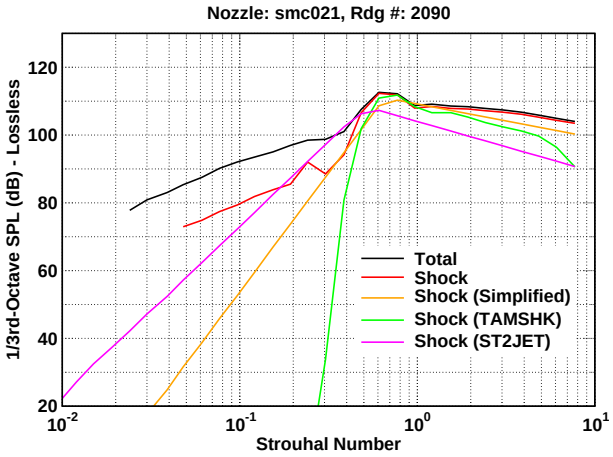

(i) $M_j = 1.392, \text{NPR} = 3.143, T_t/T_\infty = 1.76, \beta = 0.968$

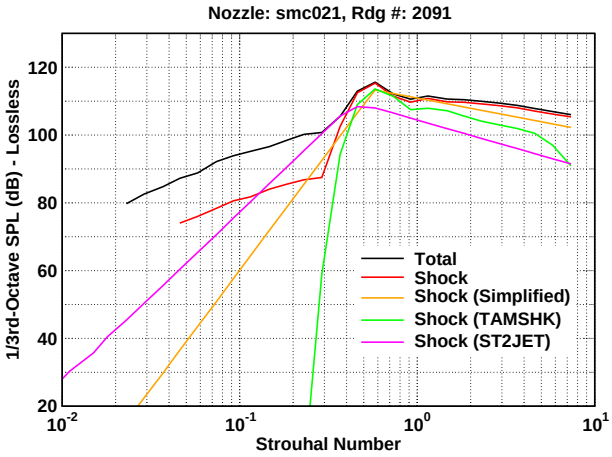

(j) $M_j = 1.492, \text{NPR} = 3.627, T_t/T_\infty = 1.76, \beta = 1.108$

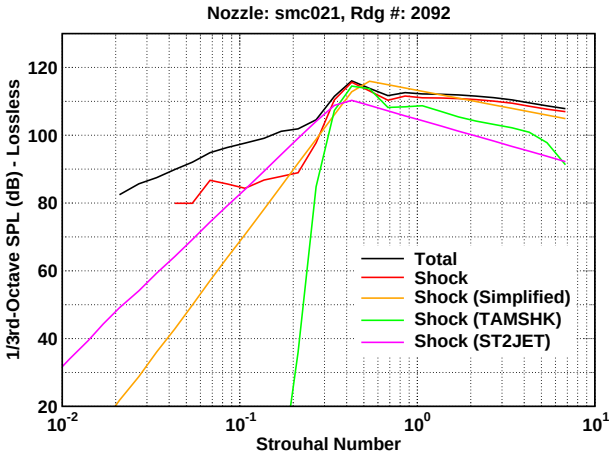

(k) $M_j = 1.660, \text{NPR} = 4.644, T_t/T_\infty = 1.77, \beta = 1.325$

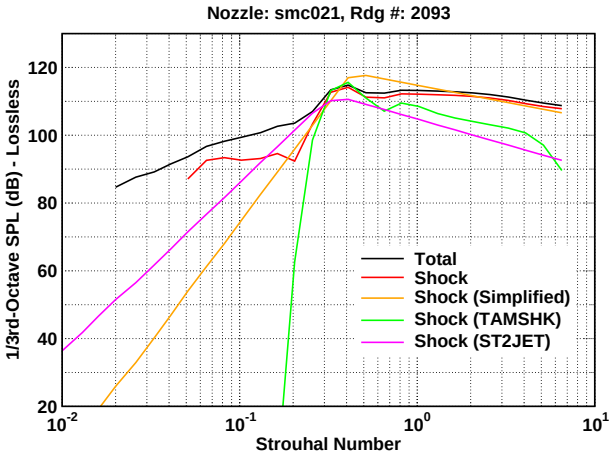

(l) $M_j = 1.792, \text{NPR} = 5.674, T_t/T_\infty = 1.76, \beta = 1.487$

Figure 11: (90 Deg., Cont.)

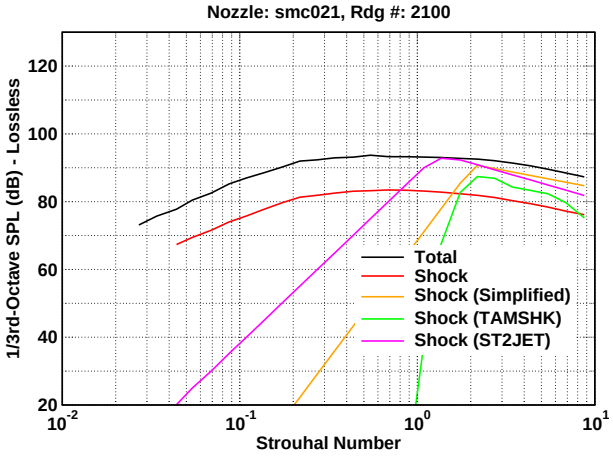

(m) $M_j = 1.045, \text{NPR} = 1.989, T_t/T_\infty = 2.16, \beta = 0.305$

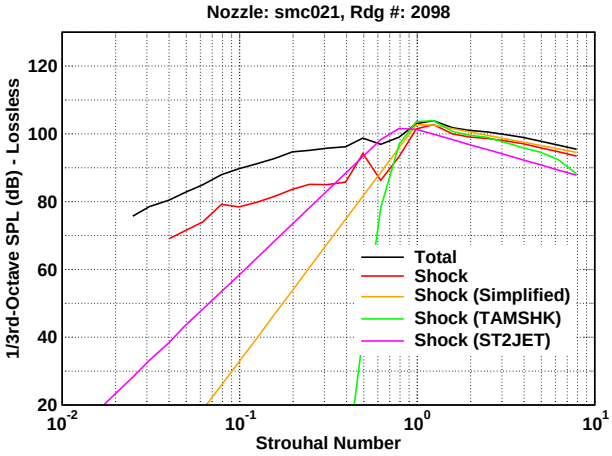

(n) $M_j = 1.181, \text{NPR} = 2.356, T_t/T_\infty = 2.16, \beta = 0.628$

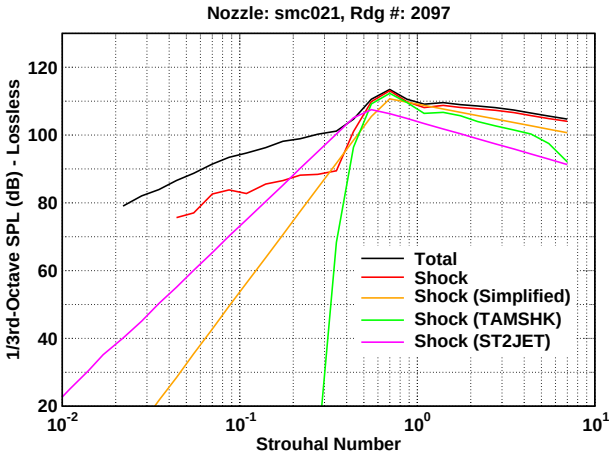

(o) $M_j = 1.390, \text{NPR} = 3.130, T_t/T_\infty = 2.16, \beta = 0.966$

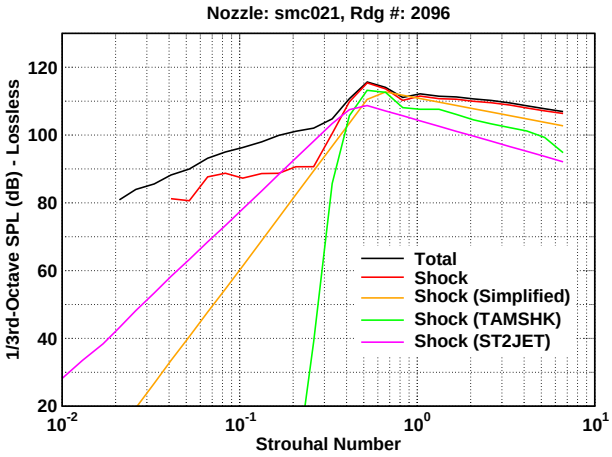

(p) $M_j = 1.494, \text{NPR} = 3.629, T_t/T_\infty = 2.16, \beta = 1.109$

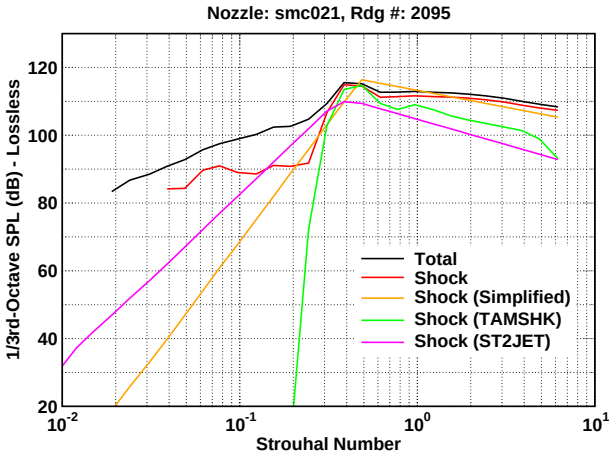

(q) $M_j = 1.660, \text{NPR} = 4.638, T_t/T_\infty = 2.16, \beta = 1.324$

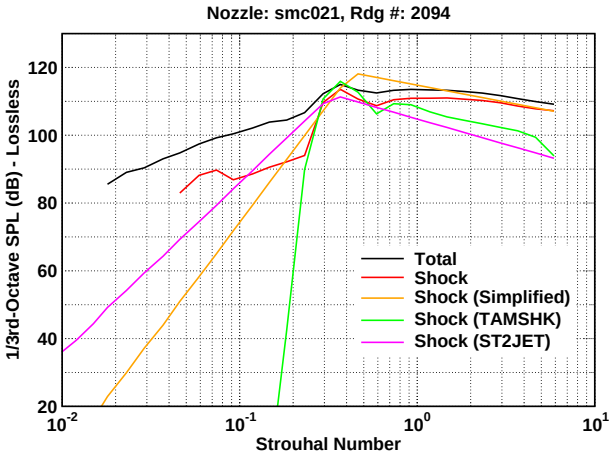

(r) $M_j = 1.794, \text{NPR} = 5.685, T_t/T_\infty = 2.16, \beta = 1.489$

Figure 11: (90 Deg., Cont.)

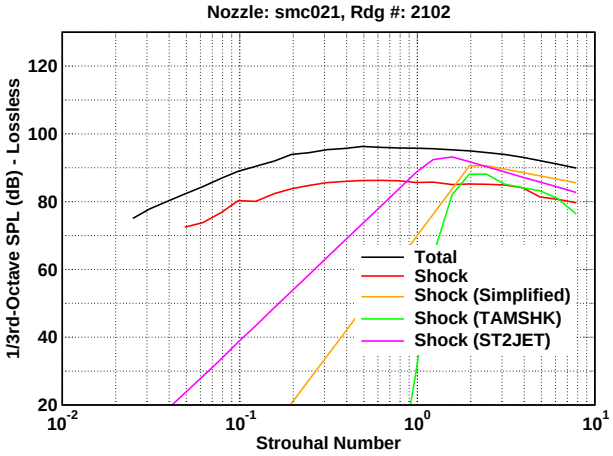

(s) $M_j = 1.048, \text{NPR} = 1.987, T_t/T_\infty = 2.66, \beta = 0.314$

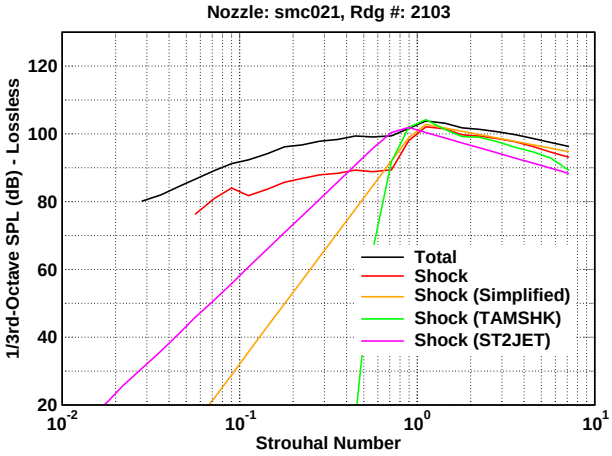

(t) $M_j = 1.175, \text{NPR} = 2.327, T_t/T_\infty = 2.65, \beta = 0.617$

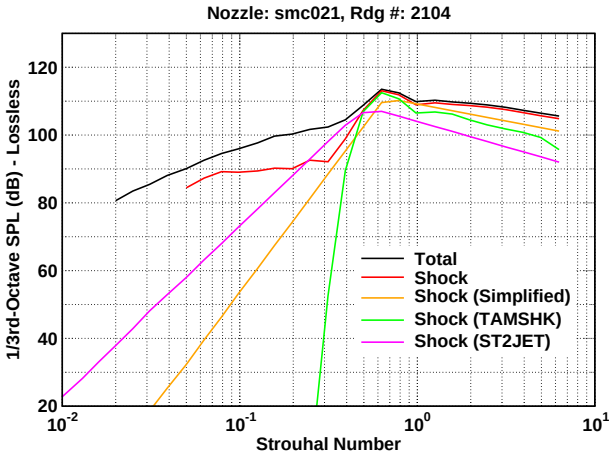

(u) $M_j = 1.391, \text{NPR} = 3.120, T_t/T_\infty = 2.66, \beta = 0.967$

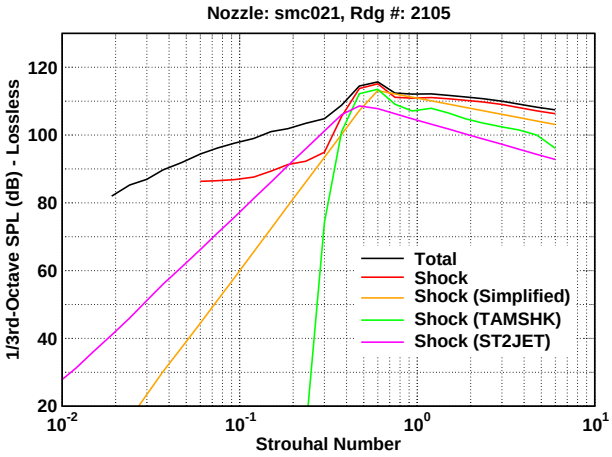

(v) $M_j = 1.490, \text{NPR} = 3.597, T_t/T_\infty = 2.65, \beta = 1.105$

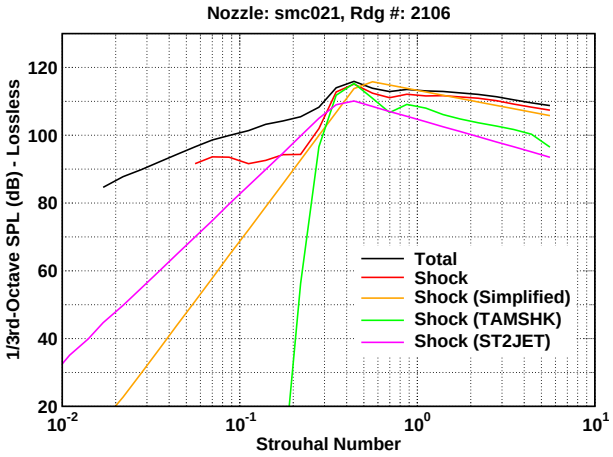

(w) $M_j = 1.660, \text{NPR} = 4.630, T_t/T_\infty = 2.64, \beta = 1.325$

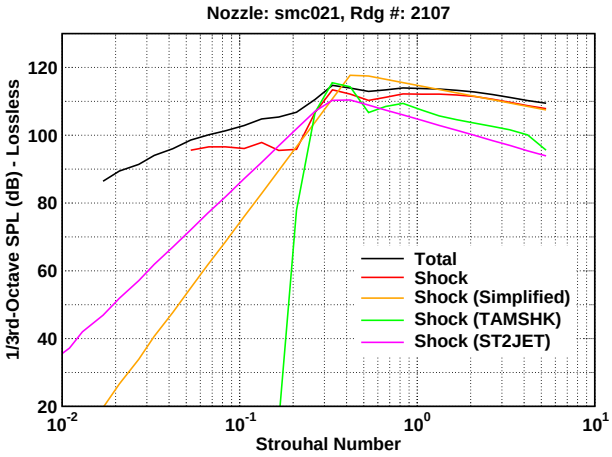

(x) $M_j = 1.789, \text{NPR} = 5.638, T_t/T_\infty = 2.65, \beta = 1.484$

Figure 11: (90 Deg., Cont.)

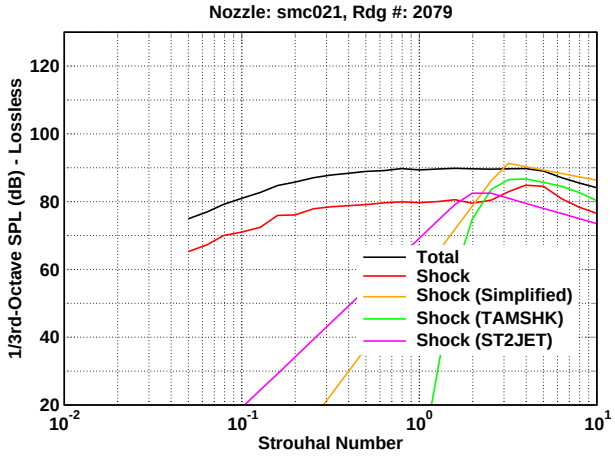

(a) $M_j = 1.049, \text{NPR} = 2.005, T_t/T_\infty = 1.01, \beta = 0.315$

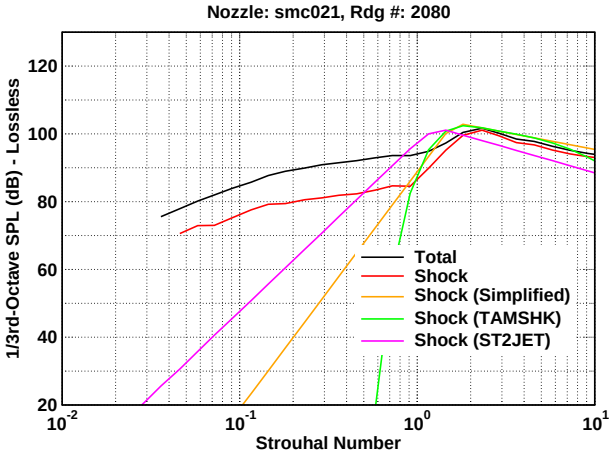

(b) $M_j = 1.178, \text{NPR} = 2.358, T_t/T_\infty = 1.01, \beta = 0.623$

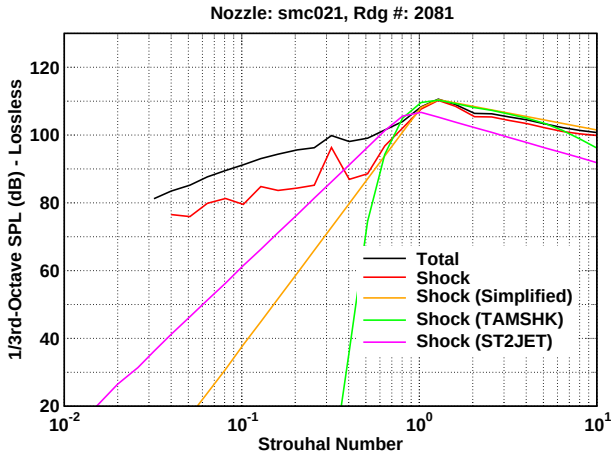

(c) $M_j = 1.392, \text{NPR} = 3.147, T_t/T_\infty = 1.01, \beta = 0.969$

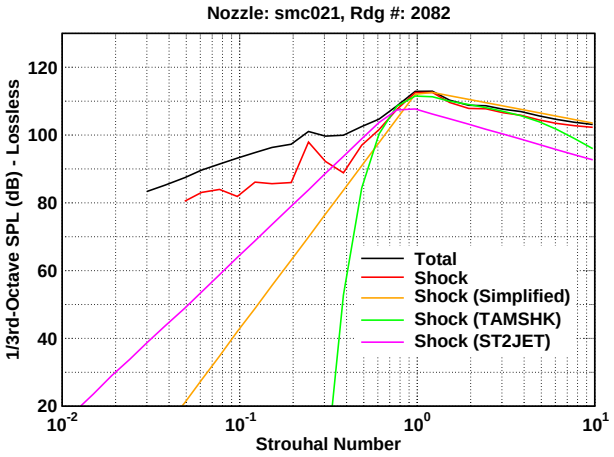

(d) $M_j = 1.493, \text{NPR} = 3.636, T_t/T_\infty = 1.01, \beta = 1.109$

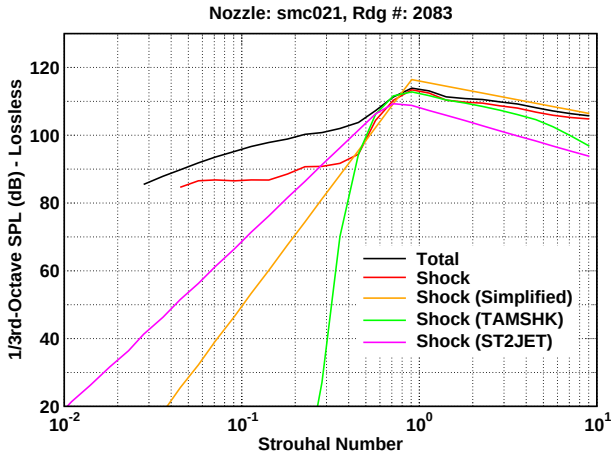

(e) $M_j = 1.660, \text{NPR} = 4.647, T_t/T_\infty = 1.01, \beta = 1.325$

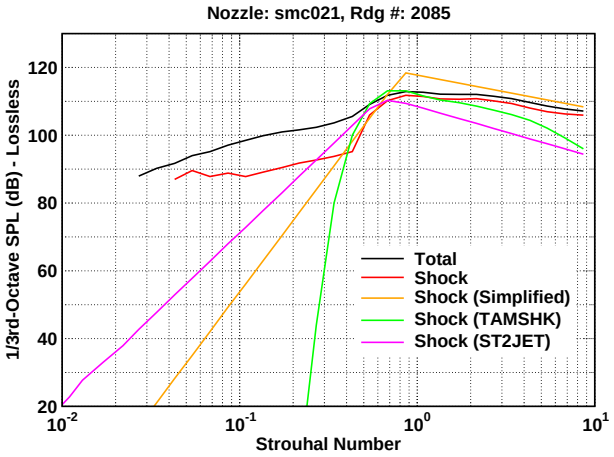

(f) $M_j = 1.796, \text{NPR} = 5.708, T_t/T_\infty = 1.01, \beta = 1.491$

Figure 12: 1/3-Octave spectra comparisons of jet shock-associated noise prediction models to the shock-associated noise component spectra for measured data from jets with shocks at a 120 degree inlet angle and distance $100D$.

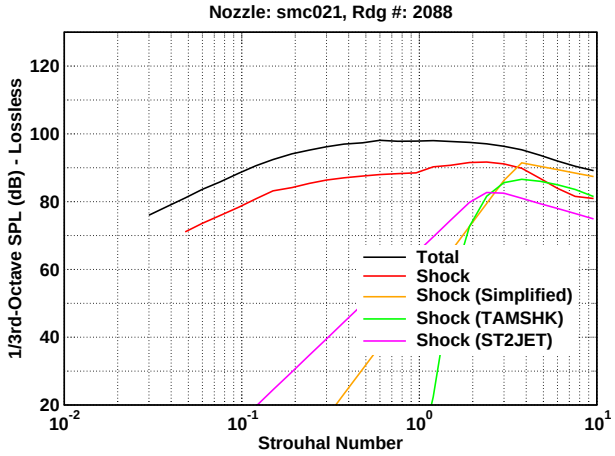

(g) $M_j = 1.049, \text{NPR} = 2.004, T_t/T_\infty = 1.77, \beta = 0.319$

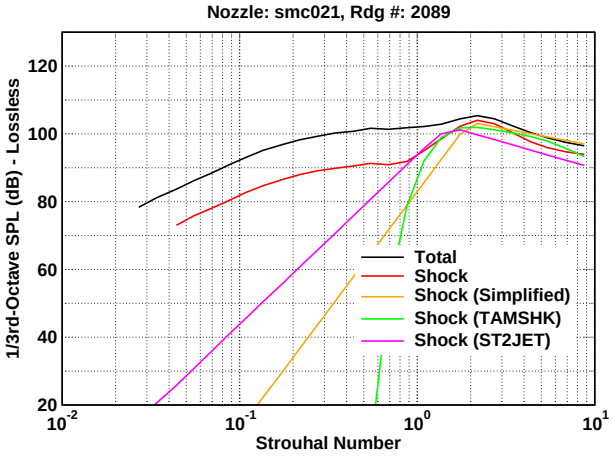

(h) $M_j = 1.182, \text{NPR} = 2.365, T_t/T_\infty = 1.77, \beta = 0.630$

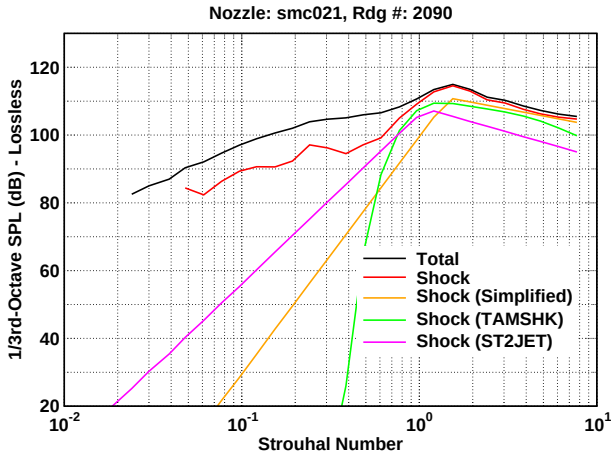

(i) $M_j = 1.392, \text{NPR} = 3.143, T_t/T_\infty = 1.76, \beta = 0.968$

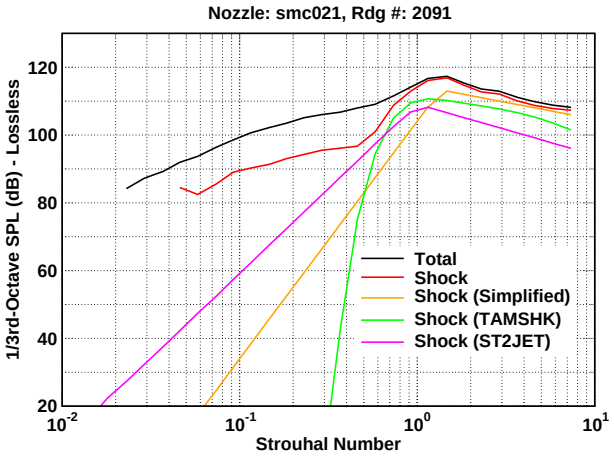

(j) $M_j = 1.492, \text{NPR} = 3.627, T_t/T_\infty = 1.76, \beta = 1.108$

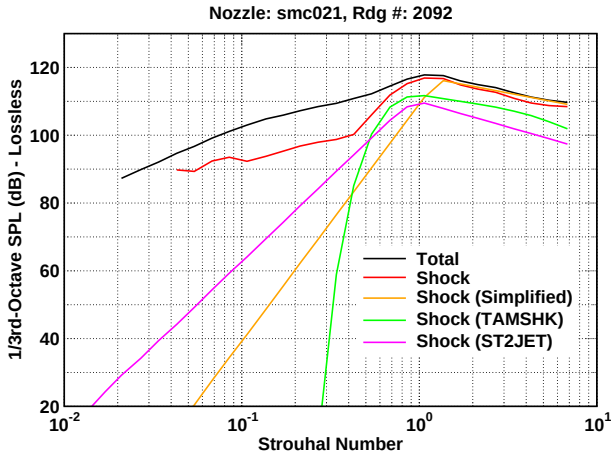

(k) $M_j = 1.660, \text{NPR} = 4.644, T_t/T_\infty = 1.77, \beta = 1.325$

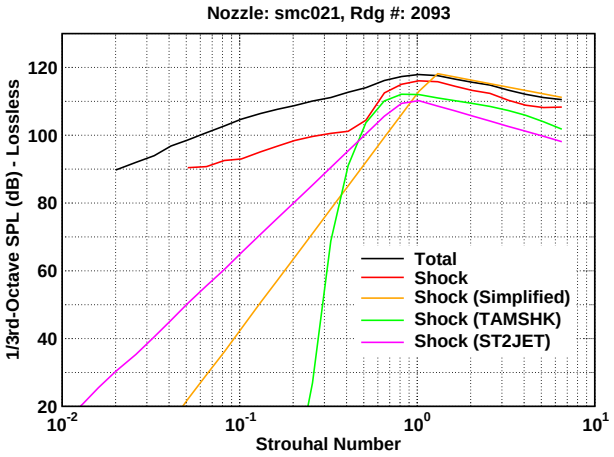

(l) $M_j = 1.792, \text{NPR} = 5.674, T_t/T_\infty = 1.76, \beta = 1.487$

Figure 12: (120 Deg., Cont.)

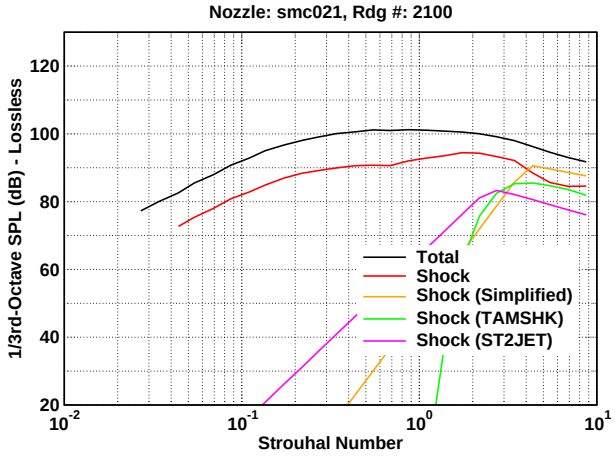

(m) $M_j = 1.045, \text{NPR} = 1.989, T_t/T_\infty = 2.16, \beta = 0.305$

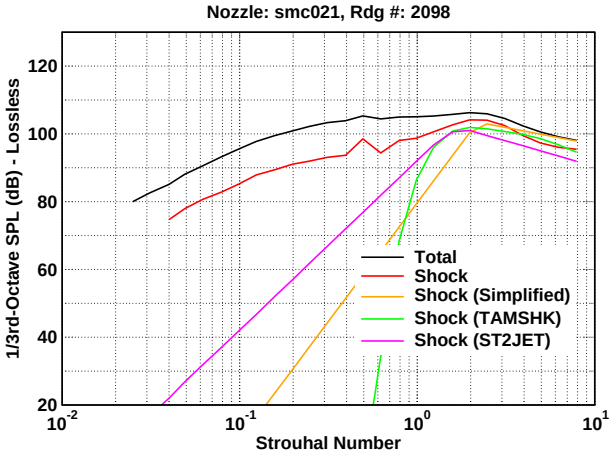

(n) $M_j = 1.181, \text{NPR} = 2.356, T_t/T_\infty = 2.16, \beta = 0.628$

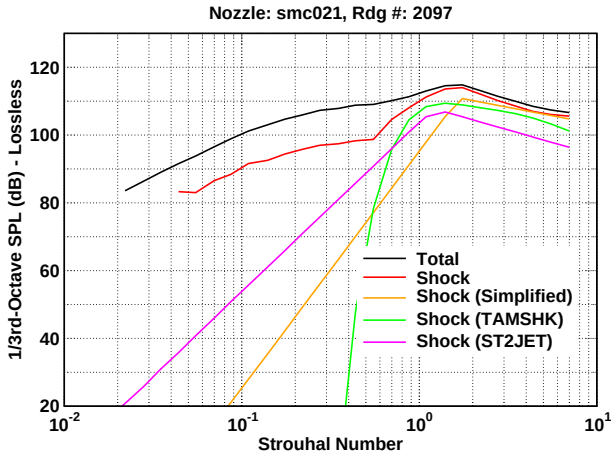

(o) $M_j = 1.390, \text{NPR} = 3.130, T_t/T_\infty = 2.16, \beta = 0.966$

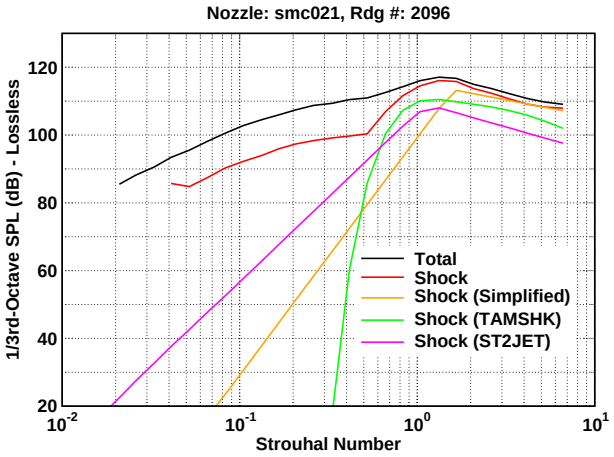

(p) $M_j = 1.494, \text{NPR} = 3.629, T_t/T_\infty = 2.16, \beta = 1.109$

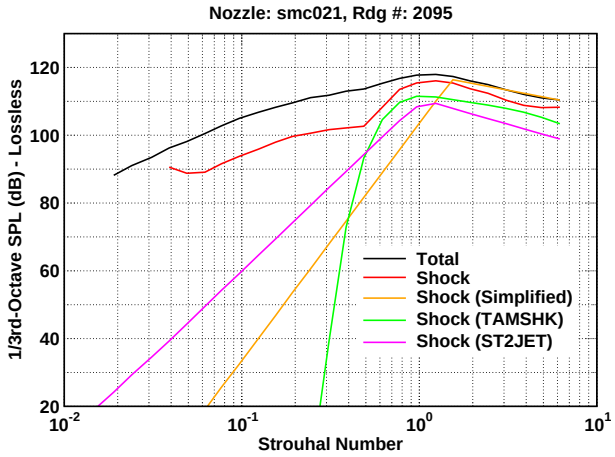

(q) $M_j = 1.660, \text{NPR} = 4.638, T_t/T_\infty = 2.16, \beta = 1.324$

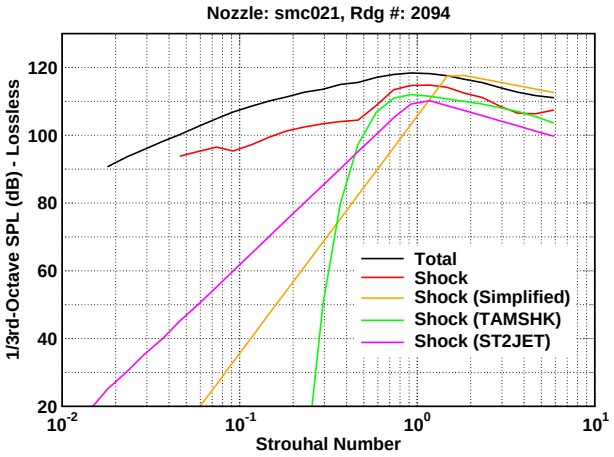

(r) $M_j = 1.794, \text{NPR} = 5.685, T_t/T_\infty = 2.16, \beta = 1.489$

Figure 12: (120 Deg., Cont.)

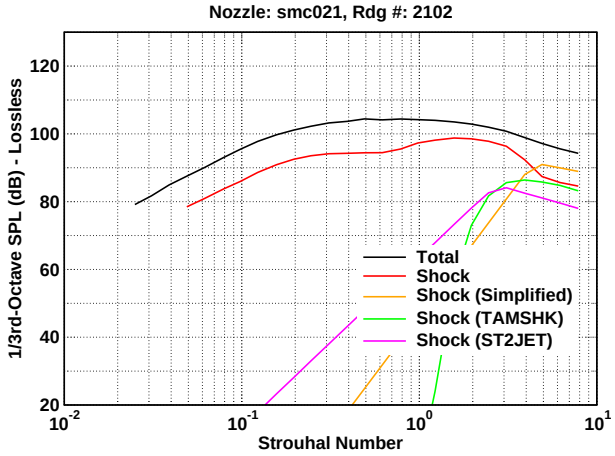

(s) $M_j = 1.048, \text{NPR} = 1.987, T_t/T_\infty = 2.66, \beta = 0.314$

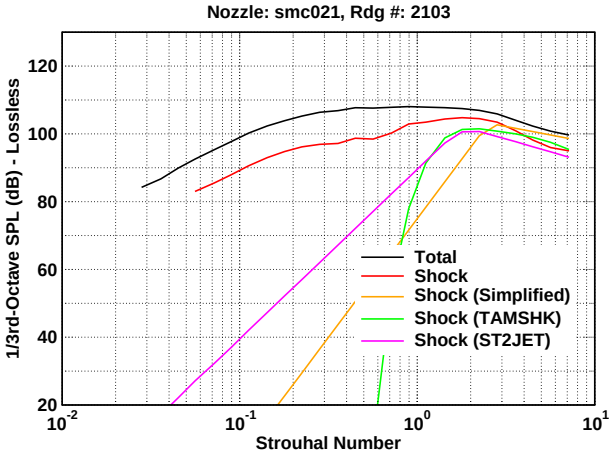

(t) $M_j = 1.175, \text{NPR} = 2.327, T_t/T_\infty = 2.65, \beta = 0.617$

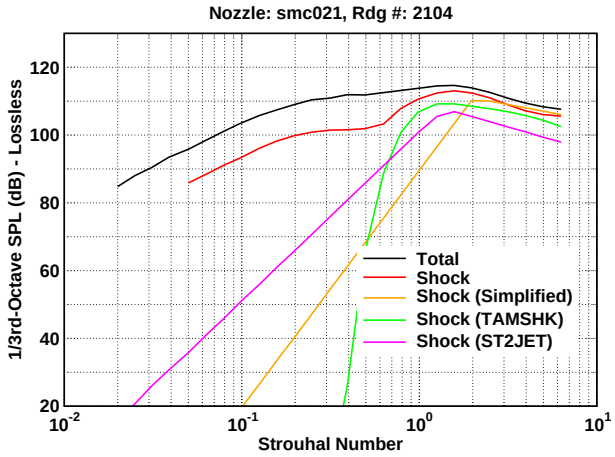

(u) $M_j = 1.391, \text{NPR} = 3.120, T_t/T_\infty = 2.66, \beta = 0.967$

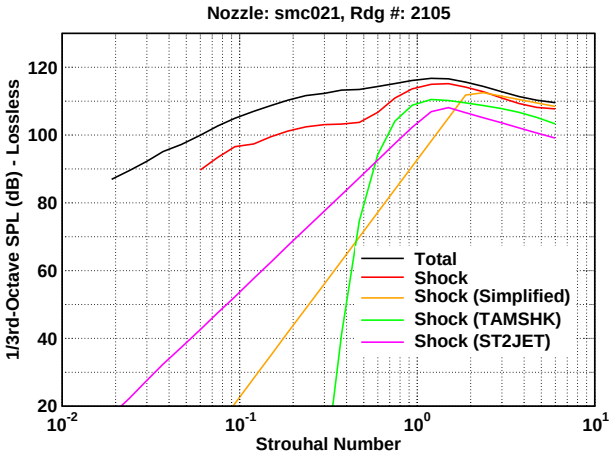

(v) $M_j = 1.490, \text{NPR} = 3.597, T_t/T_\infty = 2.65, \beta = 1.105$

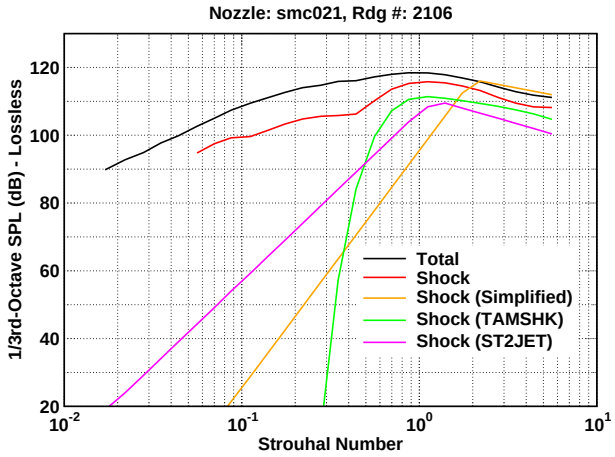

(w) $M_j = 1.660, \text{NPR} = 4.630, T_t/T_\infty = 2.64, \beta = 1.325$

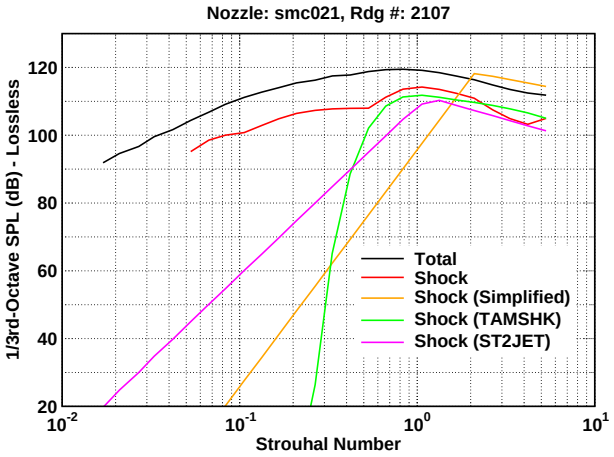

(x) $M_j = 1.789, \text{NPR} = 5.638, T_t/T_\infty = 2.65, \beta = 1.484$

Figure 12: (120 Deg., Cont.)

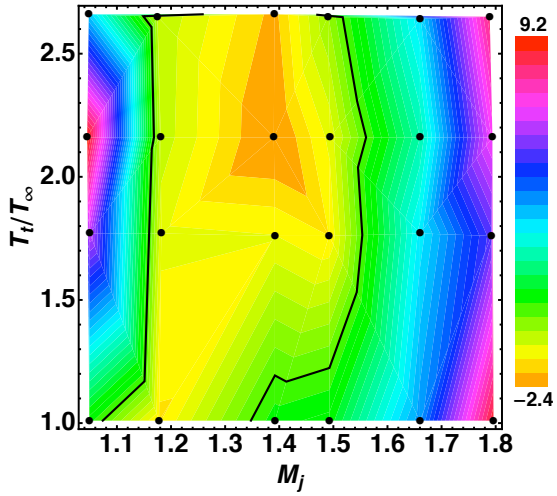

(a) Peak level error, 50 degrees.

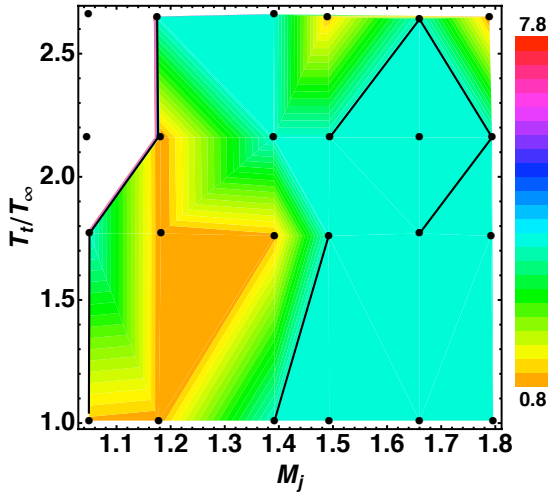

(d) Peak frequency error, 50 degrees.

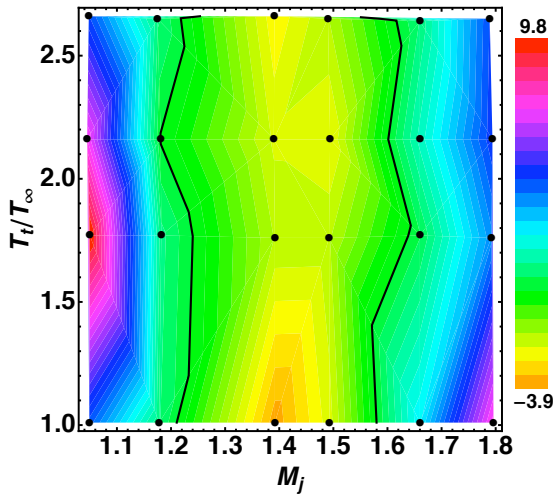

(b) Peak level error, 90 degrees.

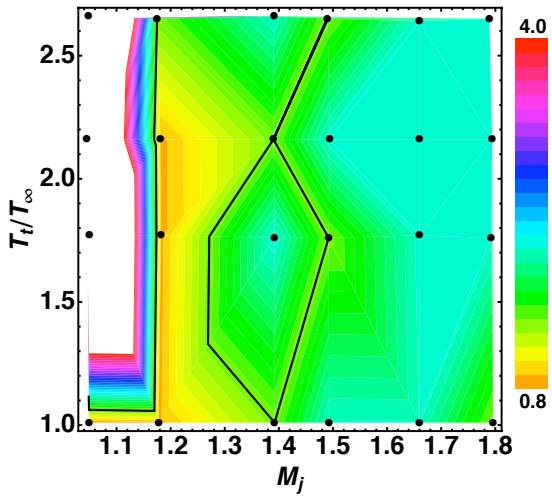

(e) Peak frequency error, 90 degrees.

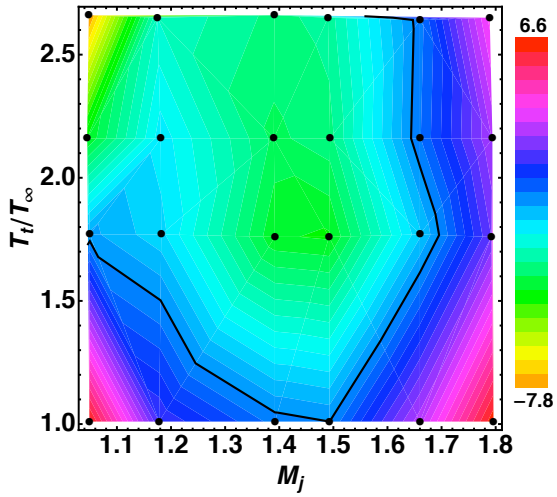

(c) Peak level error, 120 degrees.

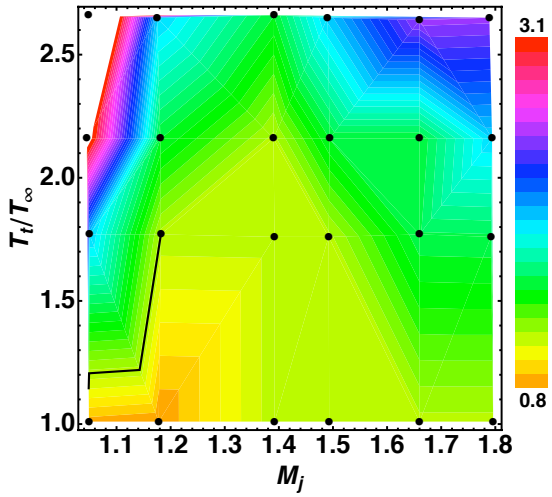

(f) Peak frequency error, 120 degrees.

Figure 13: Simplified Model. (a-c) Error in broadband shock-associated noise 1/3-octave band peak level (dB(predicted) - dB(measured)). Black line = 0 dB. (d-f) Relative 1/3-octave band peak frequency f_p(predicted)/f_p(measured). Black line = 1. Data located at positions of black dots.

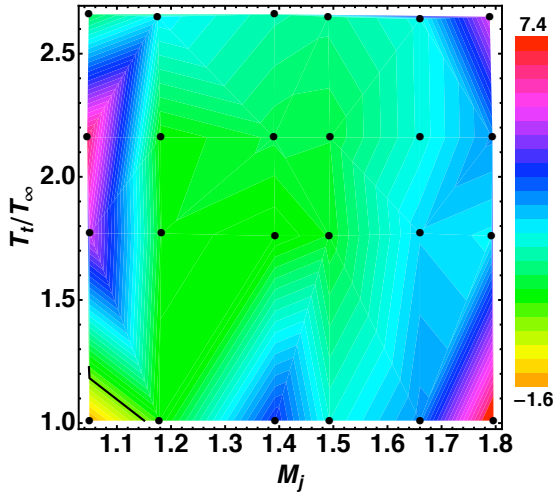

(a) Peak level error, 50 degrees.

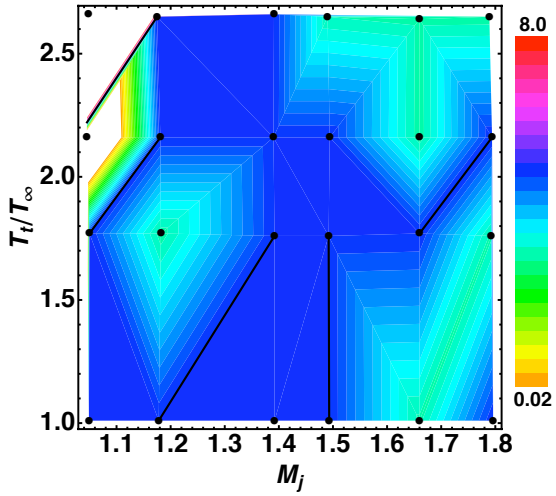

(d) Peak frequency error, 50 degrees.

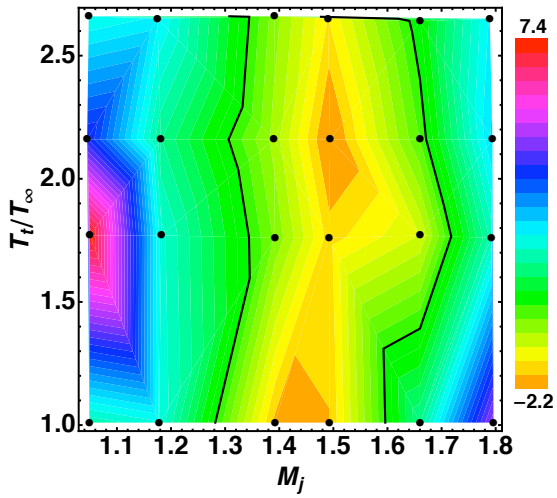

(b) Peak level error, 90 degrees.

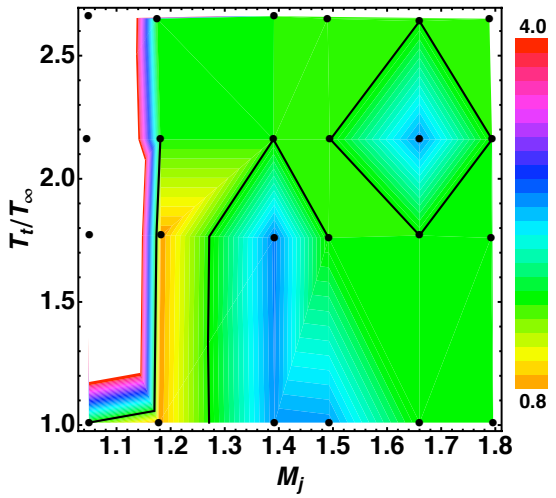

(e) Peak frequency error, 90 degrees.

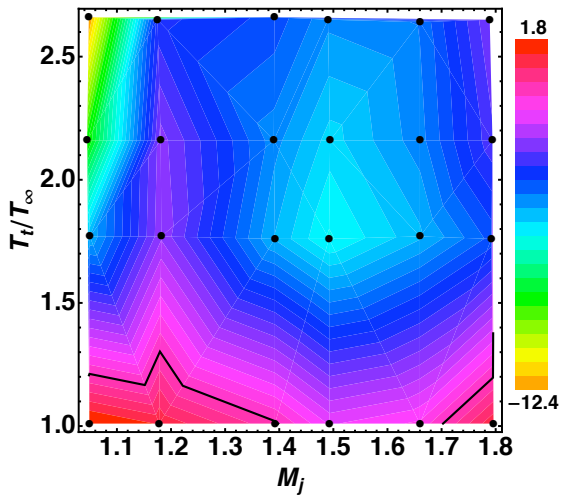

(c) Peak level error, 120 degrees.

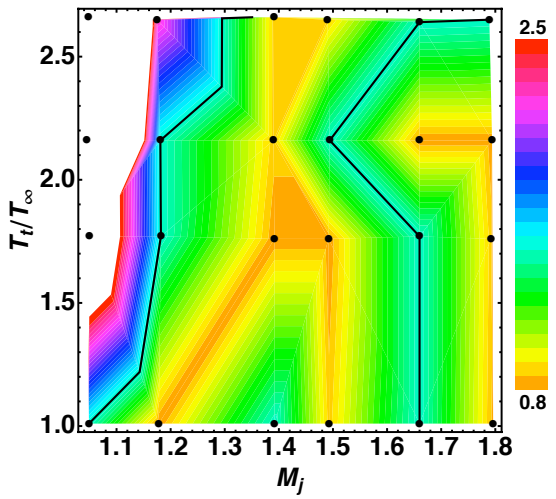

(f) Peak frequency error, 120 degrees.

Figure 14: TAMSHK Module. (a-c) Error in broadband shock-associated noise 1/3-octave band peak level (dB(predicted) - dB(measured)). Black line = 0 dB. (d-f) Relative 1/3-octave band peak frequency f_p(predicted)/f_p(measured). Black line = 1. Data located at positions of black dots.

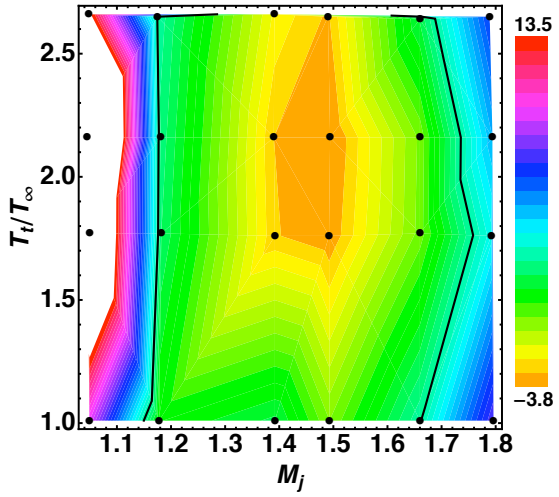

(a) Peak level error, 50 degrees.

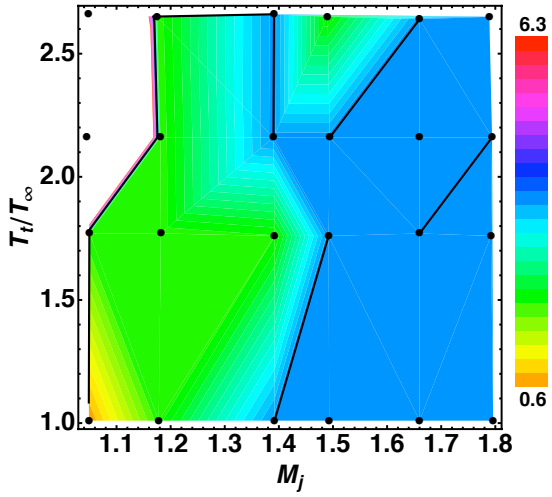

(d) Peak frequency error, 50 degrees.

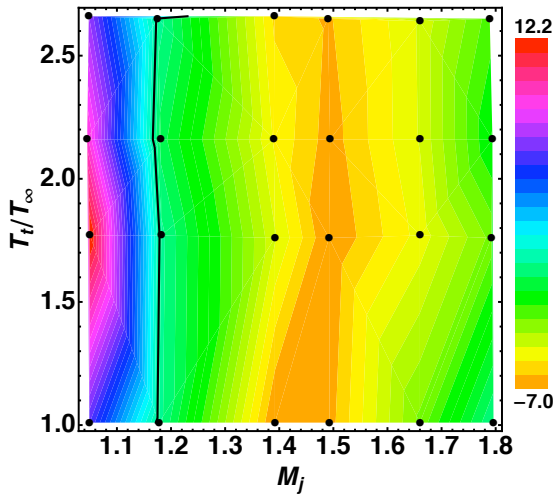

(b) Peak level error, 90 degrees.

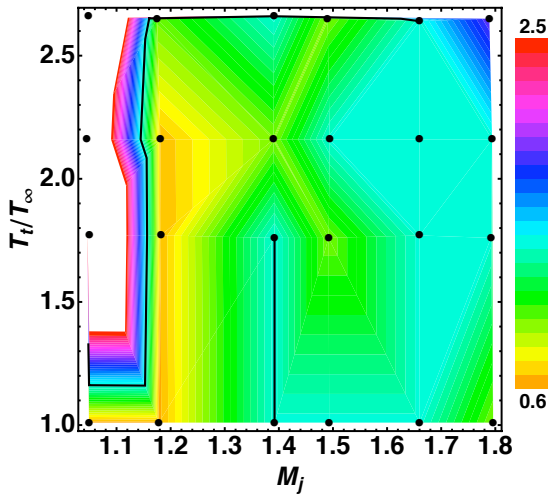

(e) Peak frequency error, 90 degrees.

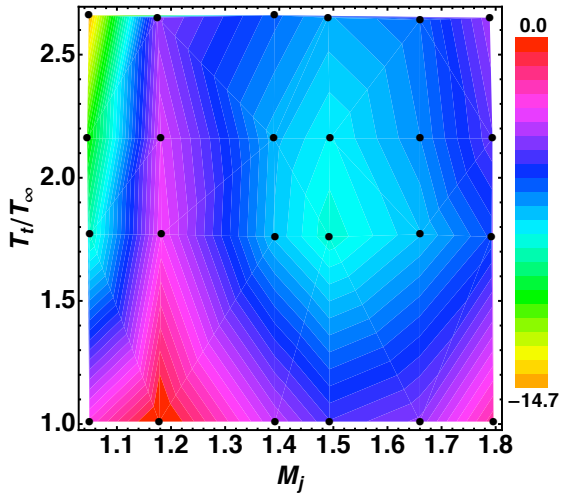

(c) Peak level error, 120 degrees.

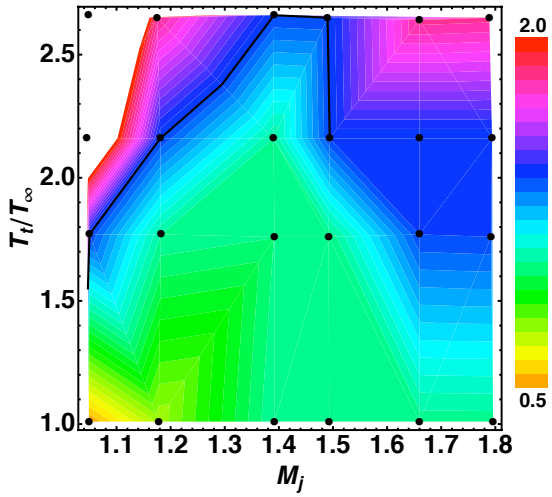

(f) Peak frequency error, 120 degrees.

Figure 15: ST2JET Module. (a-c) Error in broadband shock-associated noise 1/3-octave band peak level (dB(predicted) - dB(measured)). Black line = 0 dB. (d-f) Relative 1/3-octave band peak frequency f_p(predicted)/f_p(measured). Black line = 1. Data located at positions of black dots.

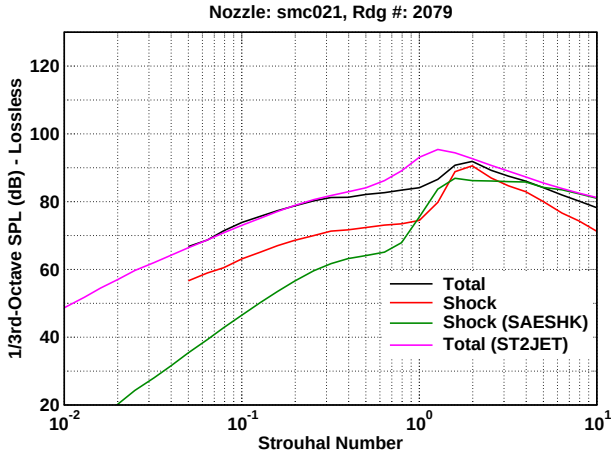

(a) $M_j = 1.049, \text{NPR} = 2.005, T_t/T_\infty = 1.01, \beta = 0.315$

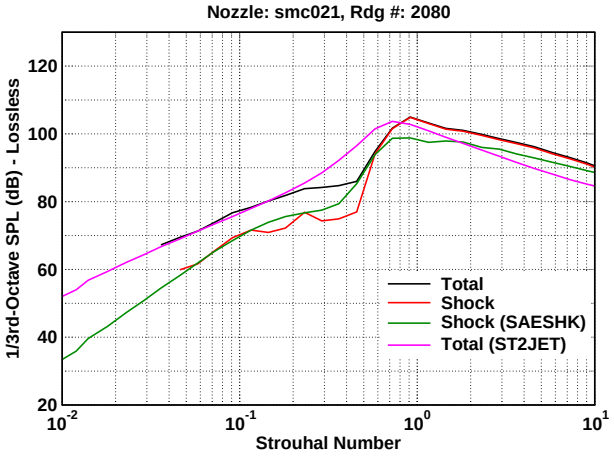

(b) $M_j = 1.178, \text{NPR} = 2.358, T_t/T_\infty = 1.01, \beta = 0.623$

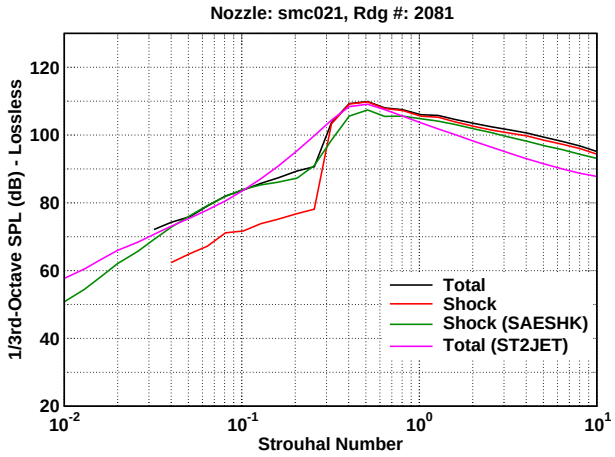

(c) $M_j = 1.392, \text{NPR} = 3.147, T_t/T_\infty = 1.01, \beta = 0.969$

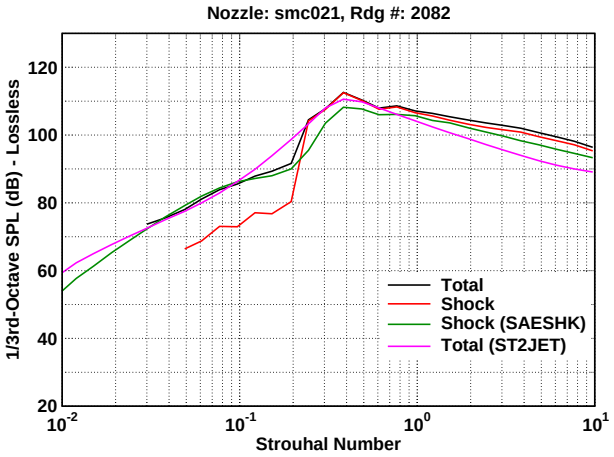

(d) $M_j = 1.493, \text{NPR} = 3.636, T_t/T_\infty = 1.01, \beta = 1.109$

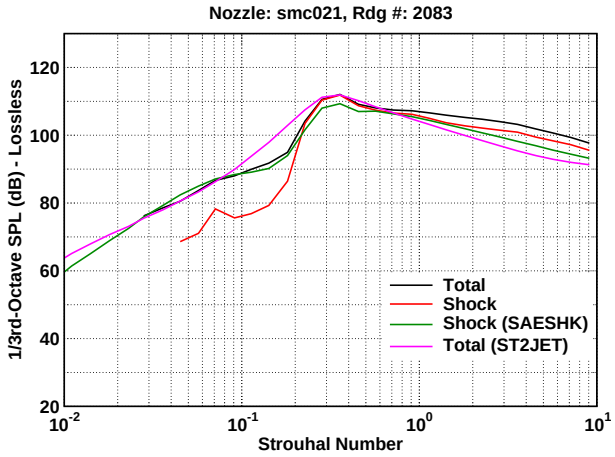

(e) $M_j = 1.660, \text{NPR} = 4.647, T_t/T_\infty = 1.01, \beta = 1.325$

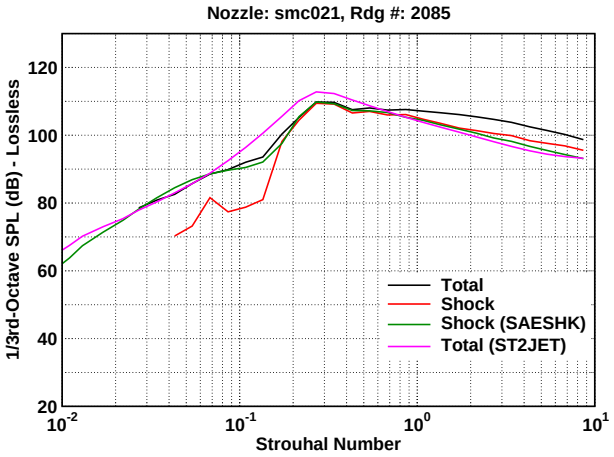

(f) $M_j = 1.796, \text{NPR} = 5.708, T_t/T_\infty = 1.01, \beta = 1.491$

Figure 16: 1/3-Octave spectra comparisons of jet noise prediction models to the total and shock component noise spectra for measured data from jets with shocks at a 50 degree inlet angle and distance $100D$.

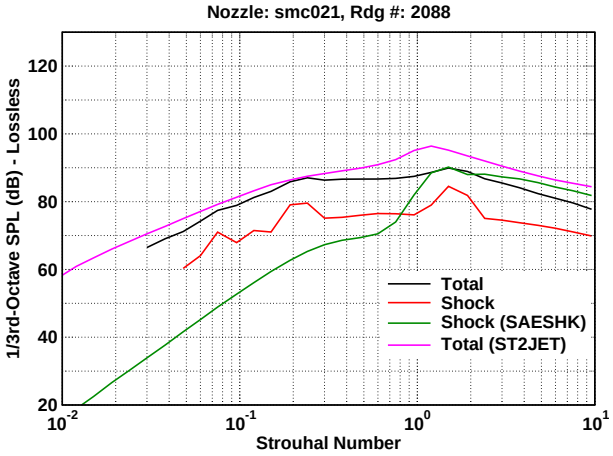

(g) $M_j = 1.050, \text{NPR} = 2.004, T_t/T_\infty = 1.77, \beta = 0.319$

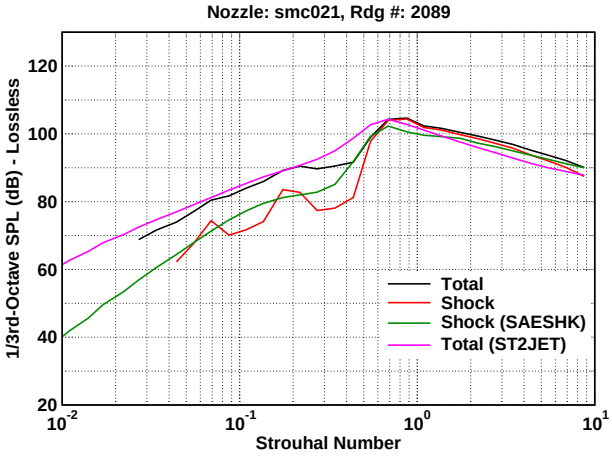

(h) $M_j = 1.182, \text{NPR} = 2.365, T_t/T_\infty = 1.77, \beta = 0.630$

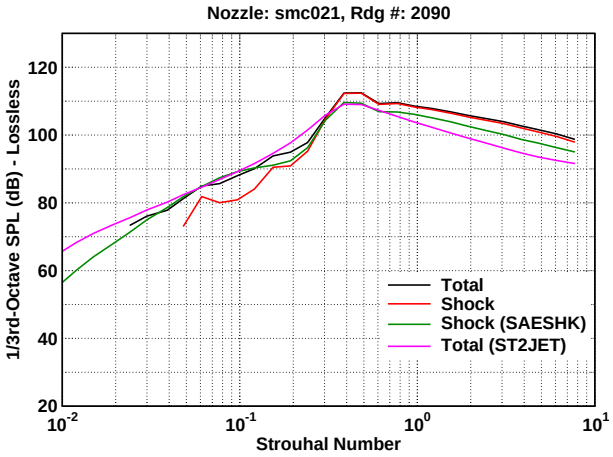

(i) $M_j = 1.392, \text{NPR} = 3.143, T_t/T_\infty = 1.76, \beta = 0.968$

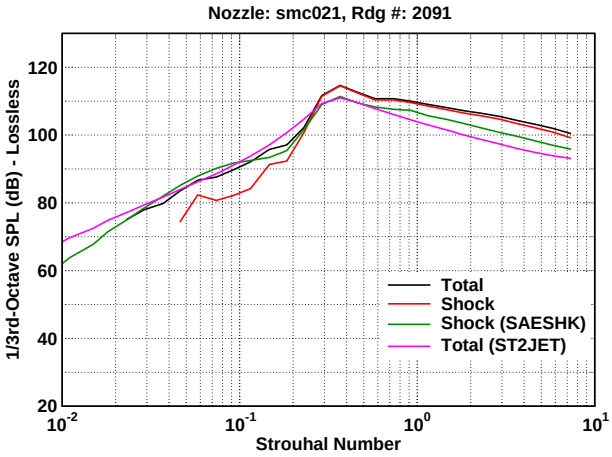

(j) $M_j = 1.492, \text{NPR} = 3.627, T_t/T_\infty = 1.76, \beta = 1.108$

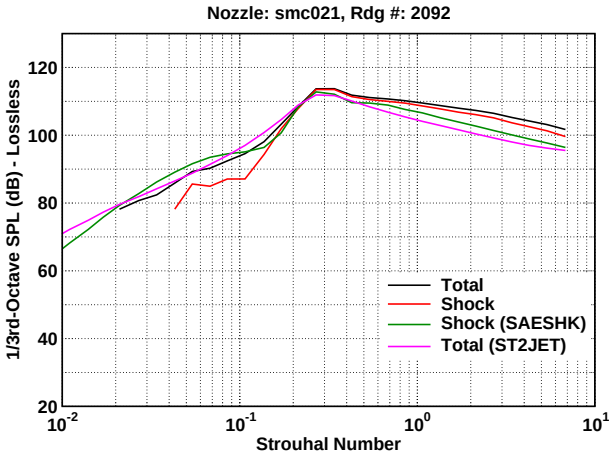

(k) $M_j = 1.660, \text{NPR} = 4.644, T_t/T_\infty = 1.77, \beta = 1.325$

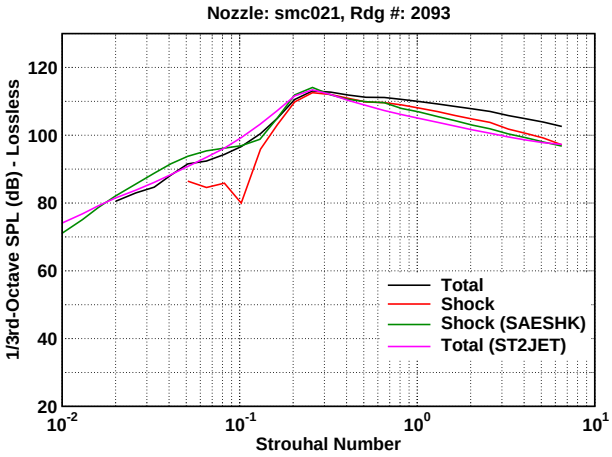

(l) $M_j = 1.792, \text{NPR} = 5.674, T_t/T_\infty = 1.76, \beta = 1.487$

Figure 16: (50 Deg., Cont.)

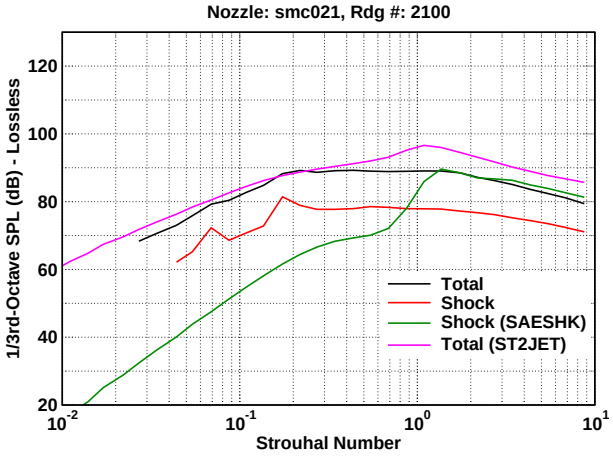

(m) $M_j = 1.045, \text{NPR} = 1.989, T_t/T_\infty = 2.16, \beta = 0.305$

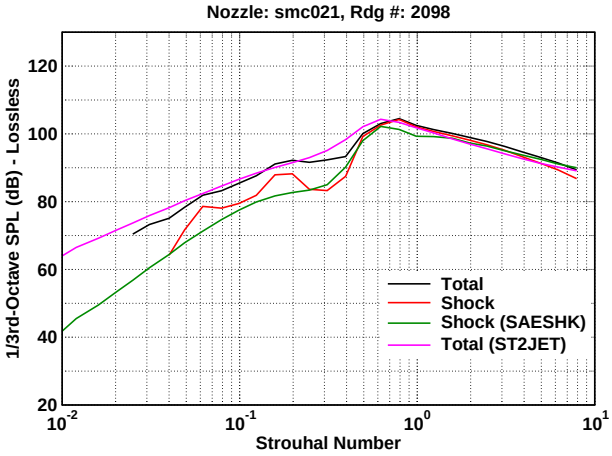

(n) $M_j = 1.181, \text{NPR} = 2.356, T_t/T_\infty = 2.16, \beta = 0.628$

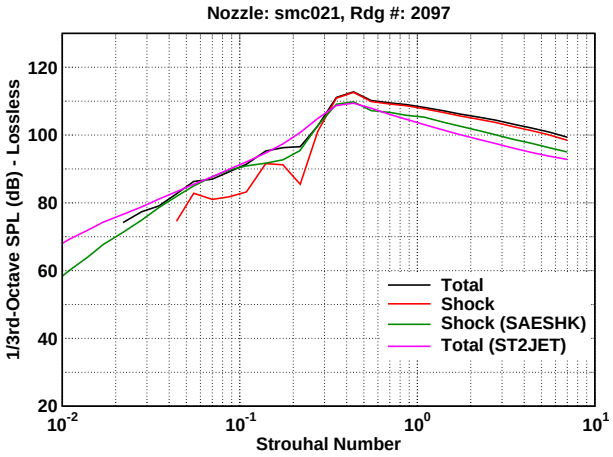

(o) $M_j = 1.390, \text{NPR} = 3.130, T_t/T_\infty = 2.16, \beta = 0.966$

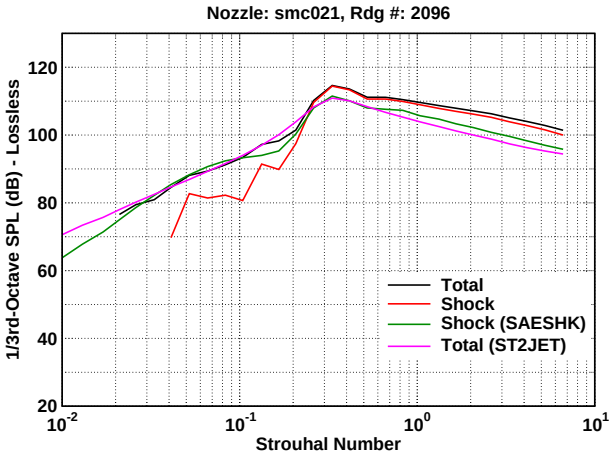

(p) $M_j = 1.494, \text{NPR} = 3.629, T_t/T_\infty = 2.16, \beta = 1.109$

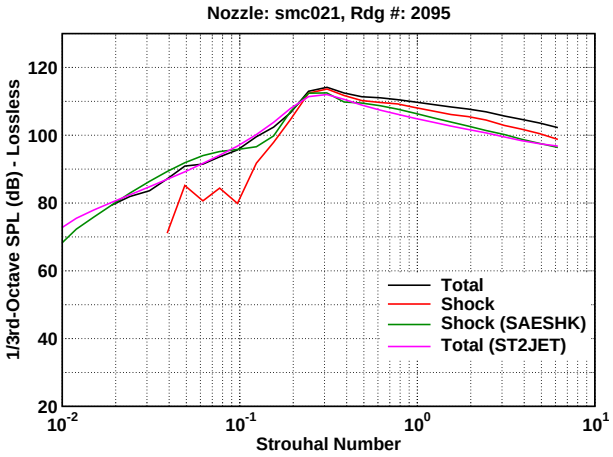

(q) $M_j = 1.660, \text{NPR} = 4.638, T_t/T_\infty = 2.16, \beta = 1.324$

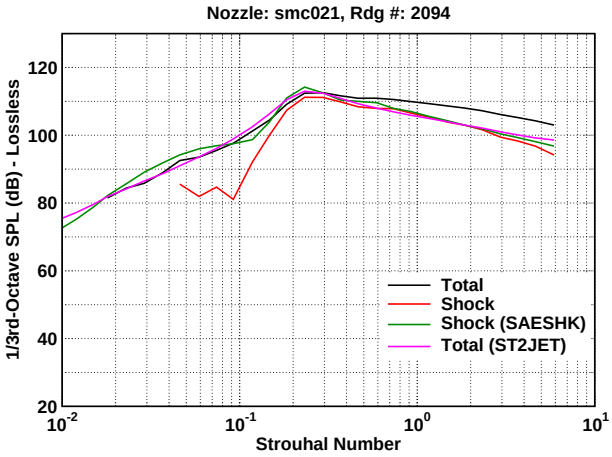

(r) $M_j = 1.794, \text{NPR} = 5.685, T_t/T_\infty = 2.16, \beta = 1.489$

Figure 16: (50 Deg., Cont.)

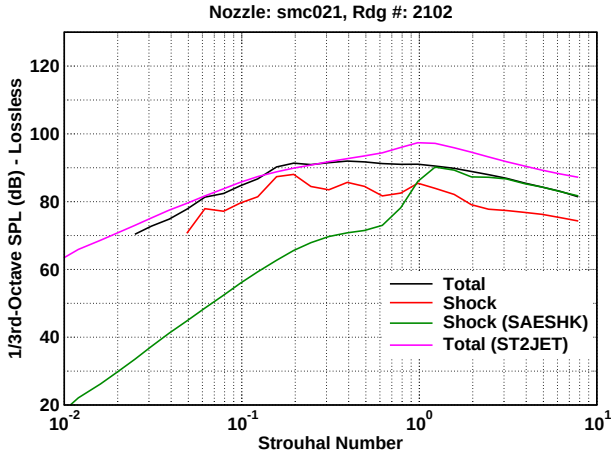

(s) $M_j = 1.048, \text{NPR} = 1.987, T_t/T_\infty = 2.66, \beta = 0.314$

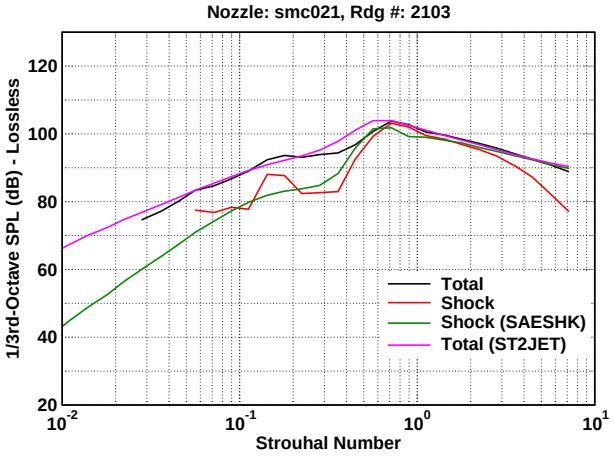

(t) $M_j = 1.175, \text{NPR} = 2.327, T_t/T_\infty = 2.65, \beta = 0.617$

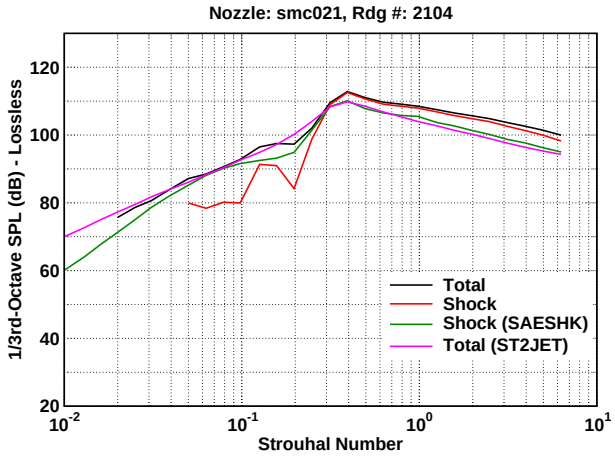

(u) $M_j = 1.391, \text{NPR} = 3.120, T_t/T_\infty = 2.66, \beta = 0.967$

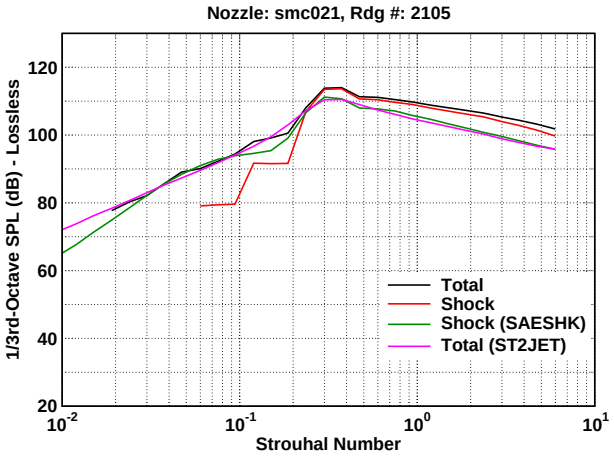

(v) $M_j = 1.490, \text{NPR} = 3.597, T_t/T_\infty = 2.65, \beta = 1.105$

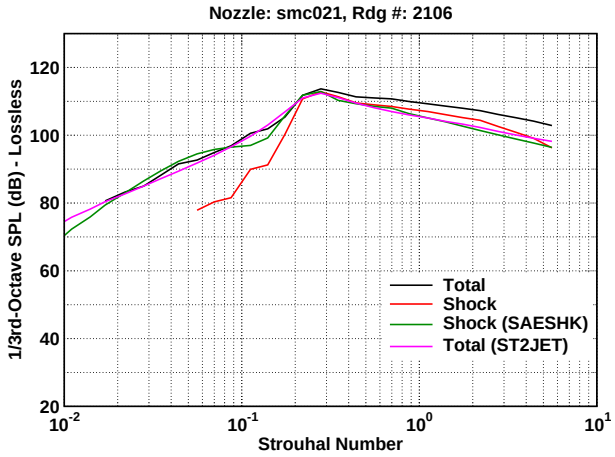

(w) $M_j = 1.660, \text{NPR} = 4.630, T_t/T_\infty = 2.64, \beta = 1.325$

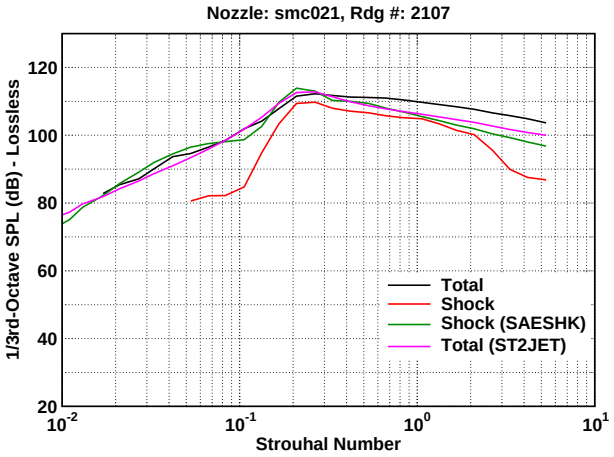

(x) $M_j = 1.789, \text{NPR} = 5.638, T_t/T_\infty = 2.65, \beta = 1.484$

Figure 16: (50 Deg., Cont.)

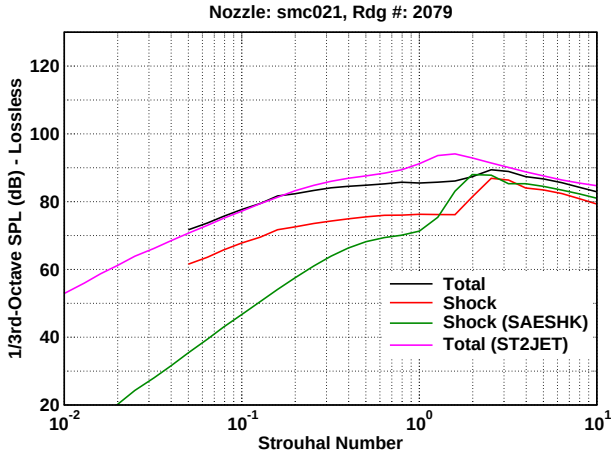

(a) $M_j = 1.049, \text{NPR} = 2.005, T_t/T_\infty = 1.01, \beta = 0.315$

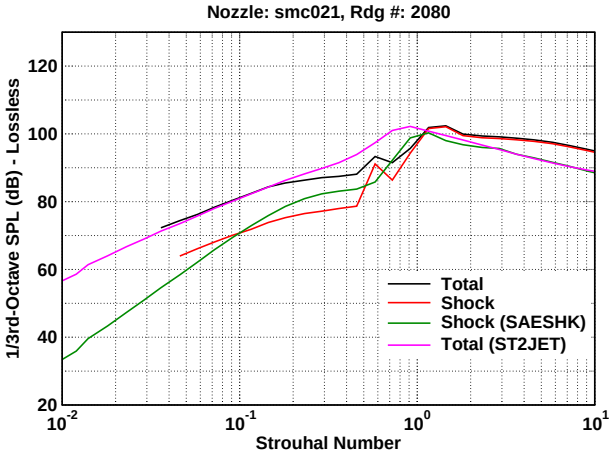

(b) $M_j = 1.178, \text{NPR} = 2.358, T_t/T_\infty = 1.01, \beta = 0.623$

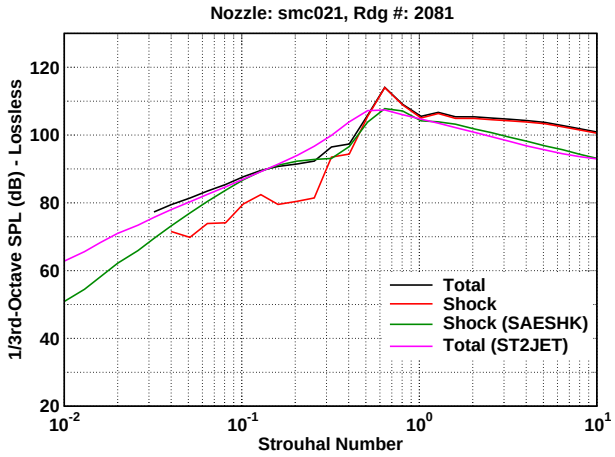

(c) $M_j = 1.392, \text{NPR} = 3.147, T_t/T_\infty = 1.01, \beta = 0.969$

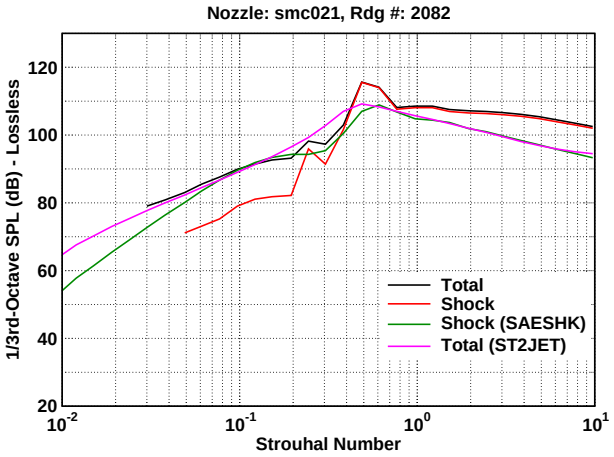

(d) $M_j = 1.493, \text{NPR} = 3.636, T_t/T_\infty = 1.01, \beta = 1.109$

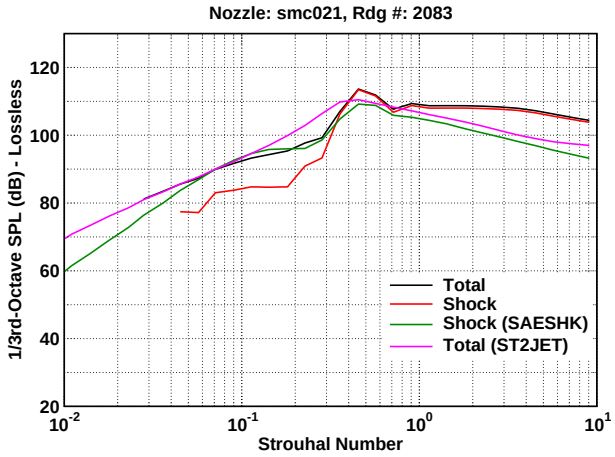

(e) $M_j = 1.660, \text{NPR} = 4.647, T_t/T_\infty = 1.01, \beta = 1.325$

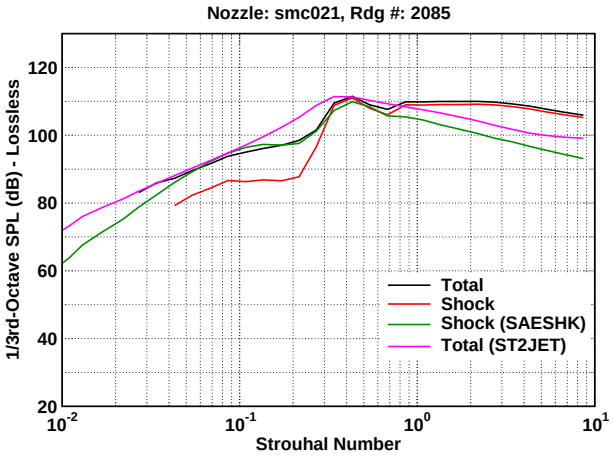

(f) $M_j = 1.796, \text{NPR} = 5.708, T_t/T_\infty = 1.01, \beta = 1.491$

Figure 17: 1/3-Octave spectra comparisons of jet noise prediction models to the total and shock component noise spectra for measured data from jets with shocks at a 90 degree inlet angle and distance $100D$.

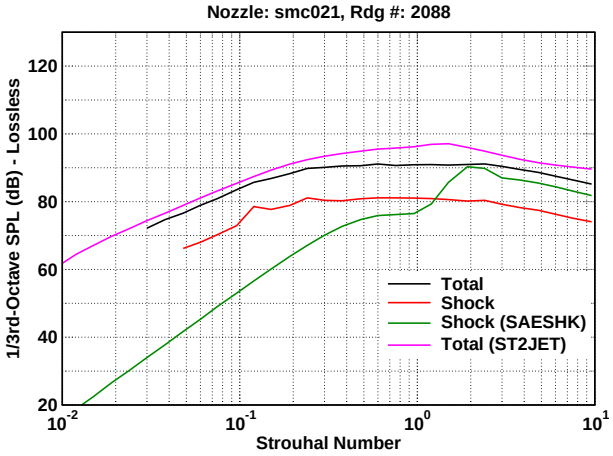

(g) $M_j = 1.049, \mathrm{NPR} = 2.004, T_t/T_\infty = 1.77, \beta = 0.319$

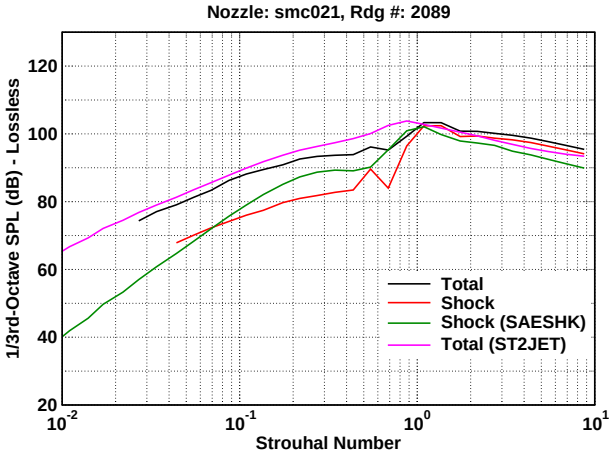

(h) $M_j = 1.182, \mathrm{NPR} = 2.365, T_t/T_\infty = 1.77, \beta = 0.630$

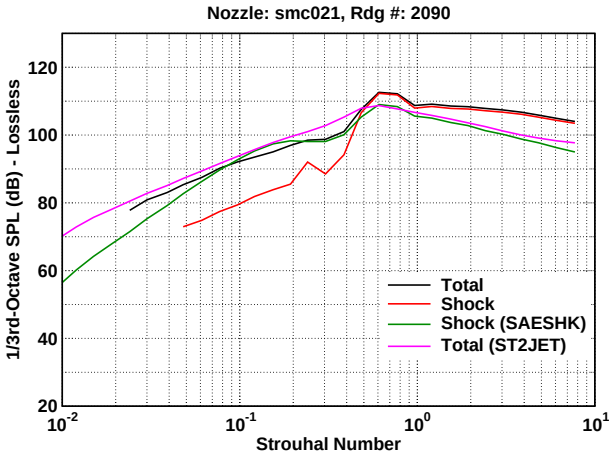

(i) $M_j = 1.392, \mathrm{NPR} = 3.143, T_t/T_\infty = 1.76, \beta = 0.968$

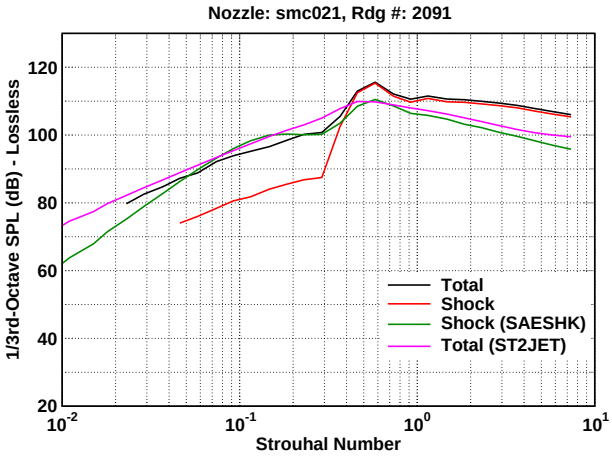

(j) $M_j = 1.492, \mathrm{NPR} = 3.627, T_t/T_\infty = 1.76, \beta = 1.108$

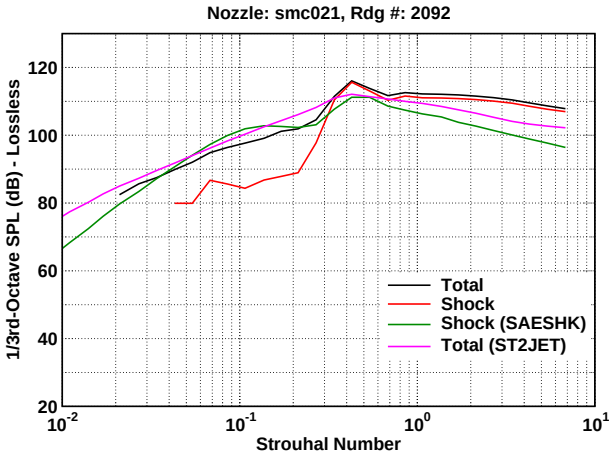

(k) $M_j = 1.660, \mathrm{NPR} = 4.644, T_t/T_\infty = 1.77, \beta = 1.325$

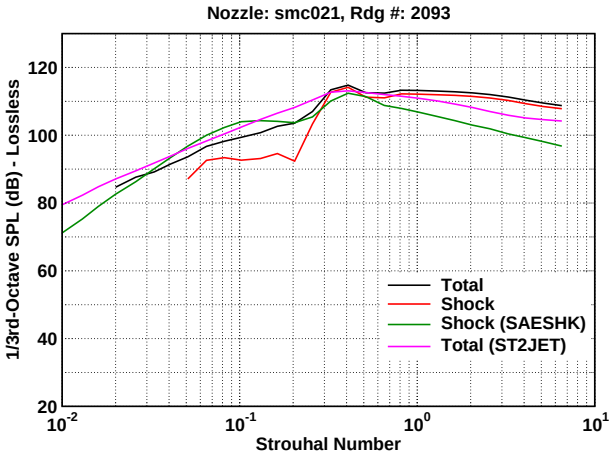

(l) $M_j = 1.792, \mathrm{NPR} = 5.674, T_t/T_\infty = 1.76, \beta = 1.487$

Figure 17: (90 Deg., Cont.)

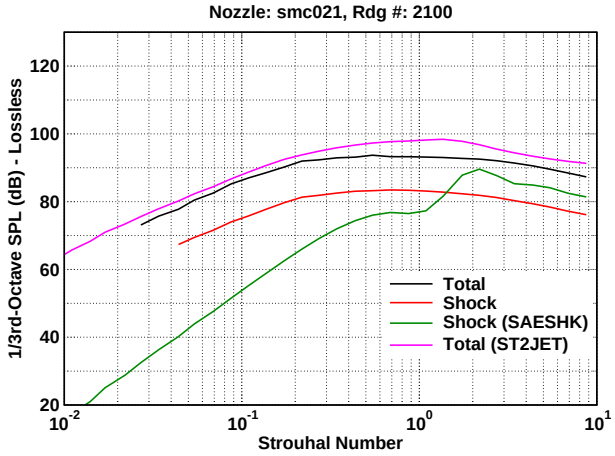

(m) $M_j = 1.045, \text{NPR} = 1.989, T_t/T_\infty = 2.16, \beta = 0.305$

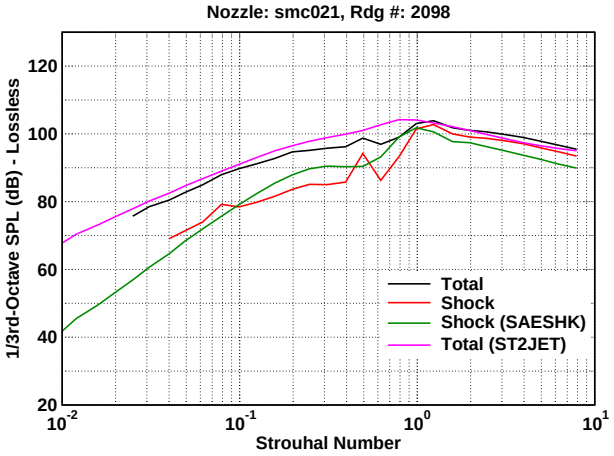

(n) $M_j = 1.181, \text{NPR} = 2.356, T_t/T_\infty = 2.16, \beta = 0.628$

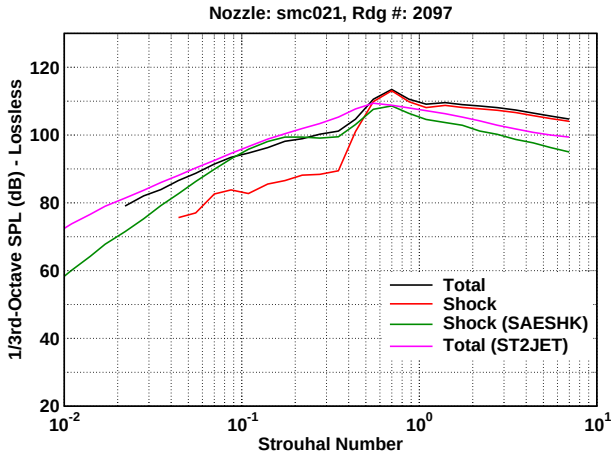

(o) $M_j = 1.390, \text{NPR} = 3.130, T_t/T_\infty = 2.16, \beta = 0.966$

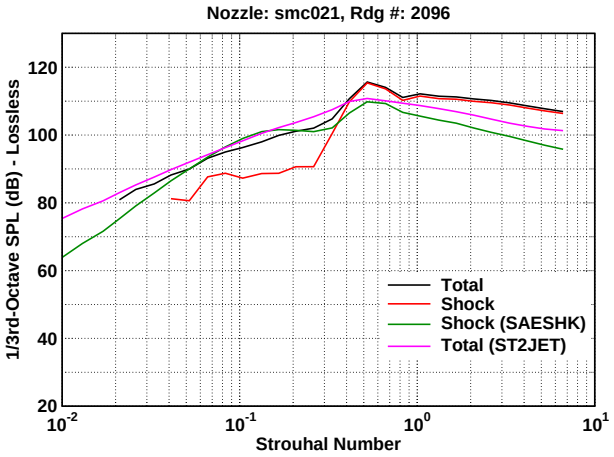

(p) $M_j = 1.494, \text{NPR} = 3.629, T_t/T_\infty = 2.16, \beta = 1.109$

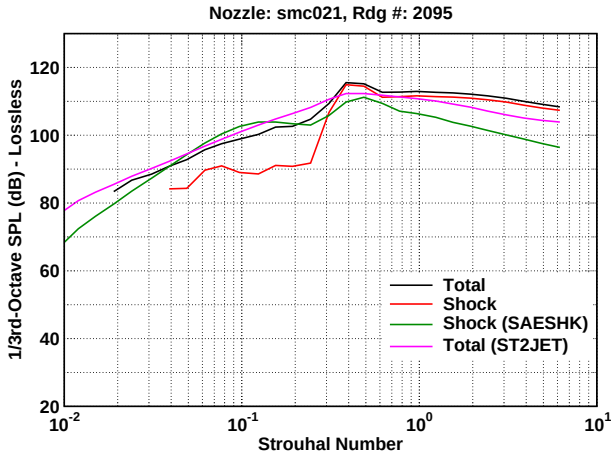

(q) $M_j = 1.660, \text{NPR} = 4.638, T_t/T_\infty = 2.16, \beta = 1.324$

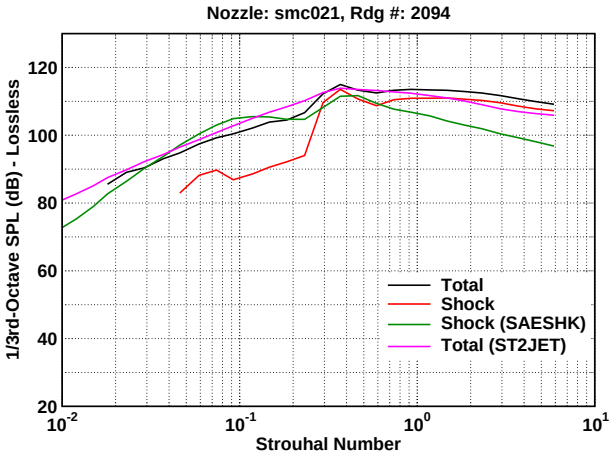

(r) $M_j = 1.794, \text{NPR} = 5.685, T_t/T_\infty = 2.16, \beta = 1.489$

Figure 17: (90 Deg., Cont.)

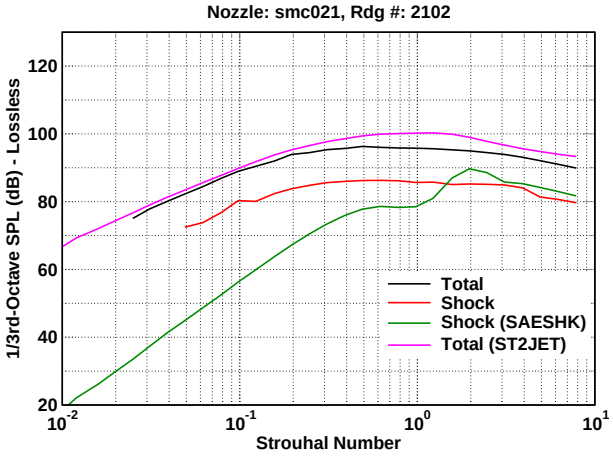

(s) $M_j = 1.048, \text{NPR} = 1.987, T_t/T_\infty = 2.66, \beta = 0.314$

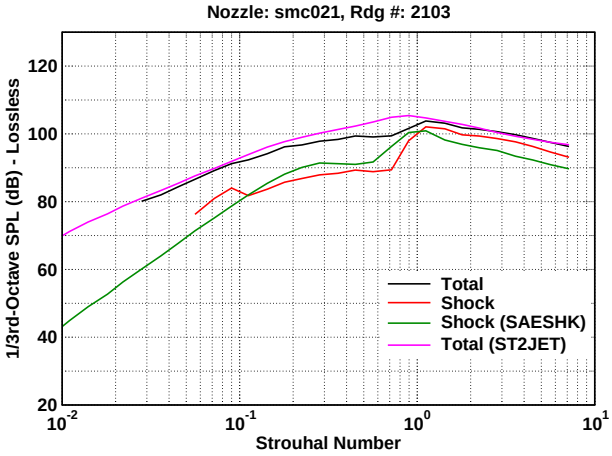

(t) $M_j = 1.175, \text{NPR} = 2.327, T_t/T_\infty = 2.65, \beta = 0.617$

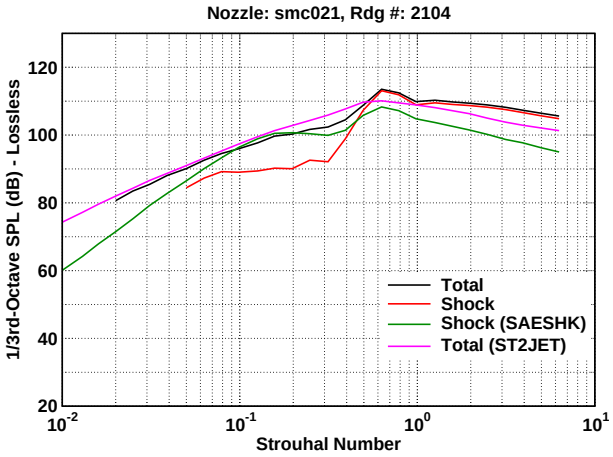

(u) $M_j = 1.391, \text{NPR} = 3.120, T_t/T_\infty = 2.66, \beta = 0.967$

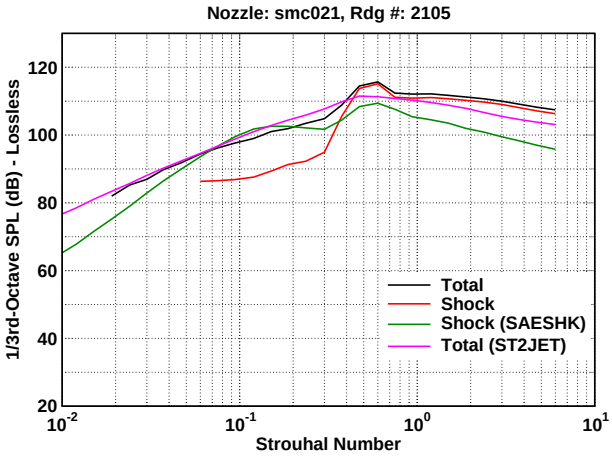

(v) $M_j = 1.490, \text{NPR} = 3.597, T_t/T_\infty = 2.65, \beta = 1.105$

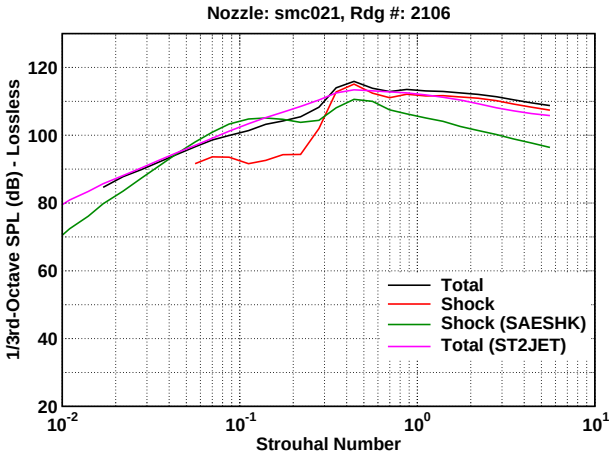

(w) $M_j = 1.660, \text{NPR} = 4.630, T_t/T_\infty = 2.64, \beta = 1.325$

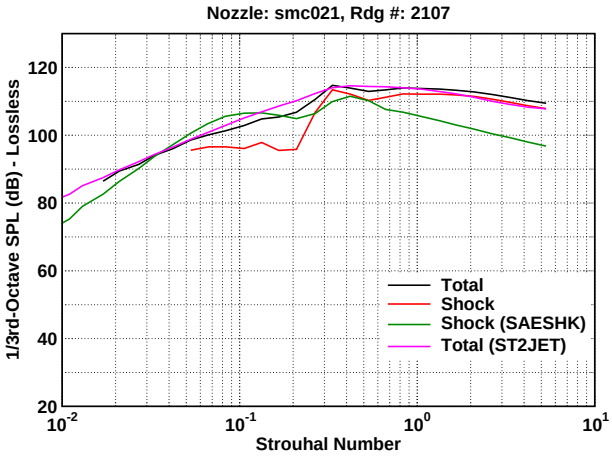

(x) $M_j = 1.789, \text{NPR} = 5.638, T_t/T_\infty = 2.65, \beta = 1.484$

Figure 17: (90 Deg., Cont.)

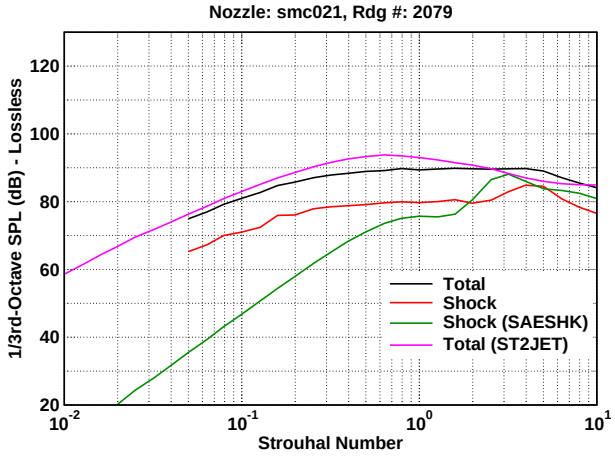

(a) $M_j = 1.049, \text{NPR} = 2.005, T_t/T_\infty = 1.01, \beta = 0.315$

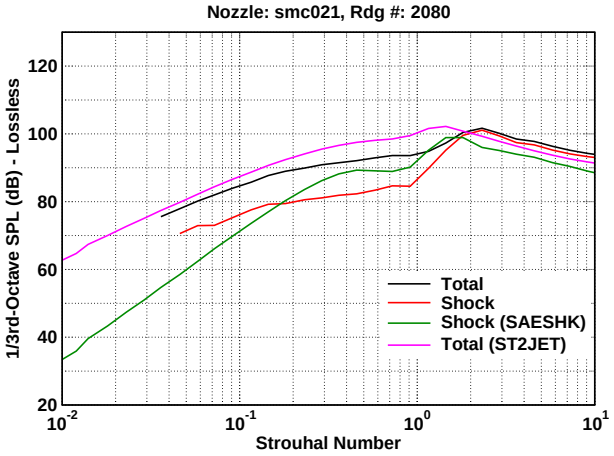

(b) $M_j = 1.178, \text{NPR} = 2.358, T_t/T_\infty = 1.01, \beta = 0.623$

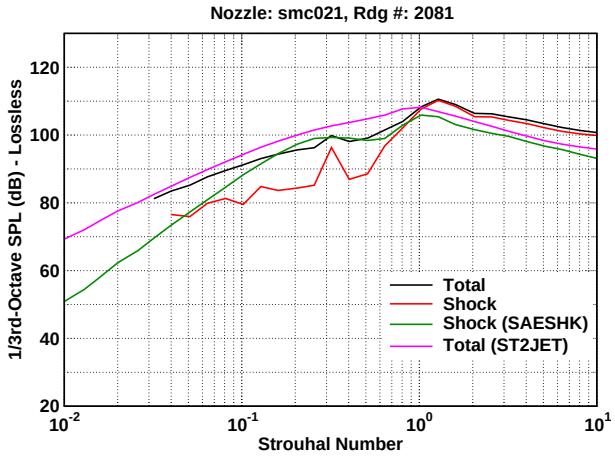

(c) $M_j = 1.392, \text{NPR} = 3.147, T_t/T_\infty = 1.01, \beta = 0.969$

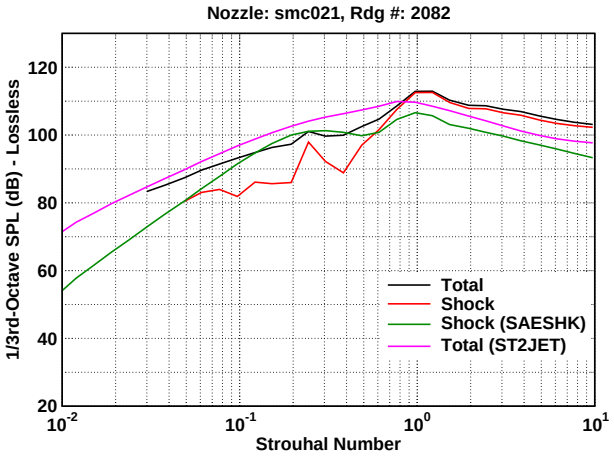

(d) $M_j = 1.493, \text{NPR} = 3.636, T_t/T_\infty = 1.01, \beta = 1.109$

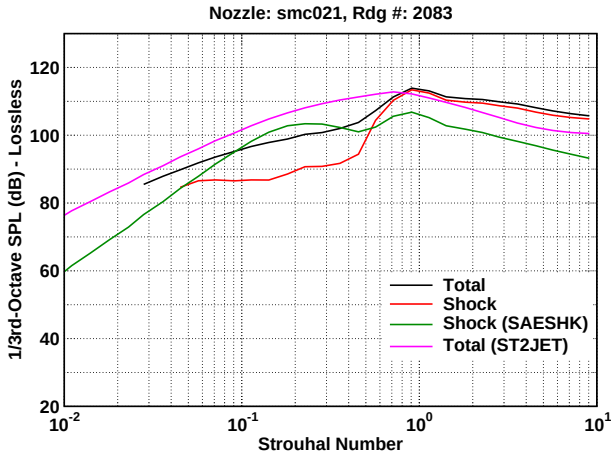

(e) $M_j = 1.660, \text{NPR} = 4.647, T_t/T_\infty = 1.01, \beta = 1.325$

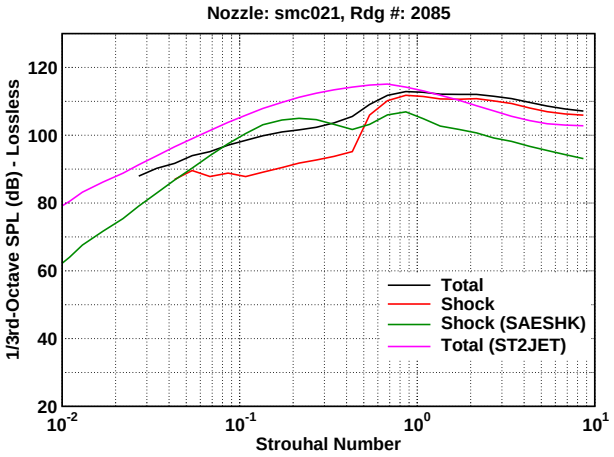

(f) $M_j = 1.796, \text{NPR} = 5.708, T_t/T_\infty = 1.01, \beta = 1.491$

Figure 18: 1/3-Octave spectra comparisons of jet noise prediction models to the total and shock component noise spectra for measured data from jets with shocks at a 120 degree inlet angle and distance $100D$.

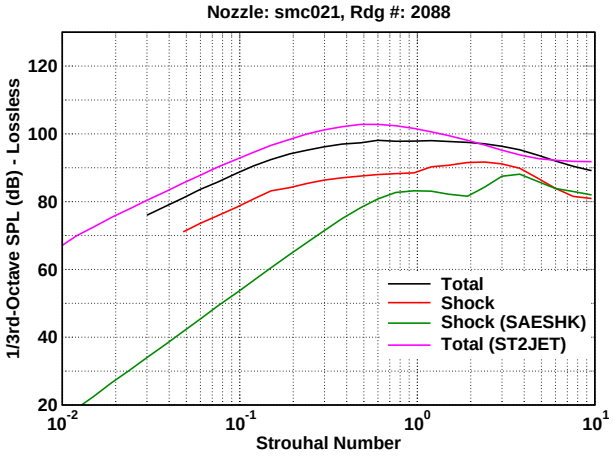

(g) $M_j = 1.049, \text{NPR} = 2.004, T_t/T_\infty = 1.77, \beta = 0.319$

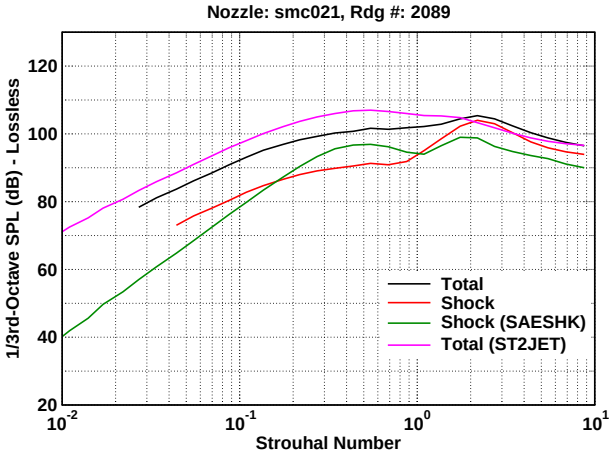

(h) $M_j = 1.182, \text{NPR} = 2.365, T_t/T_\infty = 1.77, \beta = 0.630$

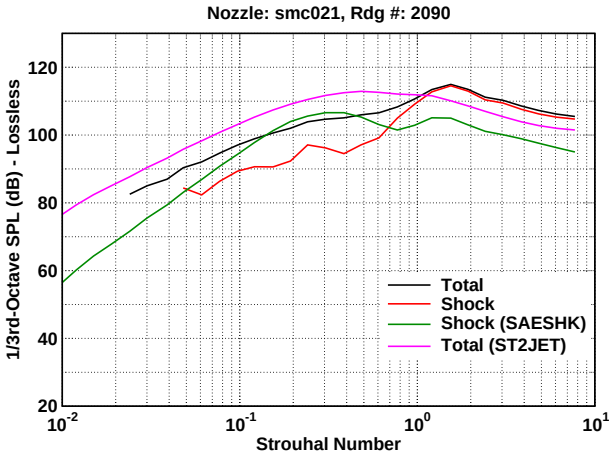

(i) $M_j = 1.392, \text{NPR} = 3.143, T_t/T_\infty = 1.76, \beta = 0.968$

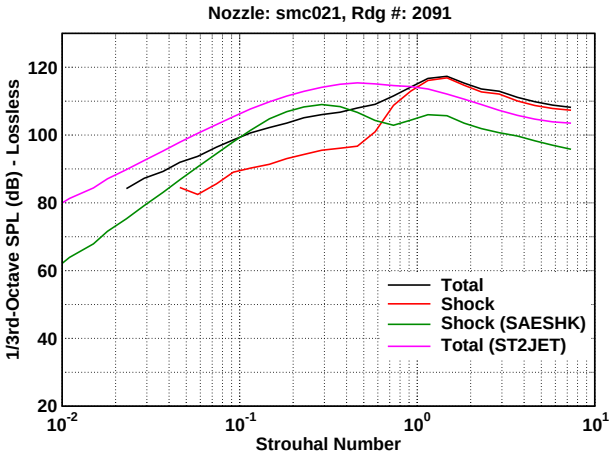

(j) $M_j = 1.492, \text{NPR} = 3.627, T_t/T_\infty = 1.76, \beta = 1.108$

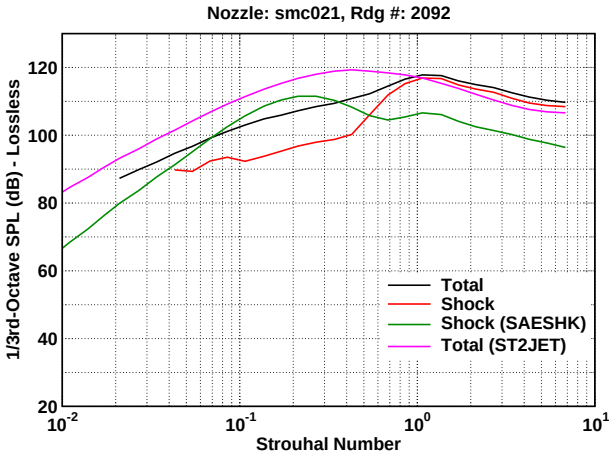

(k) $M_j = 1.660, \text{NPR} = 4.644, T_t/T_\infty = 1.77, \beta = 1.325$

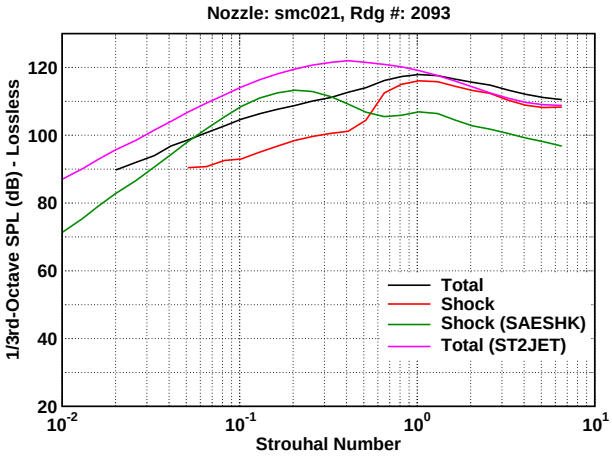

(l) $M_j = 1.792, \text{NPR} = 5.674, T_t/T_\infty = 1.76, \beta = 1.487$

Figure 18: (120 Deg., Cont.)

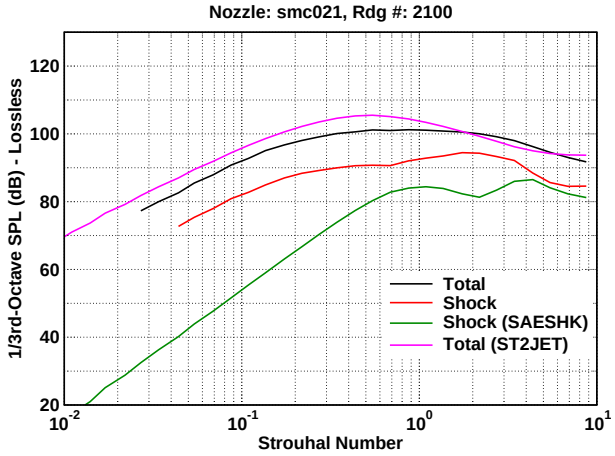

(m) $M_j = 1.045, \text{NPR} = 1.989, T_t/T_\infty = 2.16, \beta = 0.305$

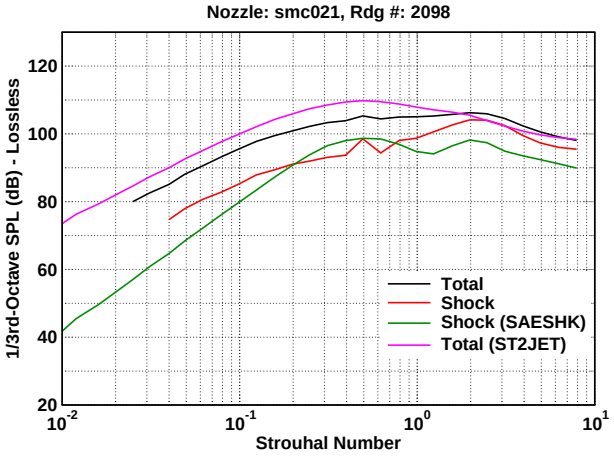

(n) $M_j = 1.181, \text{NPR} = 2.356, T_t/T_\infty = 2.16, \beta = 0.628$

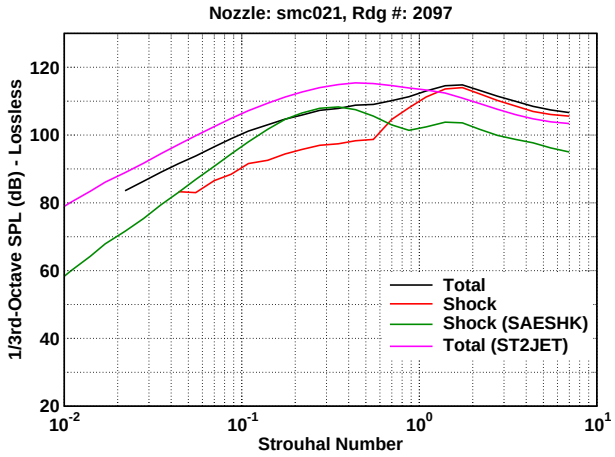

(o) $M_j = 1.390, \text{NPR} = 3.130, T_t/T_\infty = 2.16, \beta = 0.966$

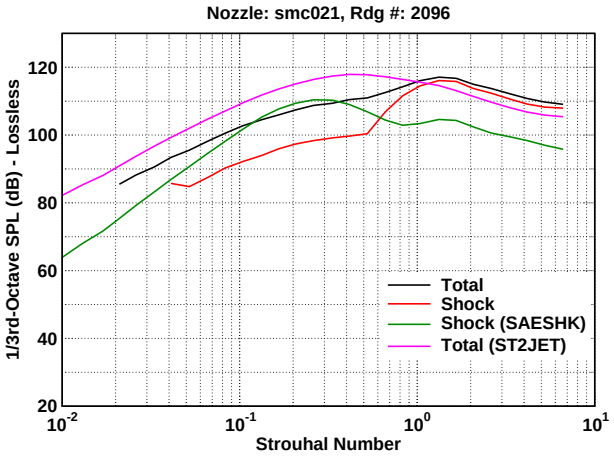

(p) $M_j = 1.494, \text{NPR} = 3.629, T_t/T_\infty = 2.16, \beta = 1.109$

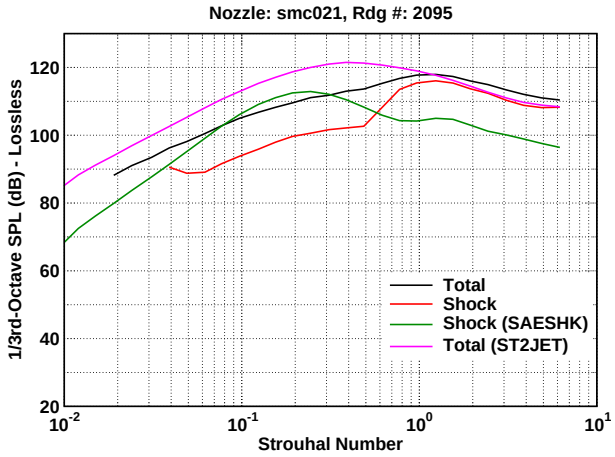

(q) $M_j = 1.660, \text{NPR} = 4.638, T_t/T_\infty = 2.16, \beta = 1.324$

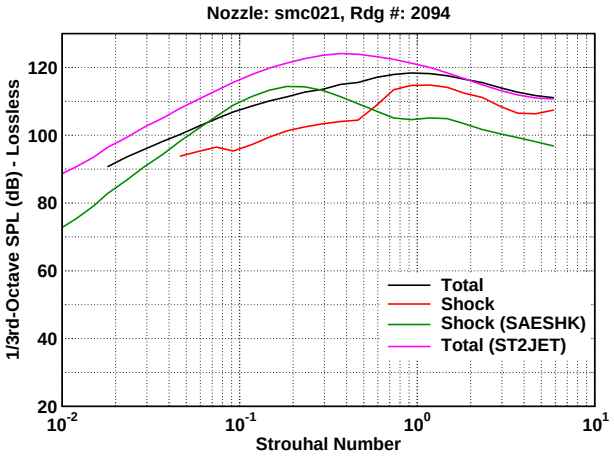

(r) $M_j = 1.794, \text{NPR} = 5.685, T_t/T_\infty = 2.16, \beta = 1.489$

Figure 18: (120 Deg., Cont.)

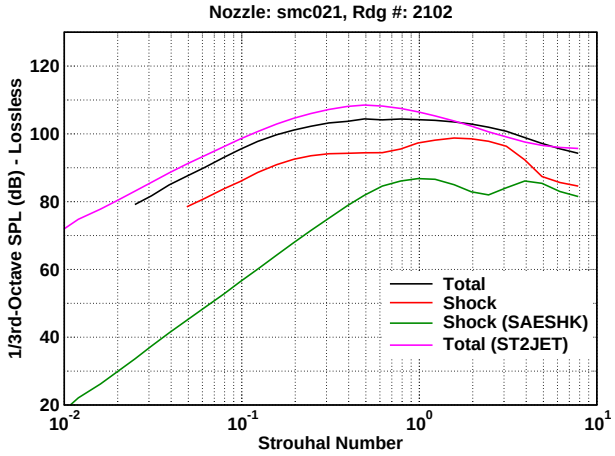

(s) $M_j = 1.048, \text{NPR} = 1.987, T_t/T_\infty = 2.66, \beta = 0.314$

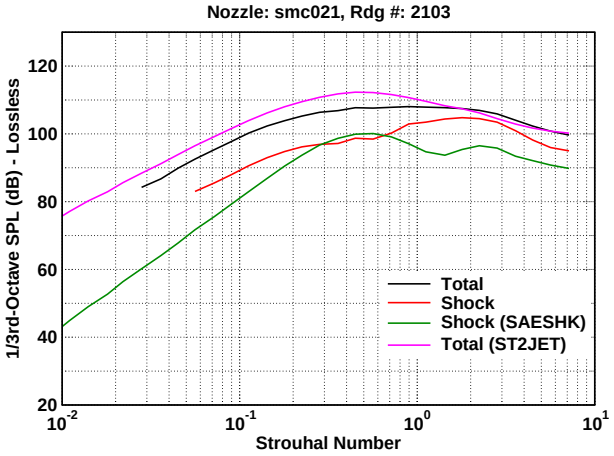

(t) $M_j = 1.175, \text{NPR} = 2.327, T_t/T_\infty = 2.65, \beta = 0.617$

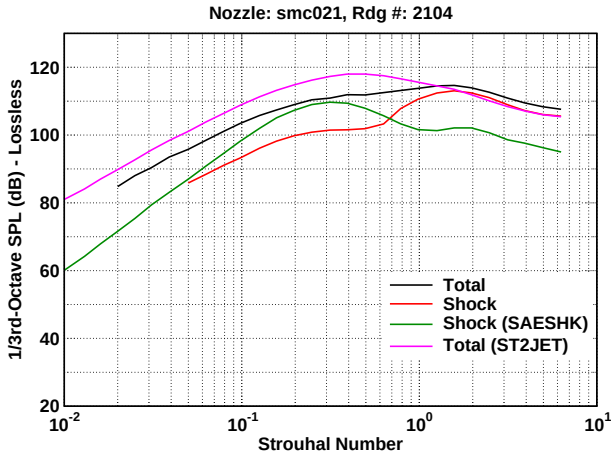

(u) $M_j = 1.391, \text{NPR} = 3.120, T_t/T_\infty = 2.66, \beta = 0.967$

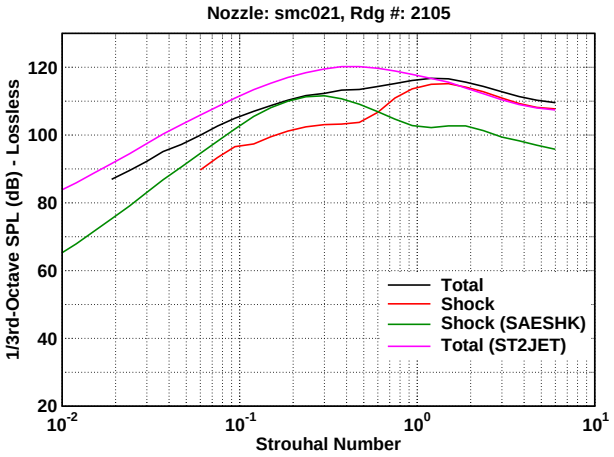

(v) $M_j = 1.490, \text{NPR} = 3.597, T_t/T_\infty = 2.65, \beta = 1.105$

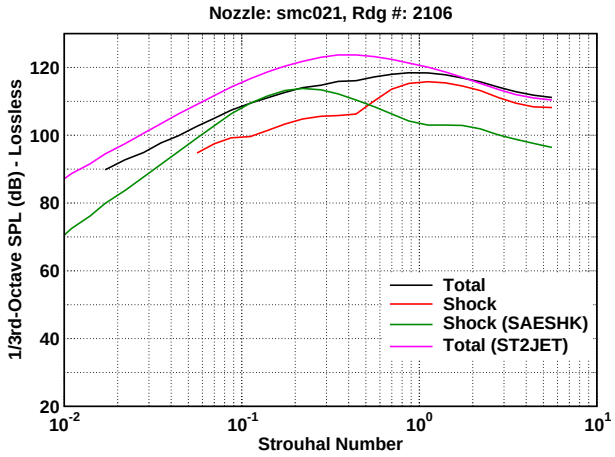

(w) $M_j = 1.660, \text{NPR} = 4.630, T_t/T_\infty = 2.64, \beta = 1.325$

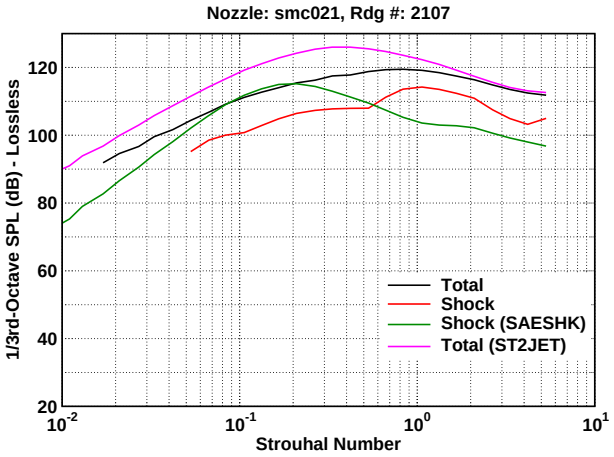

(x) $M_j = 1.789, \text{NPR} = 5.638, T_t/T_\infty = 2.65, \beta = 1.484$

Figure 18: (120 Deg., Cont.)

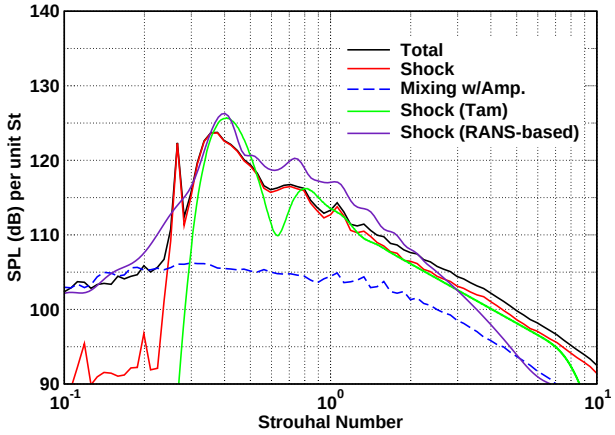

(a) Power Spectral Density at 50 degrees.

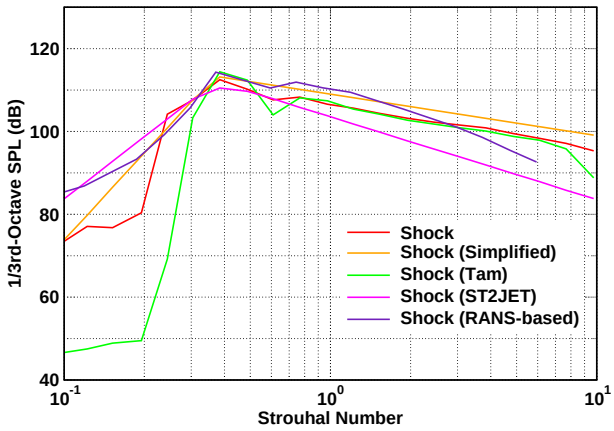

(b) 1/3-Octave Spectra at 50 degrees.

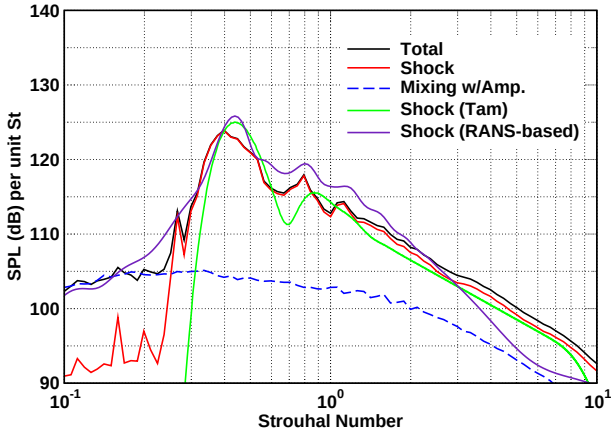

(c) Power Spectral Density at 60 degrees.

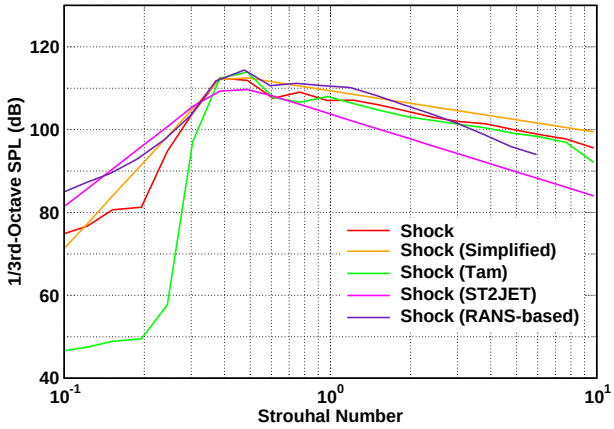

(d) 1/3-Octave Spectra at 60 degrees.

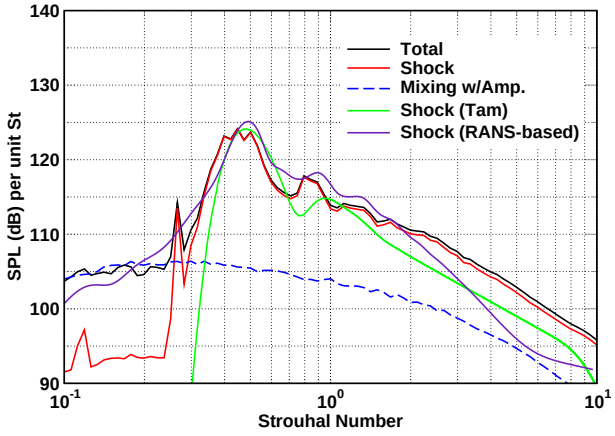

(e) Power Spectral Density at 70 degrees.

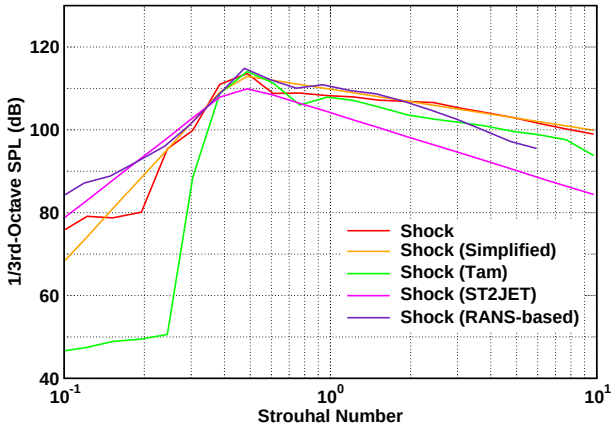

(f) 1/3-Octave Spectra at 70 degrees.

Figure 19: Spectral comparisons of jet shock associated noise prediction models to the jet noise component spectra for measured data from jets with shocks at a distance $100D$; $M_j = 1.493, \text{NPR} = 3.636, T_t/T_\infty = 1.01$.

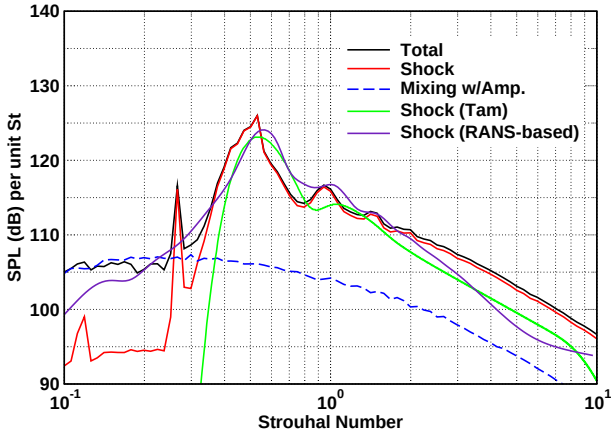

(g) Power Spectral Density at 80 degrees.

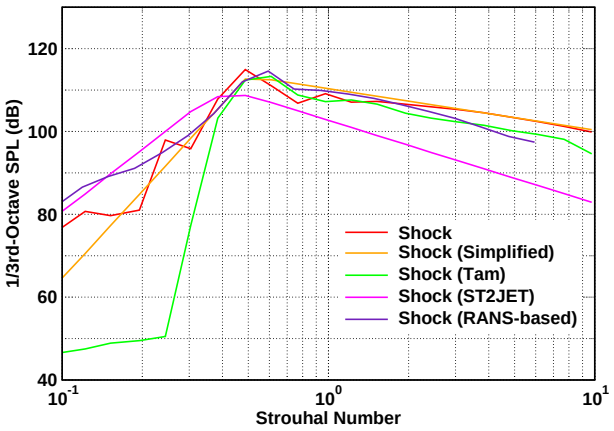

(h) 1/3-Octave Spectra at 80 degrees.

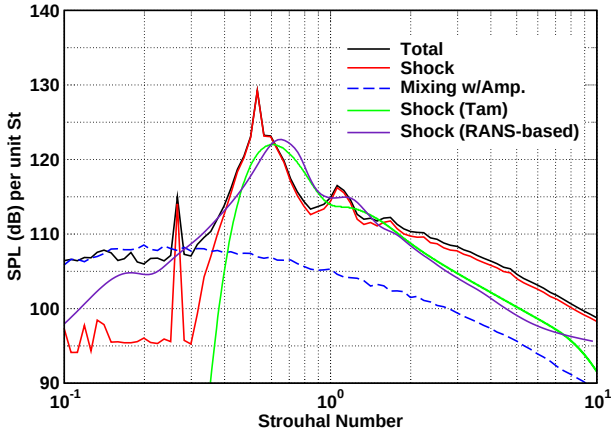

(i) Power Spectral Density at 90 degrees.

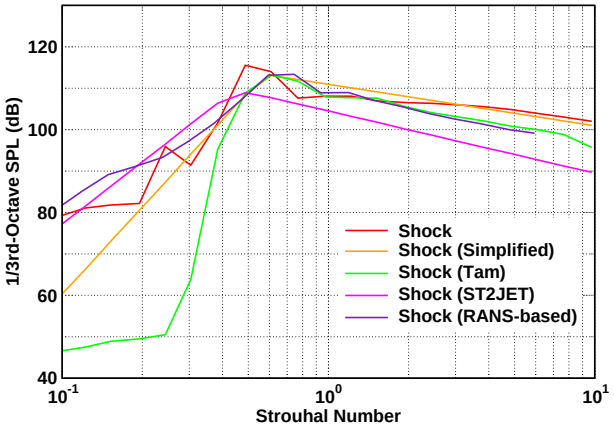

(j) 1/3-Octave Spectra at 90 degrees.

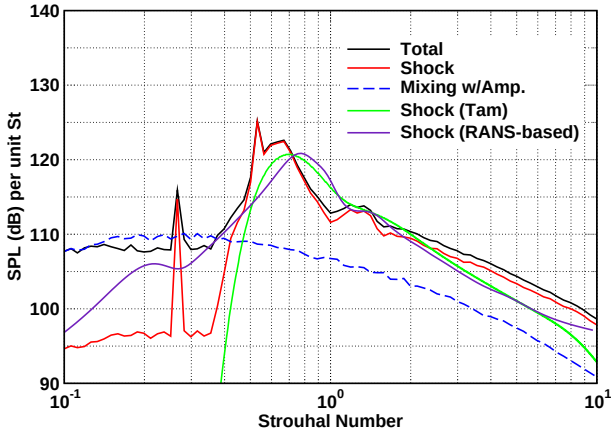

(k) Power Spectral Density at 100 degrees.

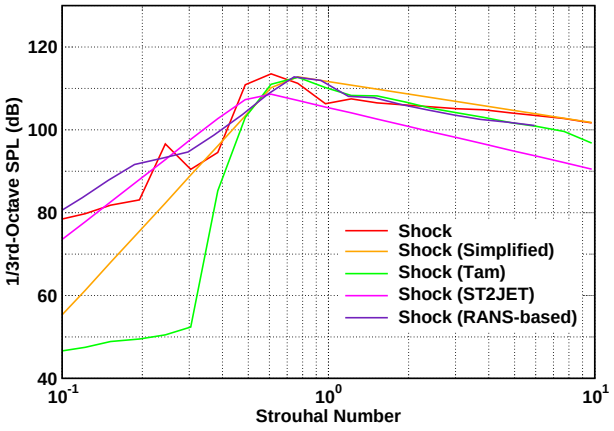

(l) 1/3-Octave Spectra at 100 degrees.

Figure 19: ($T_t/T_\infty = 1.01$, Cont.)

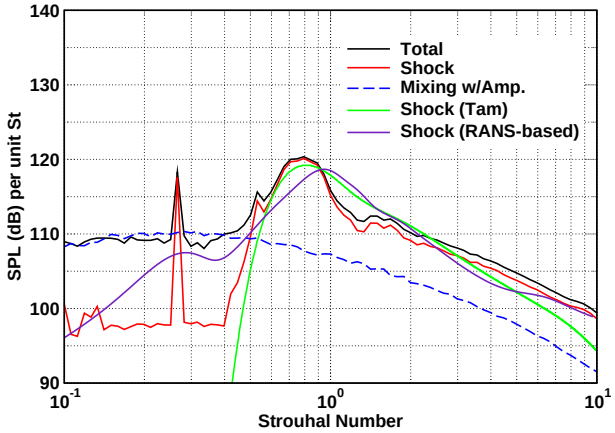

(m) Power Spectral Density at 110 degrees.

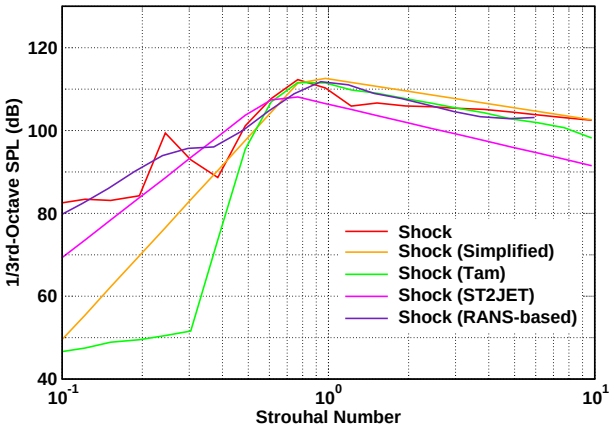

(n) 1/3-Octave Spectra at 110 degrees.

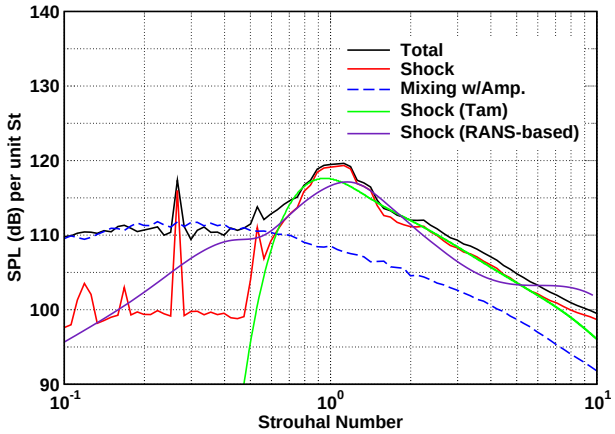

(o) Power Spectral Density at 120 degrees.

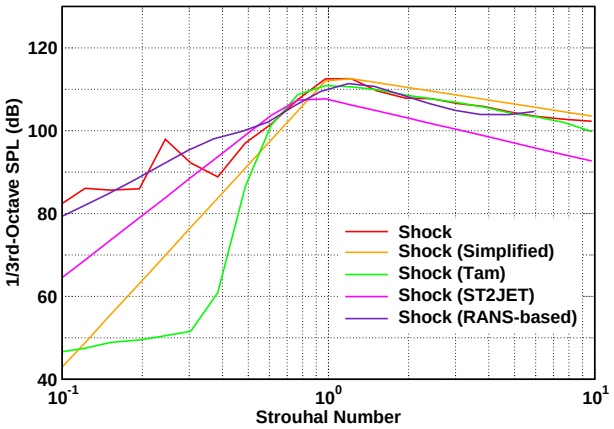

(p) 1/3-Octave Spectra at 120 degrees.

Figure 19: ($T_t/T_\infty = 1.01$, Cont.)

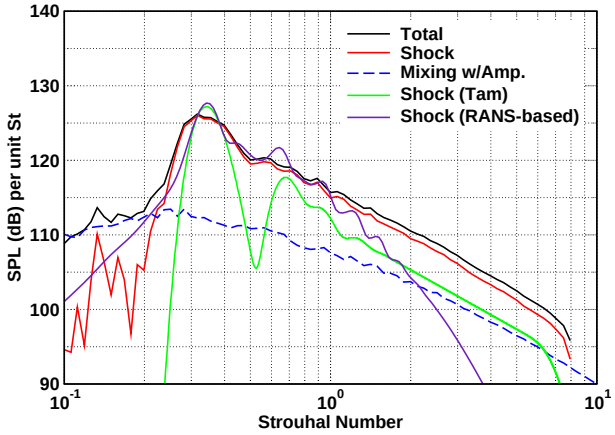

(a) Power Spectral Density at 50 degrees.

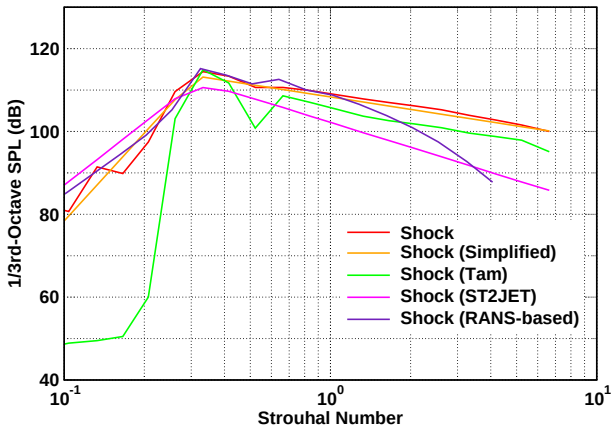

(b) 1/3-Octave Spectra at 50 degrees.

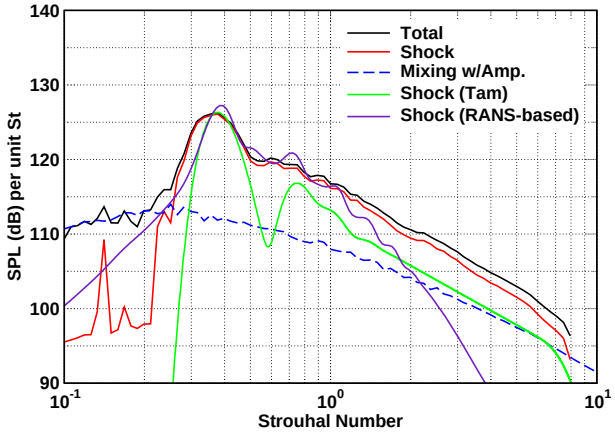

(c) Power Spectral Density at 60 degrees.

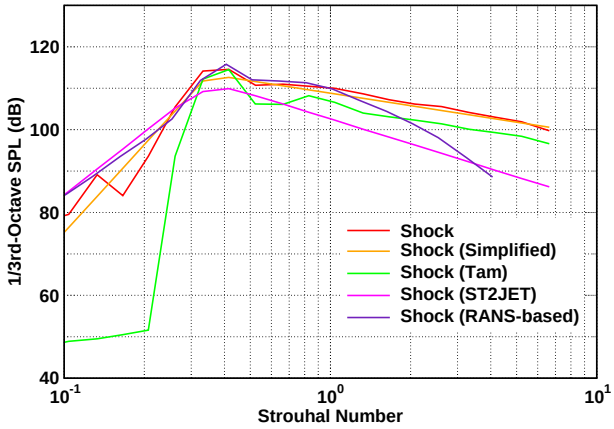

(d) 1/3-Octave Spectra at 60 degrees.

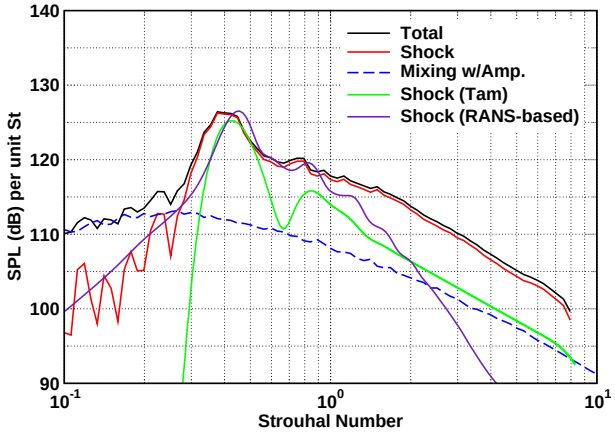

(e) Power Spectral Density at 70 degrees.

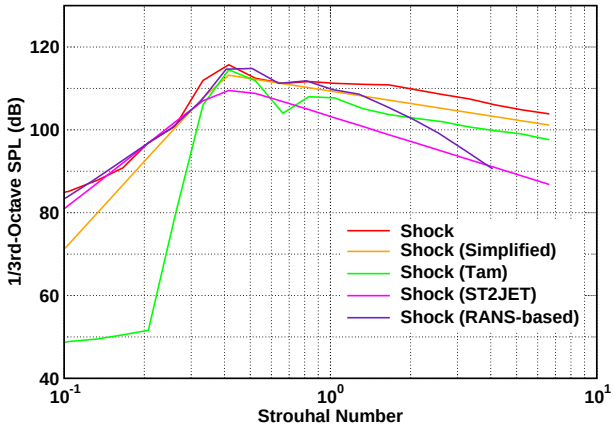

(f) 1/3-Octave Spectra at 70 degrees.

Figure 20: Spectral comparisons of jet shock associated noise prediction models to the jet noise component spectra for measured data from jets with shocks at a distance $100D$; $M_j = 1.494$, NPR $= 3.629$, $T_t/T_\infty = 2.16$.

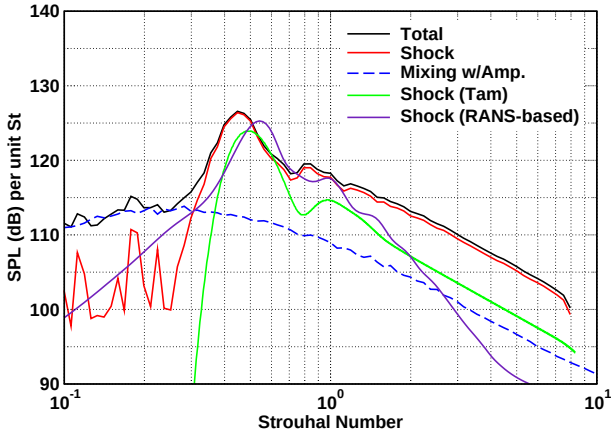

(g) Power Spectral Density at 80 degrees.

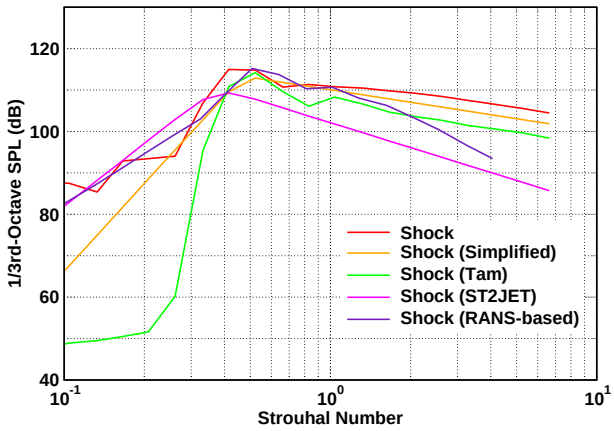

(h) 1/3-Octave Spectra at 80 degrees.

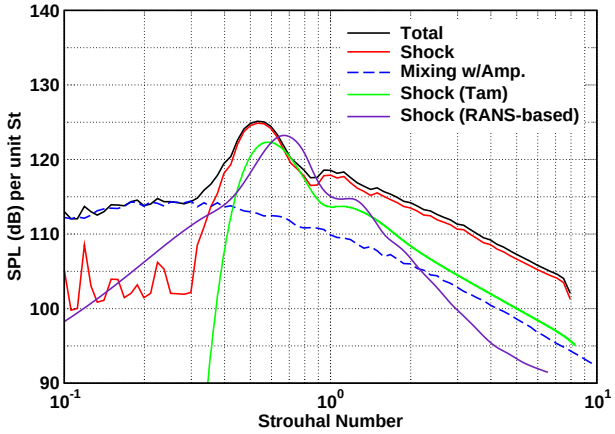

(i) Power Spectral Density at 90 degrees.

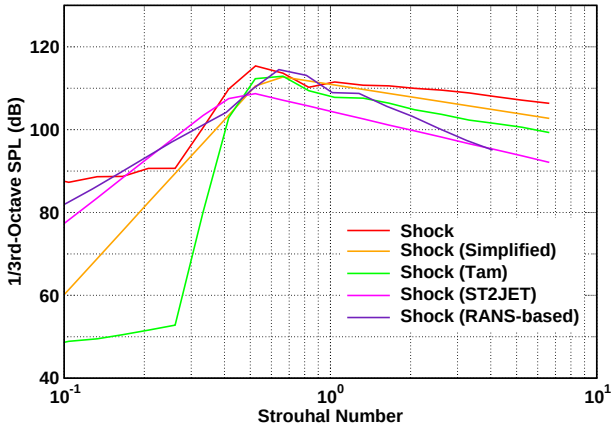

(j) 1/3-Octave Spectra at 90 degrees.

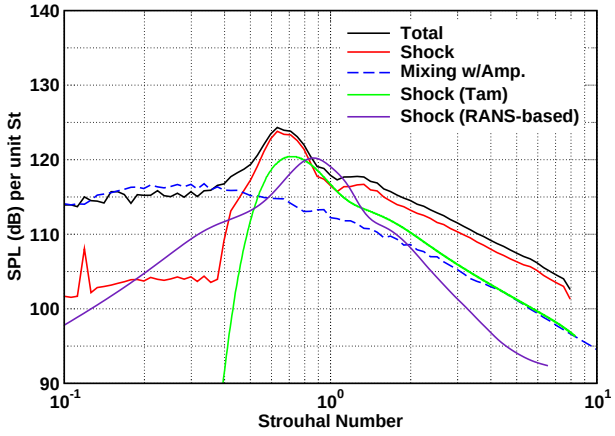

(k) Power Spectral Density at 100 degrees.

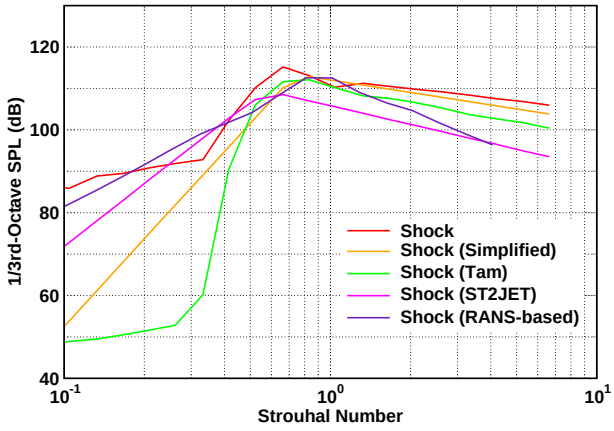

(l) 1/3-Octave Spectra at 100 degrees.

Figure 20: ($T_t/T_\infty = 2.16$, Cont.)

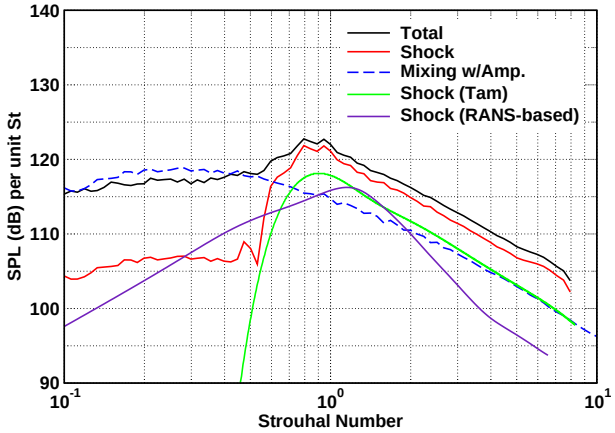

(m) Power Spectral Density at 110 degrees.

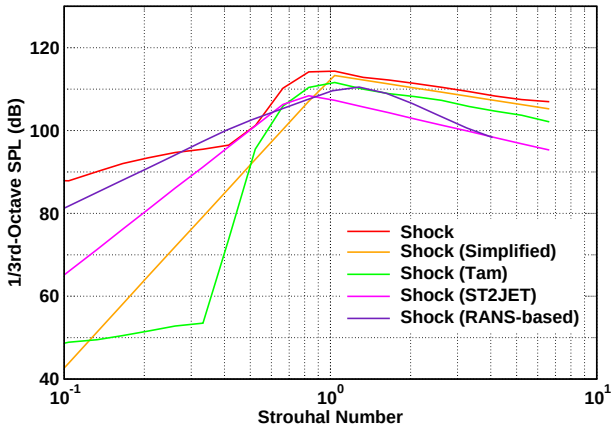

(n) 1/3-Octave Spectra at 110 degrees.

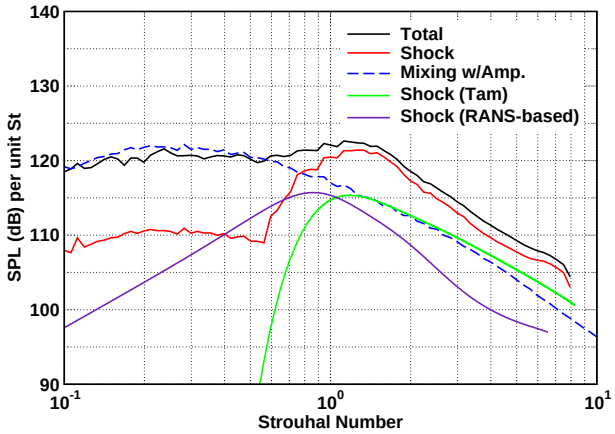

(o) Power Spectral Density at 120 degrees.

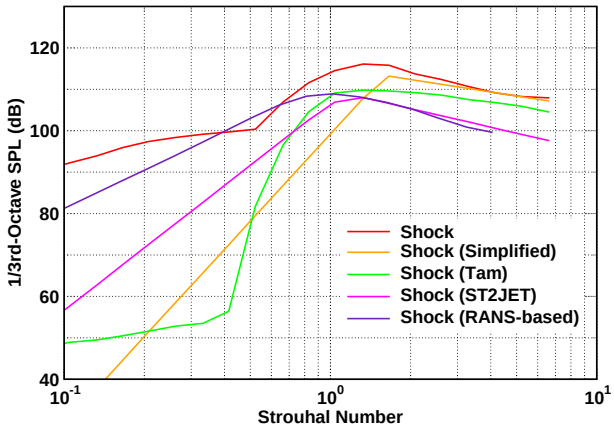

(p) 1/3-Octave Spectra at 120 degrees.

Figure 20: ($T_t/T_\infty = 2.16$, Cont.)

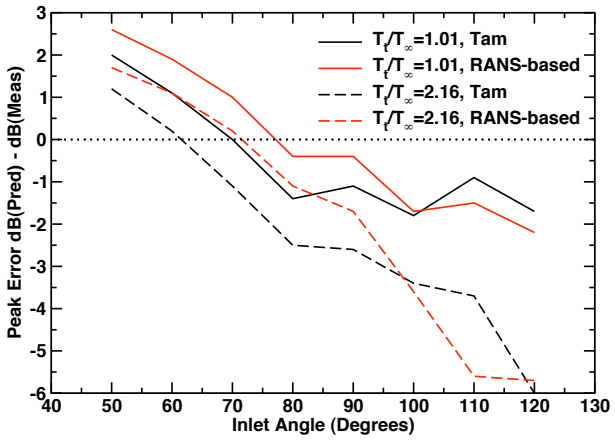

(a) PSD Peak Level Error.

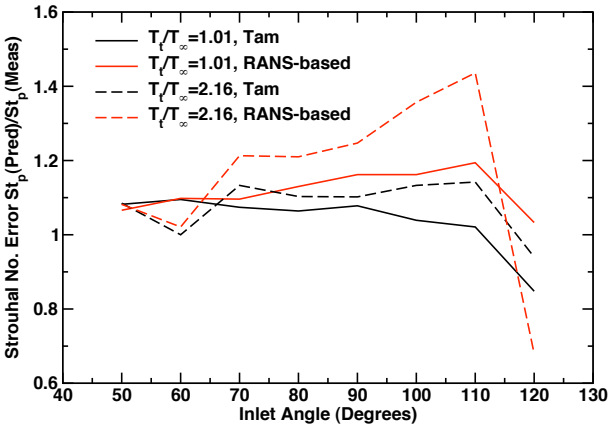

(b) PSD Peak Strouhal No. Error.

Figure 21: Errors in peak level and Strouhal number between predicted and measured shock-associated noise values from the power spectral density (PSD) data in Figures 19 and 20.

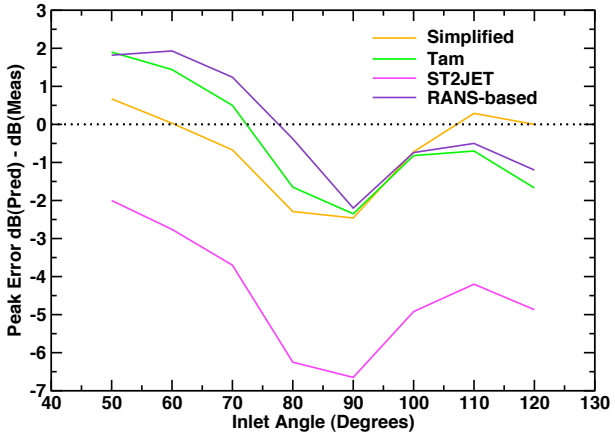

(a) 1/3-Octave Peak Level Error, $T_t/T_\infty = 1.01$.

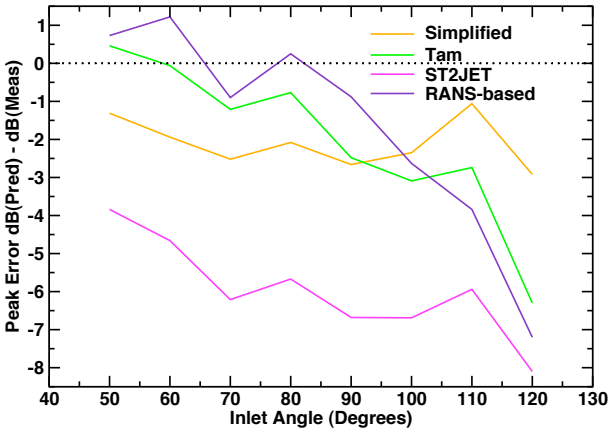

(b) 1/3-Octave Peak Level Error, $T_t/T_\infty = 2.16$.

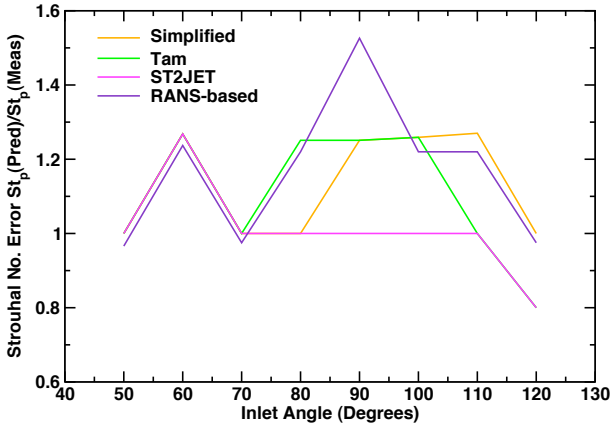

(c) 1/3-Octave Peak Strouhal No. Error, $T_t/T_\infty = 1.01$.

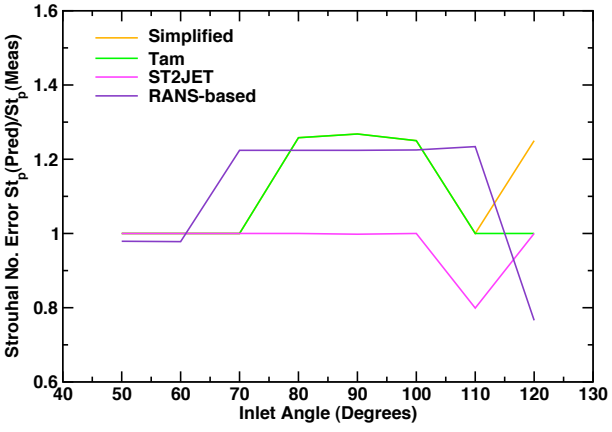

(d) 1/3-Octave Peak Strouhal No. Error, $T_t/T_\infty = 2.16$.

Figure 22: Errors in peak level and Strouhal number between predicted and measured shock-associated noise values from the 1/3-octave spectral data in Figures 19 and 20.

REPORT DOCUMENTATION PAGE	Form Approved OMB No. 0704-0188

1. REPORT DATE *(DD-MM-YYYY)*	2. REPORT TYPE	3. DATES COVERED *(From - To)*
01-05-2010	Technical Memorandum	

4. TITLE AND SUBTITLE
Predictions of Supersonic Jet Mixing and Shock-Associated Noise Compared with Measured Far-Field Data

5a. CONTRACT NUMBER

5b. GRANT NUMBER

5c. PROGRAM ELEMENT NUMBER

6. AUTHOR(S)
Dahl, Milo, D.

5d. PROJECT NUMBER

5e. TASK NUMBER

5f. WORK UNIT NUMBER
WBS 984754.02.07.03.17.02

7. PERFORMING ORGANIZATION NAME(S) AND ADDRESS(ES)
National Aeronautics and Space Administration
John H. Glenn Research Center at Lewis Field
Cleveland, Ohio 44135-3191

8. PERFORMING ORGANIZATION REPORT NUMBER
E-17262

9. SPONSORING/MONITORING AGENCY NAME(S) AND ADDRESS(ES)
National Aeronautics and Space Administration
Washington, DC 20546-0001

10. SPONSORING/MONITOR'S ACRONYM(S)
NASA

11. SPONSORING/MONITORING REPORT NUMBER
NASA/TM-2010-216328

12. DISTRIBUTION/AVAILABILITY STATEMENT
Unclassified-Unlimited
Subject Category: 71
Available electronically at http://gltrs.grc.nasa.gov
This publication is available from the NASA Center for AeroSpace Information, 443-757-5802

13. SUPPLEMENTARY NOTES

14. ABSTRACT
Codes for predicting supersonic jet mixing and broadband shock-associated noise were assessed using a database containing noise measurements of a jet issuing from a convergent nozzle. Two types of codes were used to make predictions. Fast running codes containing empirical models were used to compute both the mixing noise component and the shock-associated noise component of the jet noise spectrum. One Reynolds-averaged, Navier-Stokes-based code was used to compute only the shock-associated noise. To enable the comparisons of the predicted component spectra with data, the measured total jet noise spectra were separated into mixing noise and shock-associated noise components. Comparisons were made for 1/3-octave spectra and some power spectral densities using data from jets operating at 24 conditions covering essentially 6 fully expanded Mach numbers with 4 total temperature ratios.

15. SUBJECT TERMS
Jet noise; Noise prediction; Propulsion noise; Flow noise; Noise; Shocks; Supersonic jets; Accuracy

16. SECURITY CLASSIFICATION OF:			17. LIMITATION OF ABSTRACT	18. NUMBER OF PAGES	19a. NAME OF RESPONSIBLE PERSON
a. REPORT	b. ABSTRACT	c. THIS PAGE			STI Help Desk (email:help@sti.nasa.gov)
U	U	U	UU	80	19b. TELEPHONE NUMBER *(include area code)* 443-757-5802